DEVELOPMENT OF IMAGING PLATFORM FOR MULTI-SPECTRAL BIOLUMINESCENCE IMAGING

By

Vivek Venugopal

A Thesis Submitted to the Graduate

Faculty of Rensselaer Polytechnic Institute

in Partial Fulfillment of the

Requirements for the Degree of

MASTER OF SCIENCE

Major Subject: ELECTRICAL ENGINEERING

Approved:

_____

Birsen Yazici, Thesis Adviser

_____

Xavier Intes, Co-Thesis Adviser

Rensselaer Polytechnic Institute
Troy, New York

November 2007
(For Graduation December 2007)

CONTENTS

LIST OF TABLES

LIST OF FIGURES

ACKNOWLEDGMENT

Owing to the multidisciplinary nature of this project, there are many people without whose guidance and support this thesis would not have been possible. First of all I would like to thank my advisers Prof. Birsen Yazici and Prof. Xavier Intes for their support and providing me an opportunity to work on this project. I would particulary like to thank Prof. Intes for his encouragement and guidance over the course of this project. Moreover I would like to thank both of them for providing me with the assistantship which enabled me to join this department.

I would like to thank Prof. Kevin Craig and Jason Leucht in the Mechnical engineering department at RPI for their advice on the automation of the system. I would also like to express my gratitude to Mr. James Schatz and Ed Kreiger at the Research Machine shop at RPI for their invaluable recommendations on system design and fabrication.

While it is impossible to thank all the people who have helped me over the course of this project, I would like to especially thank Dhanannjay Deo at the Advanced Computational Research Laboratory at RPI, Ramesh Ahuja at LaVision Systems, Pamela Zepf, Jaskaran Sangra and Jin Chen for their assistance over the past months while this system was being developed.

Above all, I would like to thank my parents for their constant support and encouragement over the course of my studies.

ABSTRACT

The field known as biomedical optics has evolved considerably over the last couple of decades. The widespread availability of suitable laser sources and detectors has aided the rapid development of new optical technologies for the monitoring and diagnosis, as well as treatment, of patients. Furthermore, new optical techniques are helping to advance fundamental biomedical research. Bioluminescence imaging and tomography is a fairly new optical imaging technique which is finding wide ranging applications in cancer research and immunotherapy. My Masters thesis involved the development and evaluation of a prototype multi-view, multi-spectral optical tomographic imaging system, whose principal application is imaging bioluminescence signals in small animals.

The platform developed is capable of acquiring multi-view images at a high angular resolution of 10° and an error in angular position control of $\sim 1^{\circ}$. The spectral imaging capability of the acquisition system allows for imaging the exiting light within a 20 nm spectral band giving this platform one of the highest spectral resolution among the state-of-the-art bioluminescence imaging instrumentation. The tomographic aspect of the platform is accomplished in a novel way by employing a stereo camera system to extract a surface of the test subject.

The system's sensitivity was characterised and the performance was analysed through phantom studies. The system was found to be capable of imaging bioluminescent signals from as deep as 1.5 cm within the animal body. The accuracy of the surface reconstruction was seen to be within 4 % which further ensures accurate measurements using this system.

CHAPTER 1
Introduction

Medical imaging has seen many advances in the 20th century. Techniques such as X-ray, computed tomography (CT) and magnetic resonance imaging (MRI) allow precise charaterisation of tissues with a spatial resolution of $\sim 100\mu m$ [1]. As the acquisition times for these modalities is gradually reduced they are finding applications in functional imaging. Functional imaging techniques refer to the imaging of dynamic and biochemical processes in the body. While the scope of functional imaging can range from study of tissue physiology e.g., blood flow, tissue metabolism and digestive processes, they can also be extended to the molecular level. Functional imaging techniques like positron emission tomography (PET) and single photon emission tomography (SPECT) which require radioisotope to be injected into the blood allow the study of molecular and cellular features of biology and disease [1]. However the spatial resolution of these techniques is considerably lower than the anatomical imaging modalities but they provide information which would otherwise be available only through invasive procedures.

In the conventional *in vivo* experimental strategies, temporal information about biological processes is often obtained through repeated, time-stacked animal sacrifice. If fine temporal analysis is sought during the observation of key biological stages in normal development or disease, the number of animals required per experiment can be quite large. Moreover the inter-animal variability can induce considerable error in the studies. Noninvasive imaging methods enable molecular assays to be conducted *in vivo*, and they comprise the emerging field of molecular imaging in which a variety of imaging modalities are used for real-time visual monitoring and assessment of biological processes in living animals. Molecular imaging methods greatly reduce the number of animals required for statistical significance, sometimes by as much as an order of magnitude, because they allow the comprehensive assessment of each animal over the entire duration of the process under investigation.

1.1 Optical Imaging Overview

The idea of using light for diagnostic and therapeutic applications is centuries old. However in the recent decades with the development of more suitable light sources, sensitive detectors and a better understanding of biological processes at a molecular level, research in the field of optical imaging has picked up considerable momentum. In the biophysics and biomedical communities diffusing photons are used to reveal body function and structure. Mammalian tissues are relatively opaque, and light transmitted through the tissues or from internal biological light sources located within the tissues of small animals can be detected externally using sensitive low-light imaging systems. Whole-body imaging of light that is generated within the body and transmitted through tissue is an exciting approach for studying biological processes in laboratory animals. Optical imaging presents several potential advantages over existing radiological techniques. First, the radiation is non-ionizing, and therefore longitudinal measuremments can be made over a period of time. Second, optical methods offer the potential to differentiate between soft tissues, due to their different absorption or scatter at near - infrared (NIR) wavelengths, that are indistinguishable using other modalities. Third, specific absorption by natural chromophores (such as oxy-haemoglobin) allows functional information to be obtained non-invasively.

1.1.1 Optical Properties of Tissues

The first significant attempt at diagnostic imaging using optical radiation was made by Cutler [2], who transilluminated a female breast with a bright light source in a darkened room. However, even these early experiments revealed that the multiple scattering which occurs when light propagates through tissue causes features below the surface to appear extremely blurred. Therein lies ones of the biggest challenges of optical imaging. The optical properties of tissue, namely, scattering and absorption, govern the ability to detect light from the light sources.

The scatter coefficient (μ_s) is a parameter that defines the amount of photon scattering that takes place as light interacts with the tissue. An easier way to understand it is as the inverse of the distance travelled by a photon in the tissue

before it is scattered. The μ_s of many soft tissues has been measured at a variety of optical wavelengths, and is typically within the range $1 - 100\,mm^{-1}$ [3]. As a consequence, measurements of transmitted intensity through more than a few millimetres of tissue are dominated by scattered light, and imaging contrast is largely governed by photon interactions at the surface. The severity of scatter generally decreases with increasing wavelength, although the choice of wavelength is complicated by the need to consider the relative optical characteristics of the different tissues under investigation, the availability of suitable sources, and the sensitivity of the detector. The characteristic scatter of tissues is commonly expressed in terms of the transport scatter coefficient $\mu_s' = \mu_s(1 - g)$, where g is the mean cosine of the single scatter phase function.

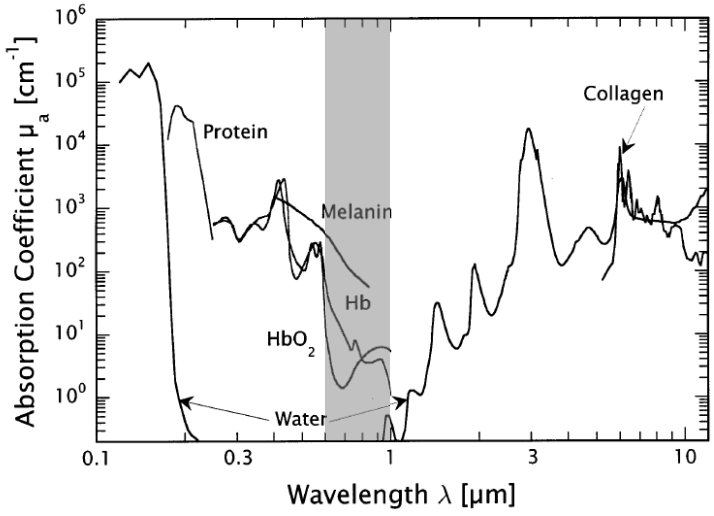

Figure 1.1: Optical absorption coefficients of major chromophores in the 0.1 - 12 μm spectral range with the shaded region showing the NIR window.

The other fundamental charateristic of tissue optics is the absorption coefficient μ_a, which characterises the amount of light energy absorbed as light propagates through the tissue. Emission in the near infra-red (NIR) range (> 600 nm) is favourably transmitted through tissues due to the relatively low absorption at these wavelengths [4]. Haemoglobin is the primary absorber of light *in vivo* in this spectrum, and its interference can even be detected in biochemical assays where optical measurements are made in the presence of tissue homogenates. The haemoglobin

absorption spectrum significantly decreases above 600 nm, and the absorption due to water content begins to rise at 900 nm [5]; this defines the optimal spectral window for optically-based imaging strategies.

1.1.2 Optical Imaging Techniques

Imaging modalities in the optical regime have been based on the use of scatter and absorption properties of biological tissue. The abundance of endogenous and exogenous contrast agents allow a wide range of optical imaging modalities with varying specificity and selectivity. In this section some of the common optical imaging modalities based on the aforementioned contrast agents are discussed.

1.1.2.1 Small animal imaging with endogenous contrast agents

Endogenous contrast agents are those substances that originate from within an organism, tissue, or cell which are sensitive to light in specific wavelengths. There are several naturally occuring intrinsic molecules which are photoactive in the ultraviolet (UV), visible and NIR spectral ranges, for example, aromatic amino acids, DNA, melanin in the UV region; haemoglobin in the visible region; and water and fat in the NIR region. This feature is useful for generating optical contrast which can be used for diagnosis of various pathological conditions. Small animal imaging based on endogenous contrast is performed usually by reflectance spectroscopy, employing fluorescence absorption or Raman scattering detection techniques [6]. As mentioned previously, the shallow penetration of light in the visible and UV ranges due to high absorption limits its applicability to superficial tissues. Light in the NIR window can be used to image deep tissues based on differential ratio of absorption by deoxyhaemoglobin and oxyhaemoglobin in normal and pathological tissues allowing the localisation of abnormal conditions. However, analysing the spectral reponse of diseased and normal tissues using endogenous chromophores remains difficult despite the availability of sophisticated image reconstruction algorithms.

1.1.2.2 Small animal imaging with exogenous contrast agents

Optical imaging benefits from the use of exogenous contrast agents to increase the sensitivity and specificity of its diagnostic potential. These contrast agents

are less dependent on intraspecies variations and can provide unique information regarding the functional status of tissues. Any biocompatible molecule that absorbs, emits or scatters light of an appropriate wavelength can serve as an optical contrast agent.

Exogenous contrast agents include non-specific imaging agents like Indocyanine Green (ICG), receptor-specific agents and Photodynamic Therapy (PDT) agents and functional imaging agent. Non-specific agents rely on the differential accumulation of the agent in the pathological tissues [7]. While the non-specific nature of these agents permits their use in screening a variety of tumours, they are retained in a number of non-tumour cases resulting in false positives. Because of the low specificity and selectivity of the non-specific probes, many studies are currently evaluating new site-specific imaging agents [8].

With advances in molecular biology, it has been seen that pathological cells tend to overexpress certain receptors which can be used for the delivery of site-specific imaging agents. Most of the studies by this mechanism have been performed with radiolabelled antibody conjugates, that have been adopted for optical imaging in small animals [9]. The applicability of this technique is however hampered by the low diffusion rate to tumours, rapid uptake by the liver and the potential to elicit adverse immuogenic reactions. PDT agents are another class of exogenous imaging agents that are preferentially retained in various types of tumours.

Functional imaging agents have the ability to probe biochemical activities *in vivo* and correlate the data with pathological conditions. There are two types of functional agents that have been studied extensively so far. The bioluminescent markers, like luciferases, are biological sources of light that require chemical substrates for light emission, and fluorescent markers, like Green Fluorescent Proteins (GFP) require excitation light for emission. Fluorescent markers absorb photons of light of particular wavelengths, creating an excited molecular state that subsequently releases light of an altered or shifted wavelength. They therefore do not need a chemical substrate, can be biocompatible, sensitive, and can be conjugated to small molecules, antibodies, or other proteins. However, the use of fluorescence probes can be constrained by the combination of absorption and scatter of both

excitation and emission light, and the natural autofluorescence of mammalian tissue. Nonetheless, fluorescence probes have been successfully used to follow tumor growth by implantation of GFP-expressing tumor cells; to detect tumor receptor density, distribution, and activity using conjugates of fluorophores to antibodies or antibody fragments; and to study actions of proteases using protease-sensitive or protease-specific probes [10]. Additionally, subsurface imaging of fluorescence can be brought to the subcellular level by the use of more invasive procedures, such as intravital microscopy. The autofluorescence of mammalian tissues is the single most important source of background noise in the transillumination based strategies and this may have significant effects on signal to noise ratios in the detection of fluorescence *in vivo*.

Bioluminescence, the action of luciferases on their substrates, releases light continually (as long as enzyme and substrate are present), enabling long acquisition times for the detection of very weak signals from deeper within the tissue. This continual signal precludes the use of time-resolved methods, but the absence of autoluminescence in mammalian tissues results in very high SNR, yielding very sensitive measurements.

1.2 Motivation and Objectives

As mentioned in the previous section, bioluminescence imaging (BLI) is based on the sensitive detection of visible light produced during enzyme (luciferase)-mediated oxidation of a molecular substrate when the enzyme is expressed *in vivo* as a molecular reporter. Bioluminescence at the emission wavelength firefly luciferase (560 nm) can be imaged as deep as several centimeters within tissue, which allows at least organ-level resolution. This technology has been applied in studies to monitor transgene expression, progression of infection, tumor growth and metastasis, transplantation, toxicology, viral infections, and gene therapy, protein interaction and cellular dynamic in small animal models [11]. BLI is simple to execute and enables monitoring throughout the course of disease, allowing localization and serial quantification of biological processes without killing the experimental animal. This powerful technique can reduce the number of animals required for experimentation

because multiple measurements can be made in the same animal over time, minimizing the effects of biological variation. One of the biggest advantages of BLI is that as the cells divide and migrate through the body the BLI reporter is replicated with each cell division. This way the entire course of an infection or metastasis can be studied over time.

Bioluminescence is appealing as an approach for *in vivo* optical imaging in mammalian tissues because these tissues have no intrinsic bioluminescence; therefore, images can be generated with remarkably high signal-to-noise ratios.

(a) The North American Firefly (b) The Moon Jellyfish

Figure 1.2: Naturally occuring organisms which display bioluminescence

A variety of different bioluminescent systems have been identified in nature, each requiring a specific enzyme and substrate. The sensitivity of detecting internal light sources is dependent on several factors, including the level of luciferase expression, the depth of labeled cells within the body (the distance that the photons must travel through tissue), and the sensitivity of the detection system. Key advances in detector technology have led to substantial improvement in sensitivity and image quality. Photons are detected by specialized charge coupled device (CCD) cameras that convert photons into electrons after striking silicon wafers. CCD cameras spatially encode the intensity of incident photons into electrical charge patterns to generate an image. For BLI, the noise of the systems is reduced by super-cooling the CCD camera and mounting the camera in a light-tight box. These cameras are run by a computer for image acquisition and analysis. Second-generation cameras that

are much smaller and can be accommodated on bench tops make the technology feasible and practical for day-to-day experimentation.

Bioluminescence tomography (BLT) is the reconstruction of bioluminescent source by taking measurements on the surface of the body. The disadvantage in this case is that the exiting signals on the surface are very weak. More over the inverse problem associated with the reconstruction of the source distribution is a very challenging problem. Recent studies have shown that the complexity of the inverse source problem can be further reduced by multi-spectral information in three dimensions. This process is carried out in four steps.

1. Acquire two dimensional bioluminescence images in different spectral bands and generate a light exitance model.

2. Acquire multiple views to create a surface map of the animal and register the previously acquired exitance map and the surface map.

3. Solve the forward problem where the exitance map is simulated based on an assumed anatomical information and source distribution.

4. Solve the inverse problem to find the source distribution by minimizing the difference between the simulated and measured exittance map.

The objective of this project is to tap into the advantages of BLT and reduce the complexity of the problem by adding the modalities mentioned earlier to reduce the ill-posedness of the problem. My research leading upto this thesis focussed on the design and development of an imaging platform for multi-spectral multi-view bioluminescence tomography which can fulfil steps 1 and 2 mentioned above.

1.3 Thesis Outline

The following chapters give an in depth introduction to the physical and biological aspects of bioluminescence and a detailed description of the instrumentation developed and a formal characterisation of the capabilities of the system. This is followed by the results obtained from the system and a discussion of the same.
Chapter 2 looks at the fundamentals of bioluminescence from a biological viewpoint

and we go on to look at the applications of BLT that have been explored in medicine. We also discuss the current state of instrumentation available for BLT both in the industry and in the academia.

Chapter 3 which forms a central part of this thesis gives an in depth description of the instrumentation as we look at each aspect of the system; the control design of the automation, the multi-spectral acquisition system for the bioluminescence signals, the stereo system for generation of the surface map, the registration of the two maps to generate the final dataset and finally the software controlling the system.

Chapter 4 discusses the calibration of the platform where we look at the accuracy of the mechanical aspect of the system and also the noise introduced by the optical components in the system.

Chapter 5 gives a detailed evaluation of the system where we explain the charaterization of the system capabilities using calibrated phantoms. We will look at the signal to noise ratio charateristics based on variation in the depth of the bioluminescence source as well as its power.

In *Chapter 6* we look at the results of the imaging experiments, starting off with a description of the experiment protocol and follow up with results highlighting the exittance map generation and the surface map acquisition and finally the combination of the two.

Chapter 7 summarises the research and we look at the direction of future research and ways to expand the utility of this platform onwards to other optical imaging modalities.

CHAPTER 2
Bioluminescence Imaging

Bioluminescence imaging (BLI) developed as a result of the synthesis of two technologies namely, biological reporters and ultra-sensitive charged coupled device (CCD) cameras for low-light imaging. It utilizes light-generating enzymes, most commonly luciferases, as an internal biological light source that can be genetically programmed to report the presence or activation of specific biological events.

2.1 Fundamentals of Bioluminescence

The family of luciferase enzymes, present in certain bacteria, marine crustaceans, fish, and insects., consists of proteins that can generate visible light through the oxidation of an enzyme-specific substrate in the presence of oxygen and, usually, adenotriphosphate (ATP) as a source of energy.

2.1.1 The Bioluminescence Reaction and Light Generation

Each time a photon of visible light is emitted at room temperature, by a living organism or chemicals in a test tube, the reaction responsible for the creation of the excited state, and thus for the emission, must be a very exergonic process, because a photon of green light ($\sim$ 500 nm), for example, corresponds to approx 60 kcal per mole (or about eight times the energy released by the hydrolysis of ATP to ADP). It must also happen in one step because the pooling of the energy of two or more exothermic reaction steps can occur only in rare conditions not encountered here [12].

$$\text{Luciferin} \xrightarrow{\text{luciferase, } O_2} \text{intermediates} \longrightarrow P^* \xrightarrow{k_F \approx 10^8\ s^{-1}} P + h\nu$$

The actual emission of bioluminescence (which is a chemiluminescence that requires an enzyme) is the extremely rapid final process of a usually multistep reaction, in which the penultimate step is the generation of a molecule in an electronically

excited state, P*. The excited state of the emitter has a very short lifetime. It holds the reaction energy for no more than a few nanoseconds before releasing it in the form of a photon.

2.1.2 Luciferase Expression

The light from these enzyme reactions typically has very broad emission spectra which frequently extend beyond 600 nm. It has been shown that the luciferase structure can itself alter the color, as in the firefly, where single amino acid substitutions in the luciferase result in significant shifts in the emission spectrum [12]. The following are the emission spectra for four commonly used bioluminescence reporters.

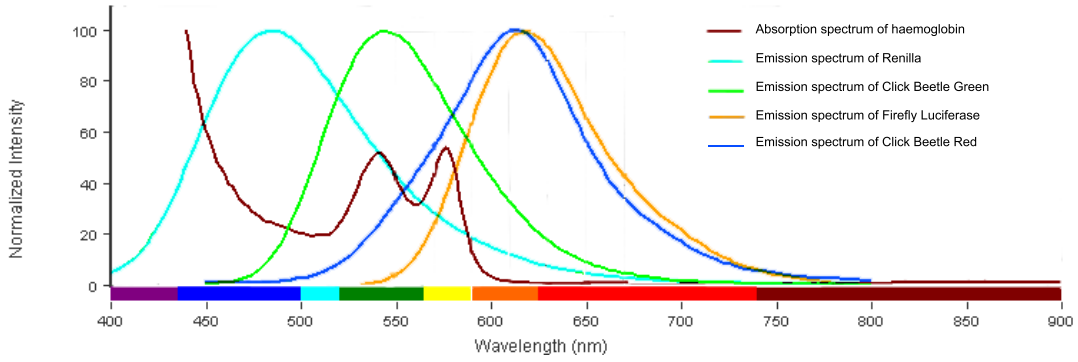

Figure 2.1: Emission spectra of some commonly used Bioluminescence Reporters

As can be seen in Figure 2.1 Firefly Luciferase and Click Beetle Red are the only two bioluminescence reporters which primarily emit light in the NIR window and thereby making them suitable for *in vivo* imaging applications. However a larger part of the emission spectrum of Click Beetle Red overlaps with the absorption spectra of haemoglobin and thus Firefly Luciferase with 60 % of its emission over 600 nm is the more popular choice as a reporter for *in vivo* imaging owing to the higher permeability of its emission through tissue. The Renilla luciferase which emit blue light at a peak of 480 nm can serve as a control for expression with firefly luciferase as these two enzymes distinguished biochemically (they use two different substrates) and also spectrally. However the absorption properties of tissues makes it unsuitable for *in vivo* imaging. Models of photon diffusion through tissues have indicated that

as few as one hundred bioluminescent cells are detectable at subcutaneous tissue sites while approximately 10^6 cells would be required to generate detectable through 2 cm of tissue [13]. These predictions have been made with the assumption of a light output of 30 photons per second per cell at a wavelength of 650 nm. The levels of reporter gene expression determines the extent to which it can be detected *in vivo*. The light output per cell can be measured in culture and can be used as an *a priori* assessment of the sensitivity of detecting a signal in a given animal model.

2.1.3 Considerations in In Vivo Bioluminscence Imaging

As has been mentioned in Section 1.1.1, for light in the NIR window the absorption length in tissue is $\sim 2cm$ while the effective length of scattering is much shorter at $\sim 0.5mm$. However during whole-body optically based imaging strategies light may be scattered multiple times, depending on its pathlength and wavelength, which renders the emitted light highly diffuse and lacking in spatial resolution. Also there is large variation in the optical properties in tissues from different mice [13]. It has also been reported that light is transmitted more efficiently transmitted in white or hairless mice because melanin absorbs substantial amounts of light and also light is scattered more by dark fur [14].

Another factor to be considered is that luciferases are oxygenases. An oxygenase is any enzyme that oxidizes a substrate by transferring the oxygen from molecular oxygen. This oxygen requirement may reduce the use of luciferase in anaerobic environments. Therefore in studies where the cell may become anaerobic, light may not be emitted in proportion to luciferase expressed. The oxygen concentration required for efficient light production is well below the level of oxygen found in living mammalian cells. Thus the reduced light production due to hypoxia may coincide with the death of cells.

2.2 Applications of BLI

2.2.1 Applications in Oncology Research

The most common application of BLI in cancer research involves the **detection of cancer in internal organs**. One of the earliest studies involved the

implantation of Luciferase expressing tumor cell lines into animal models and the bioluminscent signals were then measured and spread followed over time [15]. Subsequent experiments in this study examined the response of the tumour to various chemo- and immunotherapies. This and other studies show that luciferase expression correlates with tumor volume and mass. This shows that luciferase expression serves as a reliable measure of tumor burden which offers significant advantages in preclinical studies. BLI-based measurements allow the study of tumor cells implanted at tissue sites of their origin and enable early detection of tumor growth.

BLI provides an opportunity to detect small numbers of malignant cells expressing luciferase rapidly over the entire body of a mouse. This capability has enabled the **study of metastatic and minimal residual disease states** in animal models. In a recent study bone marrow metastases were quantitatively evaluated using BLI [16]. While bone marrow metastases cannot be detected by radiographic techniques, BLI was able to detect the locations of these lesions following intracardiac injection of tumor cells. Despite the recent improvements in cancer therapies, residual disease remains a major therapeutic target. For this reason, animal models that enable effective evaluation of therapies that target small number of tumor cells like BLI are essential for development of next generation cancer therapies.

The enzymatic production of light is ATP-dependent in luciferase based reporters. This makes BLI suitable for **monitoring metabolic activity**. In one of the studies where an animal model was transfected with a malignant melanoma , the light emission was seen to increase with tumor growth [17]. After 3-4 weeks it was possible to detect a pattern of bioluminescent signal that indicated a necrotic central region of the tumor, despite the fact that no change was observed on external examination. Thus luciferase reporters serve as metabolic indicators which can be a better measure of tumor burden.

As an alternative to simply tracking the location and number of tumor cells in an organism via the use of luciferase, it is possible to link the activity of luciferase

enzyme to specific biological events. In this way it is possible to **monitor particular steps in tumorogenisis** (such as hypoxia, angiogenesis or metastasis). As mentioned in section 2.1.2 *Renilla* luciferase and firefly luciferase have exclusive and independent expression. Thus if firefly expression is linked to to a biological event within the tumor, while every tumor cell also constituively expresses a secondary signal based on the *Renilla* luciferase, it is possible to assess what portion of tumor cells will need to undergo a molecular event in order to produce a given reponse. This application of BLI is referred to as dual reporter strategy.

2.2.2 Applications in Immunotherapy

The migration of immune cell populations is key to an organism mounting an effective immune response and understanding these patterns in context of rodent models has recently been the subject of investigation. Intravital fluorescence microscopy has been used to visualise cellular interaction and migration in real time however they are restricted to superficial tissues (few millimeters) and are affected by motion artifacts due to respiration and cardiac function. BLI is one of the macroscopic methods that offer rapid whole body analyses of cell movement and its non-invasive nature allows long study periods of days or weeks [18]. As the migratory pathways of the immune cells within the body relate to temporal changes of immune response, localisation of these cells maybe useful for local delivery of therapies. The techniques that have traditionally been used to monitor immune cell distributions in tissues, such as flow cytometry and immunofluorescence cannot readily assess the dynamic changes that take place on a whole body scale. BLI has utility to reveal these global patterns that are necessary for a systems approach to immune cell therapies.

2.2.3 Applications in Gene Therapies

Nucleic acid-based therapies offer the potential of gene replacement, potentiating conventional therapies or reducing expression of viral gene products, oncogenes or mutant proteins. Efective evaluation of new treatment stratergies for malignant disease will require that animal models that are used closely resemble the human diseases they are designed to model. Disease in these models can involve multiple

organ systems and imaging is essential for assessment of tumor burden at deep tissue sites. Moreover as nucleic acid-based techniques are developed, accessing expression data *in vivo* will become key to optimizing these therapies. The utility of BLI for this purpose has been demonstrated in several different therapeutic areas, especially oncology [19].

In many inherited human diseases, lifelong expression of the gene is a therapeutic objective. Many gene delivery strategies result in transient reponse and are thus unsuitable. Successful application of BLI in this respect was demonstrated in [20] where using an *in utero* gene model lifelong expression of cells lining the abdominal wall was monitered. BLI was used to monitor the reporter gene expression patterns throughout the lifetime of the mice beginning at gestational age of 18 days over a 24 month study period. *In utero* gene transfer offers the possibility of gene replacement at a time where immune tolerance to the expressed therapeutic protein may be induced. Advances in gene targeting will further enhance the possibility to direct the integration of the therapeutic DNA to regions of the genome where the likelihood of adverse events is diminished.

2.2.4 Summary

The use of reporter genes with *in vivo* detectable signatures, has extended the traditional tools used by molecular biologists based on studying gene regulation in cells, into the spatio-temporal domain. The use of reporter genes allows the non-invasive monitoring of intact cells in living animals under the contextual effect of the intact functional organs. The use of multi-modality approaches [21, 22] provide structural information that can be linked with the functional information obtained via BLI which will help in improving the localisation studies of molecular therapies. BLI has been used to generate high quality spatio-temporal information about expression and gene delivery. The utility, cost, flexibility and especially the high quality predictive data generated from whole animal cellular and molecular imaging define a key advantage for the development new techniques in molecular therapies.

2.3 Current bioluminescence imaging instrumentation

As mentioned at the beginning of this chapter, the advances in BLI were made possible through the development of high-sensitivity low-light charge-coupled device (CCD) cameras. Sensitive CCD cameras employ several types of architecture: intensified and cooled CCDs or variations thereof [23, 24]. Intensified detectors use photocathodes to convert captured photons to electrons that are amplified and then converted back to photons using a phosphor screen and finally detected on CCD. The limitations of the photocathode to specific regions of the light spectrum can reduce their sensitivity. CCD cameras can be cooled down to -120° C to reduce thermal noise and thereby improving the sensitivity of the CCD. In addition, the light collection capabilities of the lenses employed in these systems, the distance between the detector and the subject will also determine the sensitivity of detection. There are also camera systems that have been specifically designed for the detection of weak bioluminescence signals in animal models incorporate design features that optimize signal detection. In the following sections some of the successful BLI instrumentation developed in the industry and the academia are described.

2.3.1 Xenogen Corporation

Xenogen Corporation has a series of vivo bioluminescence and fluorescence imaging system, which include both 2D and 3D vivo molecular imaging system. They have also recently published studies exploring the use of their system for multi-spectral imaging [25]. We will be looking at two systems from the IVIS ® series - IVIS 200 series and IVIS 3D series.

2.3.1.1 IVIS ® Imaging Systems 200 series

This is a single-view fluorescence and bioluminescence imaging system. Researchers can use this single system to perform quantitative in vitro and in vivo assays using reporter cells tagged with bioluminescence. One of the unique features of this instrument is a large diameter (5 inch) custom lens with 4-position zoom carousel [26].

The lens provides high light collection at f/1, an adjustable field of view from 4

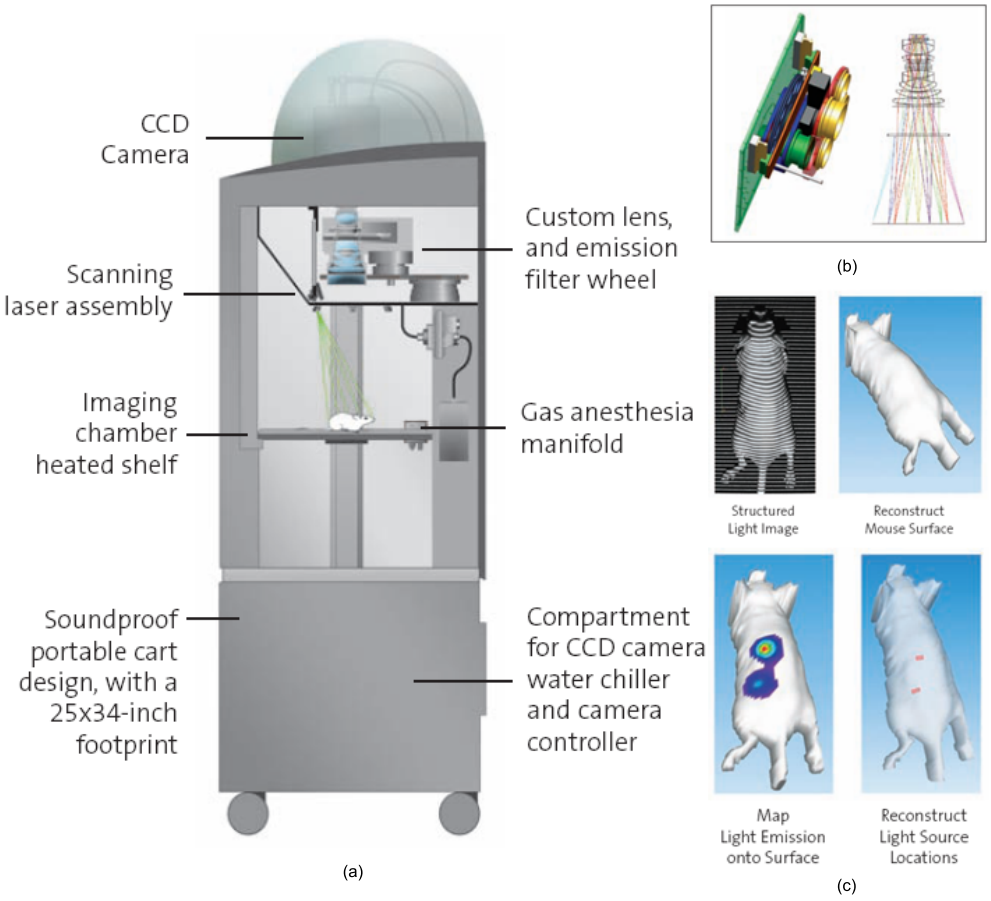

Figure 2.2: The IVIS Imaging System 200 Series: (a) System Layout, (b) Lens Mechanism and (c) Reconstruction Results

– 23 cm, uniform light collection, and superior resolution with single cell sensitivity for in vitro or ex vivo use. A laser scanning device provides the 3D surface topography used in diffuse tomographic reconstructions of internal sources. The system includes premium animal handling features such as a heated stage, laser alignment of animal position, and an integrated gas anesthesia system.

Spectral imaging uses measurement data from a sequence of images filtered at different wavelengths, ranging from 560 nm to 660nm, to determine the depth and location of a bioluminescent reporter. Meanwhile it has ability of controlling 24 filters, which significantly expand the research opportunities of bioluminescent imaging. Diffuse tomography algorithms under development can be used with the IVIS Imaging System 200 Series to reconstruct the location and brightness of bioluminescent

sources inside the mouse. This algorithm utilizes single-view surface topography and luminescent image data. The accuracy of this system is on the order of 13 mm.

2.3.1.2 IVIS ® Imaging Systems 3D series

The IVIS 3D offers rotational axis imaging of bioluminescent light sources within living animal models. With a unique optomechanical design, the IVIS 3D provides eight imaging views about the longitudinal axis of the animal without physically rotating the animal or the CCD camera [26].

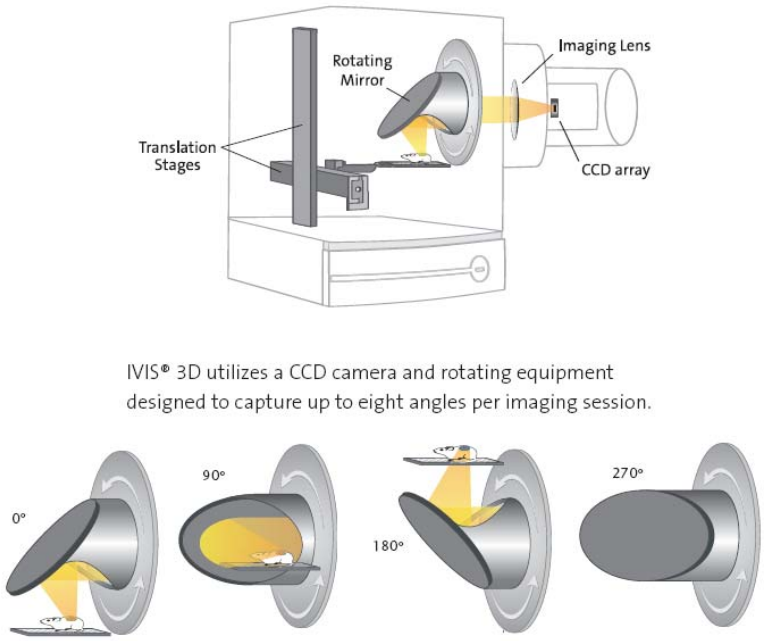

Figure 2.3: The optomechanical system for multiview imaging in the IVIS Imaging System 3D Series

As the first and only commercial 3D bioluminescent imaging system, Xenogen technology enables researchers to better visualize, track, and understand biological processes in living animals. The light-tight low background imaging chamber allows the IVIS 3D to be used in standard lab lighting environments. The IVIS 3D is highly automated, with all hardware motor movement and imaging parameters controlled by software. The surface extraction method employed in the 3D series is the same as in the 200 series. The 3D series presents another stratergy for aiding the process of imaging bioluminescence signals. It is also equipped with the standard animal

handling features included in all Xenogensystems like a heated sample chamber and full gas anesthesia system.

2.3.2 The Simultaneous Multispectral Multiview Bioluminescence Tomography Imager

This system is the latest in a series of bioluminescence tomography systems that have been developed at the Bioluminescence Tomography Laboratory, University of Iowa [27]. In this study [28] , a system which is capable of simultaneous multispectral and multiview acquisition of bioluminescence signals is presented. The motivation behind this design is the relatively long acquisition time of weak bioluminescent signals. When acquiring multispectral information over 10 spectral bands, the time taken to complete the acquisition may reduce the temporal resolution of the data obtained. This design performs simulatenous acquisition with the use of a special mouse holder, referred to as the rainbow holder.

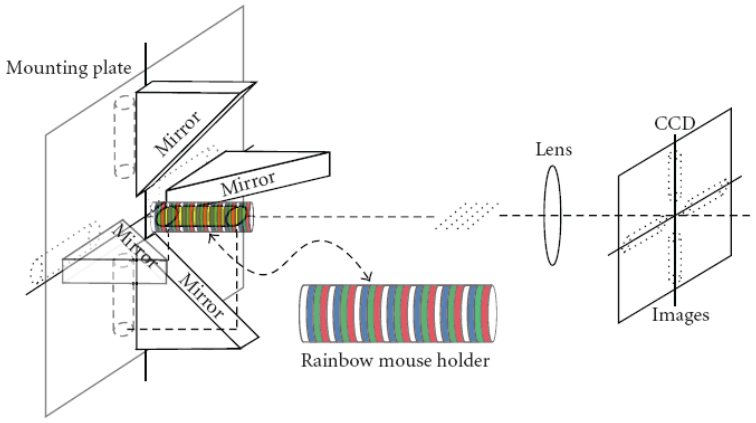

Figure 2.4: The system design for simultaneous acquisition of multispectral and multiview data

The schematic shown in figure 2.4 describes the operation of this instrumentation. The system uses a very sensitive camera with a quantum efficiency of more than 80 %. The multiview system is based on a stage design that was discussed in an earlier publication [29] which incorporates mirrors to acquire multiple views of the mouse at the same time. The multispectral information as mentioned earlier is obtained using a cylindrical tube as a mouse holder with interleaving filter bands

which seperate the emitted bioluminescent signal into spectral bands.
The major issues with this design arise with the spectral resolution obtained by the use of the rainbow filter. The light at some pixels is obtained from more than one spectral band and thus the resolution can only be improved by taking data from pixels representing only the central bands on the tube. This results in loss of data, but the study shows that this drawback can be avoided by the development of unmixing algorithms. This design is a feasible method for bioluminescence tomography.

The previously discussed designs have been summarised in the following table,

Specification	IVIS ® 200	IVIS ® 3D	Multispectral Multi-view Imager
Camera Sensor	CCD	CCD	CCD
Imaging Pixels	2048 x 2048	2048 x 2048	1340 x 1300
Quantum Efficiency	85 %	85 %	80 %
Pixel Size	$13.5\mu m$	$13.5\mu m$	$20\mu m$
Minimum Pixel Resolution	$20\mu m$	$20\mu m$	$75\mu m$
f-stop Range	f/1 – f/8	f/1 – f/16	f/1.4
Spectral Imaging Filters	6	3	3
Number of views	1	8	4
Surface map extraction	Yes	Yes	No

Table 2.1: Comparison of state-of-the-art Bioluminescence Imaging Instrumentation

CHAPTER 3
Instrumentation Overview

As discussed in section 2.3, the current instrumentation used by biologists and researchers for bioluminescence imaging and tomography of small animals is based on two strategies: multiview acquisition and multispectral acquisition. The inverse source problem associated with BLT is especially challenging and reducing the ill-posedness of the problem by making a comprehensive set of measurements is the primary motive behind these strategies.

It has been shown that three-dimensional (3D) information about the emission of bioluminescence signals from the animal model can be acquired through a single view acquisition [25]. The inherent diffusive nature of light poses a challenge to obtaining a unique solution to the inverse problem. Acquiring images at multiple views will help improve the uniqueness of the solution [22]. Thus instrumentation that acquires images over a 360° field of view will by definition provide the most complete set of bioluminescence signal measurements. These images are acquired in discrete steps and the size of these steps decide the angular resolution of the resulting measurements. Therefore, the size of these steps becomes a critical factor.

Multispectral information acquisition has become one of the cornerstones of all optical imaging techniques including bioluminescence tomography (BLT) [29, 30].The problem of uniqueness associated with nonspectrally resolved intensity-based bioluminescence tomography is discussed in [30]. As mentioned in section 2.2 the applications of multispectral acquisition can be twofold. First, it is useful for imaging animal models based on the dual reporter strategies as it reduces the requirements on the spectral exclusivity and biochemical independence of the reporters. Second, it is useful for constraining the solution to the inverse problem. The efficacy of acquiring measurements at multiple spectral bands in reducing the uniqueness problem associated with the continuous wave (CW) Diffuse Optical Tomography has been shown in [31]. This has been extended for the inverse source problem associated with BLT in [30].

The drawback of the instrumentation described in section 2.3 is the relatively lower resolution, both in the angular (maximum of 8 views) and spectral (maximum of 6 spectral bands) measurements. This system is based on the above mentioned strategies for bioluminescence tomography of small animals with the objective to acquire images of bioluminescence signals exiting the animal model at a smaller angle seperation while incorporating provisions for a variable spectral resolution. This sets up a testbed for us to explore the effect of increasing the measurements on improving the solution of the inverse source problem.

3.1 Instrument Description

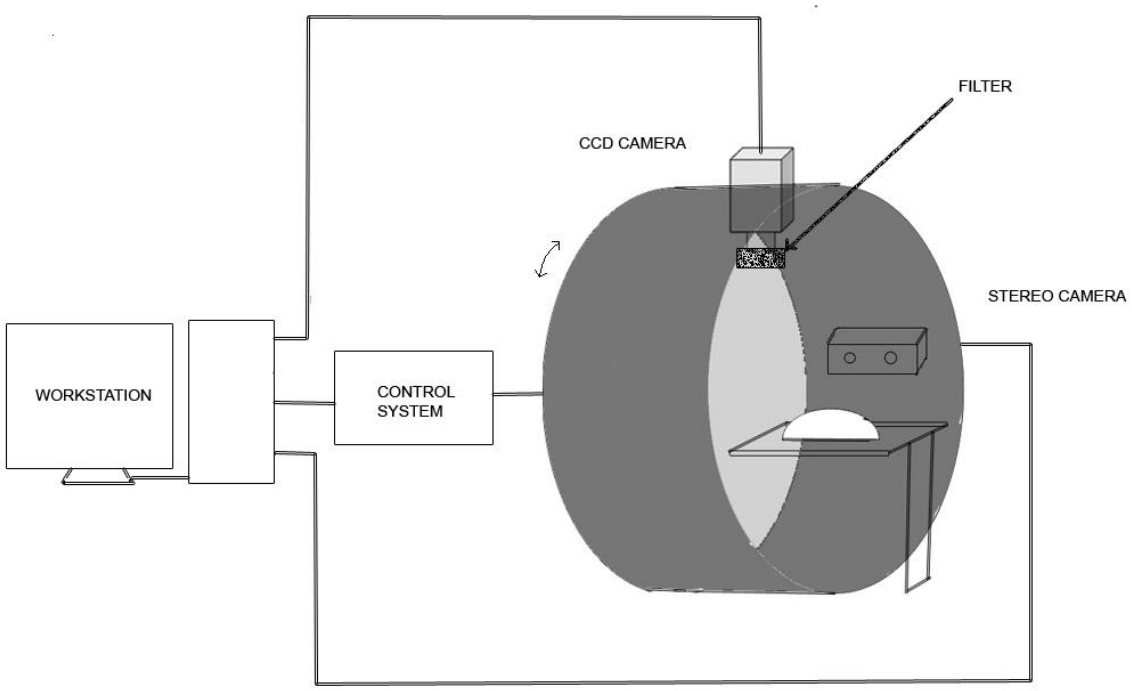

Figure 3.1: Bioluminescence tomographic imager system schematic for acquisition of multiview multispectral data

Figure 3.1 shows the architecture of the system. This system can be divided into three subsystems where each individual subsystem is controlled from the workstation.,

1. The Control System

   The variability in angular resolution obviated the use of mirrors to simultane-

ously acquire bioluminescence signals at multiple views as was done in [29, 28]. In this system the CCD camera is rotated around the animal model to acquire images at pre-specified angles.This subsystem comprises of the motor and the associated control hardware which allows the automation of the platform and independently controls the angular accuracy of multiview image acquisition.

2. The Acquisition System

   The multispectral data is acquired using interference filters in conjugation with the CCD camera.The CCD camera and the filter set are collectively referred to as the acquisition subsystem.

3. The Stereo System

   The stereo subsystem is a seperate two-camera system which acquires surface information of the animal model. This approach is unique to this system with the previously mentioned instrumentation using a scanning laser technique for extracting surface topography.

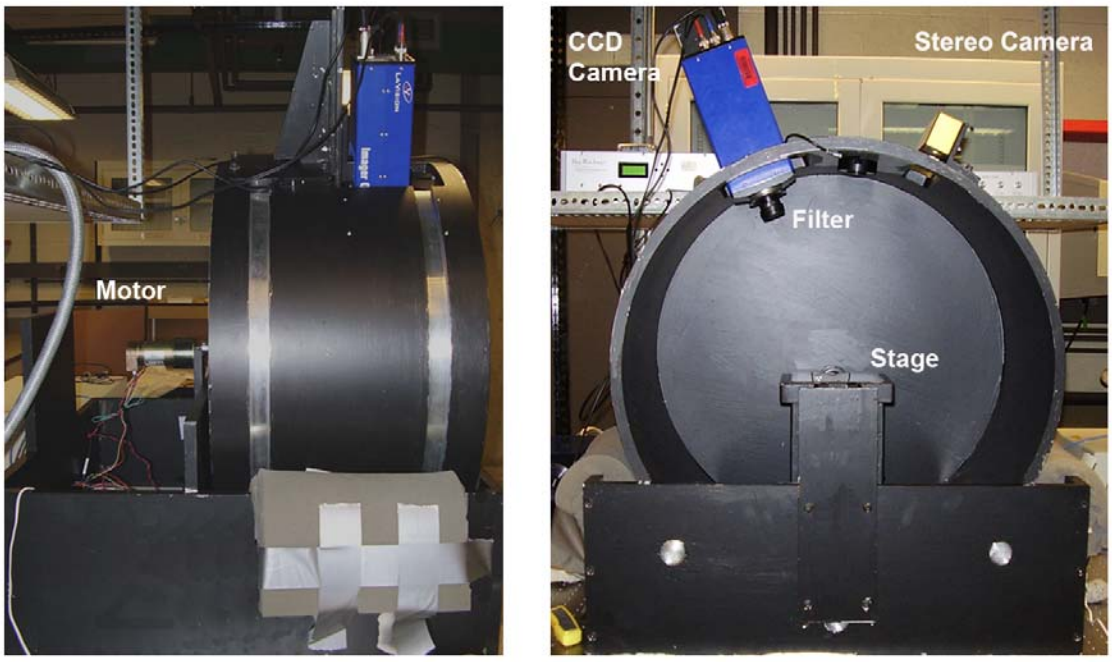

Figure 3.2: The Spectral Bioluminescence Tomographic Imager (sBLTI)

Detailed technical drawings of each component of the system shown in Figure

3.2 are given in Appendix A. In the subsequent sections each of the subsystems is discussed in detail.

3.2 The Control System

The instrumentation as shown in Appendix A comprises of two major components – the supporting base, the mounting drum. The camera mounts and the specimen stage form the minor components of the system. Due to the continous wave nature of bioluminescence signals, the speed of rotation of the system while acquiring multiview images was not considered to be an critical factor. The speed of rotation was fixed at $2°/second$. For this speed the load torque required to rotate the mounting frame with the attached cameras and the respective mounts was found to be 0.745 Nm. The objective behind the control system is to provide an angular resolution of 5°. At the highest angular resolution, the drum will rotate the camera by 5° and wait for signal from the workstation. The command signal from the workstation will provide the direction and degrees in which the system is to be rotated. The two main considerations while selecting the components of the control system were,

- The system should be capable of bidirectional rotation.
- The system must be held perfectly steady in between rotation during image acquisition.

3.2.1 System Components

The components forming this system are,

1. GM9234S031-R1 – Brushed DC motor with an optical encoder (PennEngineering Motion Technologies, Pittsburgh, USA)
2. DB300-0 – DC brush motor driver / Servo amplifier (3MeN Technologies, Click Automation, USA)
3. NI USB 6211 – 16-Bit, 250 kS/s M Series Multifunction Data Acquisition Device (DAQ) (National Instruments, Texas, USA)

4. 500 mA 12 V DC Adapter – Power Supply (Model: 273-1774, Radioshack)

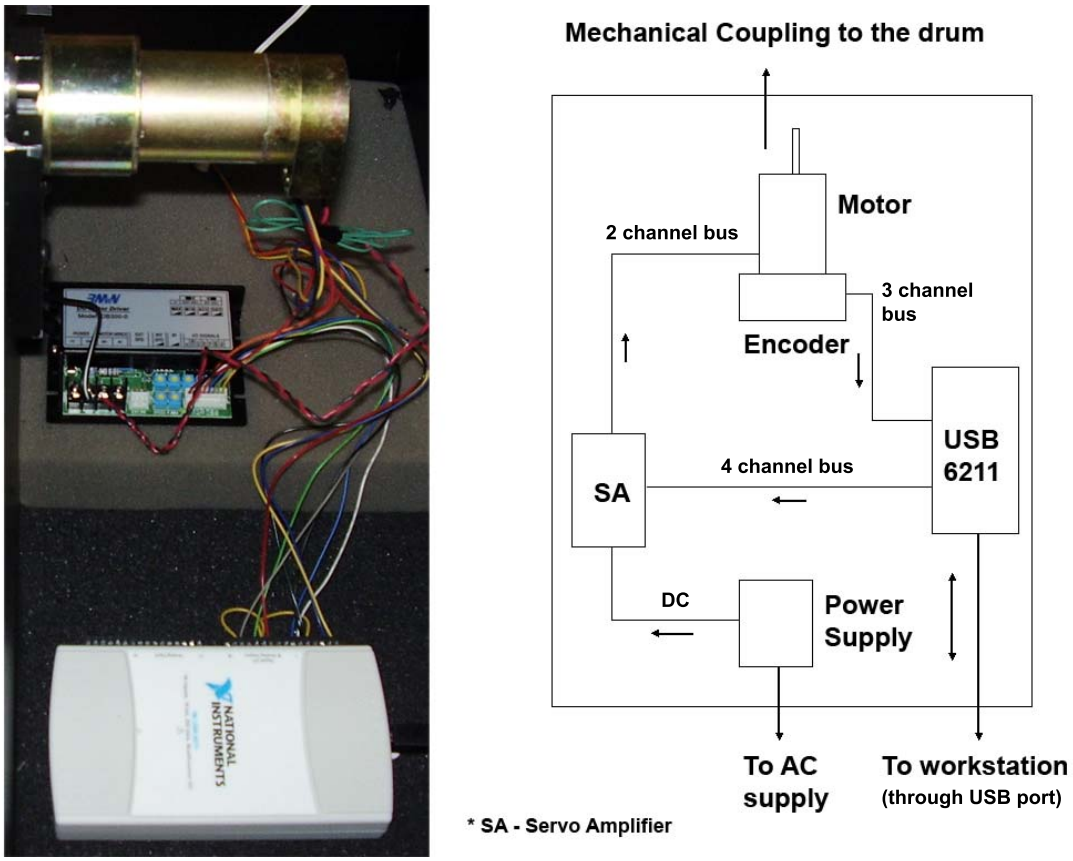

Figure 3.3: Control subsystem schematic

Figure 3.4 shows the control module as set up in the sBLTI and also the direction of command and control signals in the subsystem.

3.2.1.1 Brushed DC motor with optical encoder

The rotatory movement of the mounting drum in discrete steps suggests the use of stepper motor for its control. The stepper motor has the advantage of a high holding torque which is a critical requirement in this case. However, the stepper motor was not able to supply the torque required by this systm. The DC motor on the other hand is harder to control and requires a feedback device for accurate position control and was able to provide sufficient torque for rotation. The feedback device in this case is an optical encoder.

The optical encoder is a quadrature encoder and has two outputs called quadrature outputs (Channels A and B). There can be an optional third output: Index (Z), which happens once every turn. This is used when there is the need of an absolute reference, such as positioning systems. The optical encoder is used when higher RPM's are encountered or a higher degree of precision is required.

Phase	A	B
1	0	0
2	0	1
3	1	1
4	1	0

(a)

Phase	A	B
1	1	0
2	1	1
3	0	1
4	0	0

(b)

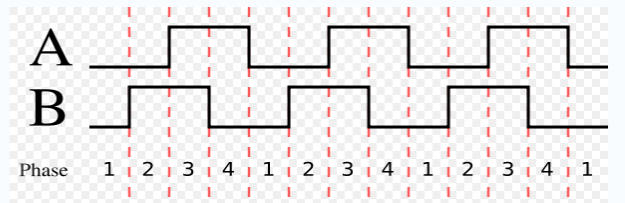

(c)

Figure 3.4: Gray Coded Optical Encoder: (a) Gray coding for clockwise rotation (b) Gray coding for counter-clockwise rotation (c) Two square waves in rotation

The signals shown in Figure 3.4 are decoded to produce a count up pulse or a count down pulse. For decoding in software, the A and B outputs are read by software (in this case Labview, either via an interrupt on any edge or polling, and the above tables are used to decode the direction). The angular accuracy is dependent on the resolution of the square waves. In our case the encoder has a resolution of 500 cycles per revolution.

Specification	Value
Reference Voltage	12 V
Continous Torque (Max.)	3.5 Nm
Torque Contant (K_t)	0.0232 Nm/A
Back-emf constant (K_e)	2.43 V/krpm
Peak Current	9.45 A
Friction Torque	0.0042 Nm
Rotor Inertia	0.0000042 Nm
Reduction Ratio of Gearbox (r)	218.4
Efficiency	0.73

Table 3.1: Summary of motor specifications of GM9234S031-R1

The table 3.1 provides a summary of the mechanical and electrical charateris-

tics of the DC motor used and Figure 3.5 shows the variation of speed and efficiency with torque as given in the product datasheet.

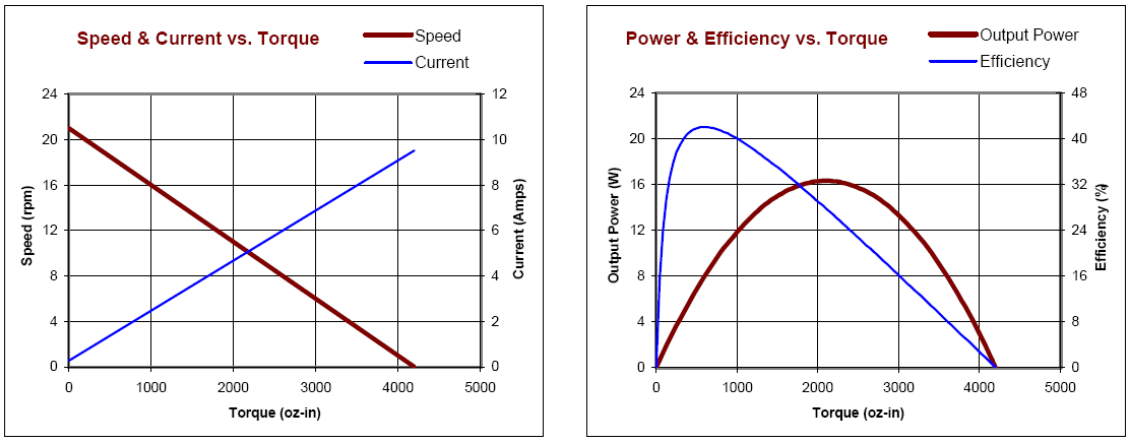

Figure 3.5: Torque Charateristics

3.2.1.2 Motor Driver

The basic theory behind motor control is that the motor's speed, torque and direction are controlled by switching or modulating the voltage input into the motor. Pulse Width Modulation (PWM) is the most common method used to vary the average voltage supply to the motor [32]. For example, for this 12 V motor if a PWM signal with 50 % duty cycle is applied the voltage input would be 6 V. The DB300-0 motor driver is also based on the PWM principle. It also supports both 12 V and 24 V and in this case the driver is set for 12 V by shorting the J2 connector. The schematic of this driver interface is given in Figure 3.6.

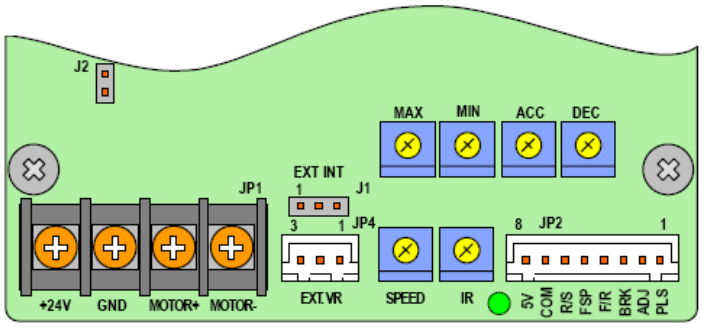

Figure 3.6: DB300-0 Interface

The motor can be controlled using this driver by two methods,

- Internal control through the 6 pin setting parameters where the maximum speed, minimum speed, acceleration, decceleration, torque and speed can be controlled for a constant operation.
- The more robust external control allows the interfacing of this driver with DAQ devices like USB 6211 through the JP2 8-pin connector. Table 3.2 details the function of each connector in JP2 and also the values at which it are operated. This is the method adopted for this system.

Pin Number	Name	Description	Value
1	PLS	None	NA
2	ADJ	Speed Control	0-5 V analog input
3	BRK	Determines the manner in which the motor stops when motor is turned OFF	Low
4	F/R	Direction control	High / Low
5	FSP	Full Speed Control (Motor runs at full speed if the pin is short with COM)	High
6	R/S	ON/OFF Control (ON when the pin is short with COM)	High / Low
7	COM	Ground	NA
8	5V	DC 5V 0,01 supply	NA

Table 3.2: Function Control description for the DB300-0

3.2.1.3 Multi-function Data Acquisition device (DAQ)

The National Instruments USB-6211 is a bus-powered USB M Series multifunction data acquisition (DAQ) module optimized for superior accuracy at fast sampling rates. It offers 16 analog inputs; 250 kS/s single-channel sampling rate; two analog outputs; eight digital input lines; eight digital output lines; four programmable input ranges (0.2 to 10 V) per channel; digital triggering; and two counter/timers. The NI USB-6211 is designed specifically for mobile or space-constrained applications.

In addition to LabVIEW SignalExpress (which is used as the control software in this our application), M Series data acquisition devices are compatible with Visual Studio .NET, C/C++, and Visual Basic 6.

3.2.1.4 Power Supply

In this control module the power supply is only responsible for driving the motor through the servo amplifier and the DAQ device is powered through the USB port of the computer. As mentioned in Table 3.1 the peak current, I, that can be handled by the motor is 9.5 A. However it is also mentioned that the torque constant of the motor is 0.0232 Nm/A and the reduction ratio of the gearbox is 218.4. The relation between these quantities is given by the motor equation,

$$Torque\,Supplied = \tau = K_t \times I \times r \tag{3.1}$$

For the given values of K_t, the maximum value of current I that can be supplied to the motor to ensure the torque supplied τ to be less than 3.5 Nm is calculated to be 696 mA. Any supply more than this value will result in the failure of the gearbox and thereby the motor. Also, the reference voltage for the motor is 12 V. Therefore, the DC power supply was chosen to be a 12V supplying a peak current of 500 mA. At this current value the torque supplied by the motor can be calculated using equation 3.1 was found to be 2.53 Nm which is well over our required torque.

The interconnections between the components of the control subsystem described above is give in Appendix B.

3.2.2 Control Design

The control design for the system is based on proportional control. In order to reduce the load torque τ_l of the system to within achievable limits (3.5 Nm), the mounting drum was augmented with counter-balancing weights which reduce the total torque required to rotate the drum.

The control design for the system reflects the effects of the addition of the counter-balancing weights. The addition of weights, while reducing the required

torque τ_l increases the total moment of inertia (I_t) of the system. This means that at higher speeds, when the system is dynamic in nature, the torque required to stop the rotation increases two-fold and the torque required to reverse the direction of rotation increases to four times the required value. This situation is detrimental to the motor and to the power supply and the gearbox in the motor is highly susceptible to breakdown. To avoid this situation, it is critical that the rotatory motion of the system be quasi-static in nature.

Quasi-static motion refers to a stepwise rotation, similar to a stepper motor, but with higher step resolution. As mentioned at the beginning of this section, the acquisition time is not considered to be a critical factor and thus the imaging system can afford to conform to this requirement. As previously stated, the rotatory motion is based on proportional control. Following are the keypoints of the control algorithm.

- The user is required to supply the step size, the velocity of rotation, the target angle, the aggresivity gain and the direction of rotation. These parameters are defined as follows,
  - Step Size – This is the angle over which the system rotates before stopping to fulfil the quasi-static constraint. Its default value is 30.
  - Target Velocity – This is the velocity to which the system accelerates before slowing down within one step. Its default value is 25.
  - Target Angle – This is the complete span over which the system is to be rotated. It can also be defined as the angular seperation between each view in the multiview image acquisition. It is initialized to zero.
  - Aggresivity gain – This is the proportionality constant between the total error and the control voltage. It default value is 0.8.
  - Direction of rotation – This is a boolean variable with a value 0 for clockwise rotation and 1 for anti-clockwise rotation.
- The units of angle and velocity used in defining the above said parameters are based on the encoder pulses.

- The control voltage V_o and control direction D_o are proportional to the sum of the errors in angle and velocity. The control voltage is calculated by multiplying the total error in axis angle and axis velocity by the aggresivity gain. Its value lies between 0 – 5 V and it is the analog input to the motor driver. V_o determines the duty cycle of the PWM signal sent to the motor. The control direction, D_o is a boolean value which is sent to Pin 4 defined in table 3.2.

The use of counter-balancing weights has further facilitated the use of servo motors by completely balancing the system when the motor is not operating. In other words, the motor only needs to provide the torque required to overcome the frictional forces in the system. The rotatory motion is accomplished by this algorithm in the following steps:

1. The system starts at zero velocity an zero axis angle and this results in maximum gain and maximum control voltage.

2. The temporary target angle is a variable within the controller loop which increases in multiples of the step size and provides a reference for the angle error. As the axis angle approaches the temporary target angle, the angle error reduces and the system slows down as the angle error is multiplied by five times its values and thus has a higher contribution to the control voltage.

3. As the velocity falls below 99 % of the target veolcity, the temporary target angle is increased by the step size. This increases the error in angle correspondingly the control voltage and the system increses in speed.

4. This process continues till the axis angle reaches the target angle.

The algorithm is also summarised by the flowchart given in Figure 3.7. The implementation of this algorithm as a Labview Virtual Instrument (VI) is given in Appendix C.

3.3 The Acquisition System

The acquisition system is the primary optical component of the sBLTI which is responsible for multispectral image acquisition. In the following sections we will

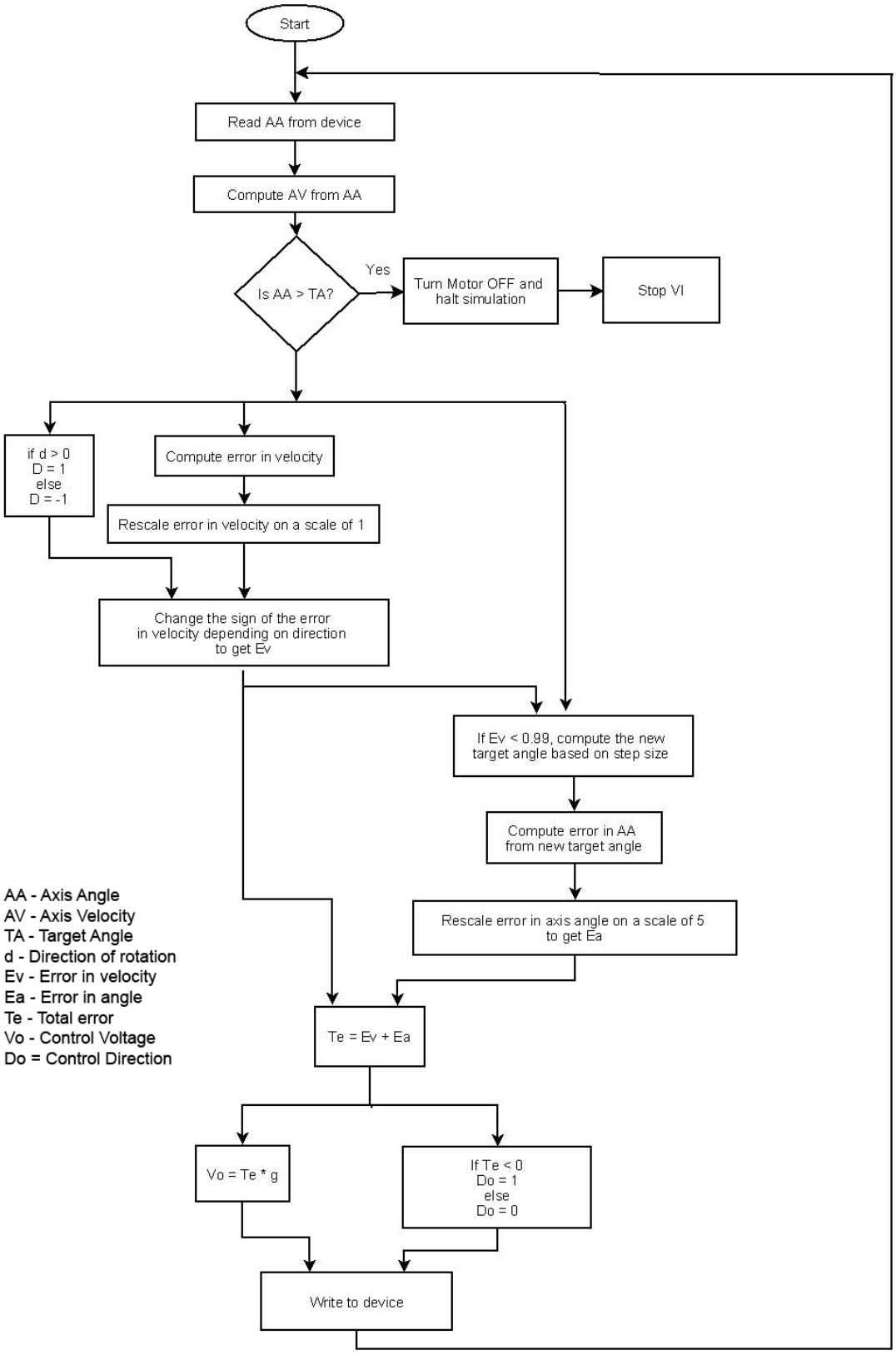

Figure 3.7: Flow chart representation of the control algorithm

look at the two components of this subsystem – the CCD camera and the filter set.

3.3.1 The CCD (charge coupled device) Camera

This system employs the Imager 3 QE CCD camera provided as a part of the Picostar Imaging System from LaVision GmBH, Germany for image acquisition. A CCD camera converts photons to electric charge based on the photoelectric effect. The CCD sensor consists of many individual CCDs that are arranged in a rectangular array. Each pixel (picture elements) has a size in the order of $10 \times 10 \mu m$. It is built on a semiconducting substrate with a p-layer (cathode) and n-layer (anode), an insulating oxide layer and metal conductors on the surface. A small voltage generates an electric field in the semiconductor. An incident photon produces an electron-hole pair in the p-n-junction and the electrons migrate towards the minimum of the electric field. Here the electrons are accumulated during the exposure time. The number of electrons correspond to the intensity of the incident light.

The pixels are arranged in an array. In order to read out the sensor the pixels have to be addressed sequentially. The electrons are shifted vertically one row at a time into a masked analog shift register on the lower edge of the sensors optically active area. Each row in the analog shift register is then clocked pixel by pixel through a charge-to-voltage converter. This converter generates a voltage for each pixel that is proportional to the detected amount of light at this sensor position.

The transmission format is either sequential (so called progressive scan) or interlaced. The progressive scan approach preserves the image integrity while the interlaced approach will read out of all odd rows before the even rows are addressed. Therefore the progressive scan approach is more useful for imaging applications.

The masked-off storage area of an interline transfer CCD reduces the fill factor of the chip i.e. the ratio of optically sensitive area and entire chip area. This is often compensated by a microlens array on the sensor that is collecting the incident light onto the sensitive areas.

3.3.1.1 Spectral Sensitivity

Like photographic film each CCD sensor has a sensitivity and spectral response. The sensitivity of a pixel is given by its quantum efficiency (QE). This

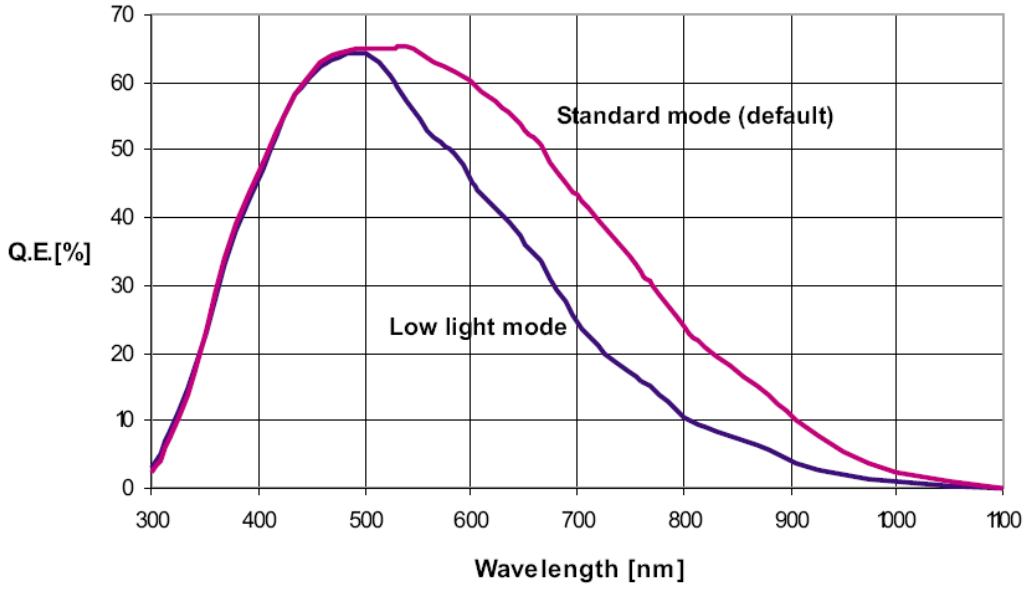

Figure 3.8: Spectral Quantum Efficiency for the Imager 3 QE.

is defined as ratio between number of collected photoelectrons and the number of incident photons per pixel. The QE depends basically on the pixel architecture, i.e. dimensions, material and thickness of the optically sensitive area. The CCD substrate material silicon has a frequency dependent band gap. Therefore photons of different frequencies will penetrate the sensor differently. As a result the quantum efficiency is wavelength dependent.

It can be seen in Figure 3.8 that the QE of this camera in the spectral band important for BLT (500 nm – 700 nm) the QE is approximately 60%.

3.3.1.2 Sources of noise

A CCD pixel is as any electric device a subject of electronic noise. The major part of noise is generated thermally. Heat can also generate electron-hole pairs in the semiconductor that can not be separated from those generated by the photoelectric effect. Thermal effects will reduce the signal-to-noise ratio. This is especially a problem for low signal intensities. The dark current noise has a value of approximately the square root of the dark current and doubles for about every 6° C increase in temperature. Therefore many CCD sensors are cooled for scientific imaging.

Specification	Value
Sensor type	CCD-Interline Progressive Scan with lens-on-chip
Number of pixels	1376 × 1040
Pixel size	$6.45\mu m \times 6.45\mu m$
Sensor format	2/3 ”
Scan area	8.9mm × 6.7mm
Cooling type	2-stage peltier cooler with forced air cooling
Maximum QE	$\geq$ 60 %
Spectral Response	200 – 1000 nm
Average dark charge	$<$ 0.1 e $^-$/pixel s

Table 3.3: Imager 3 QE Specifications

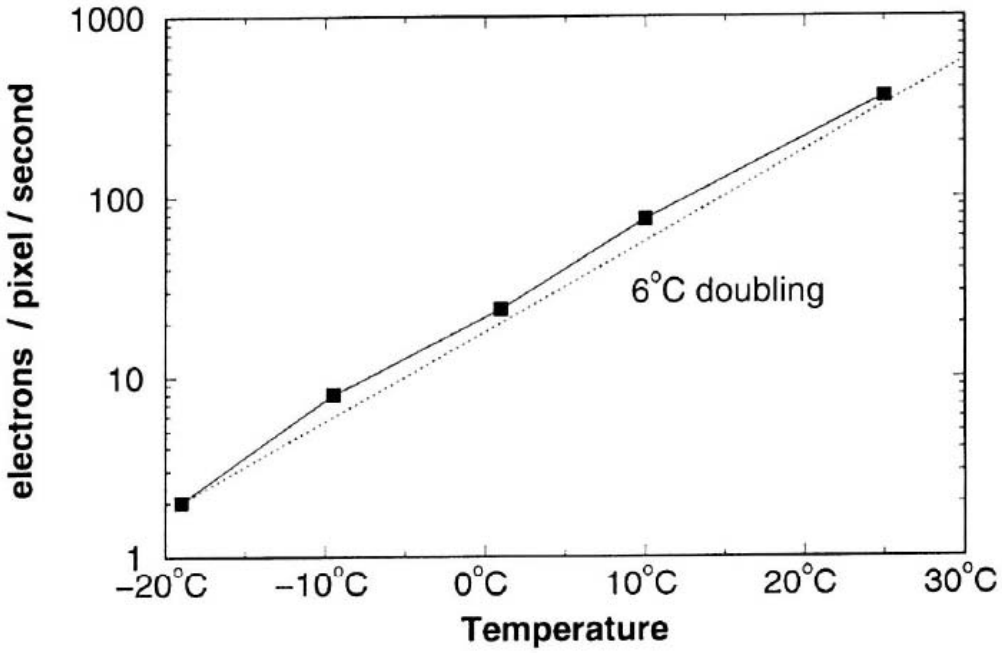

Figure 3.9: Dark current noise vs. Temperature.

Another source of noise is the read noise which is generated by the charge-tovoltage conversion during the readout procedure. The read noise increases with the readout frequency. A careful optimization of the conversion electronics, a reduced readout frequency and a cooling of the sensor will limit the read noise to a few electrons per pixel.

The specifications of the Imager 3 QE have been summarised in Table 3.3

3.3.1.3 The Lens System

Figure 3.10 shows the working distance for the sBLTI.

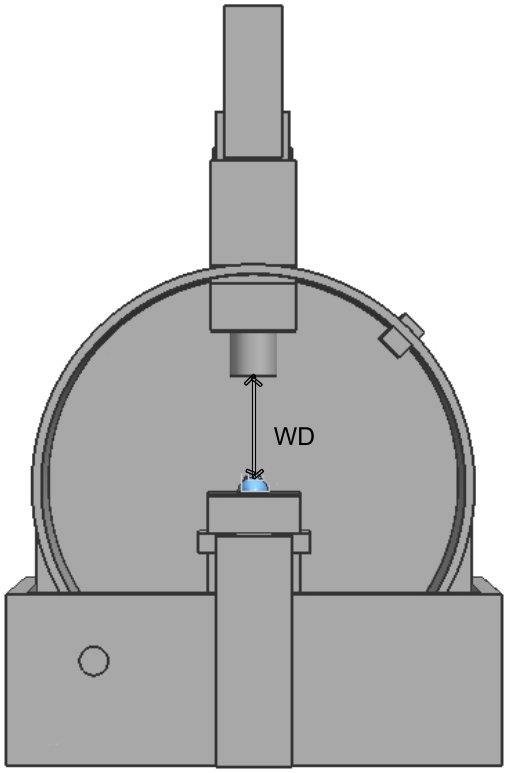

Figure 3.10: Working distance in BLTI

From the drawings in Appendix A, it can be seen that the maximum possible working distance (WD) available in this design of the sBLTI is 8" and the minimum possible WD when the CCD camera is lowered as far as possible into the mounting drum is 6". The camera system came with a 50mm Nikkor lens but this being a wide field lens was unsuitable for close-up imaging. As given in Table 3.3, the Imager 3 QE has a sensor format of 2/3".

Field of View = 5"
Sensor Resolution = 1376
Thus, Minimum feature size = $\frac{5}{1376}$ = 0.003633 " = 0.0911 mm
Given, Pixel size = 6.45 $\times 10^{-3}$ = 0.00645 mm
Therefore, Magnification, m = $\frac{Pixel\,size}{Minimum\,feature\,size}$ = 0.0707

Now, Focal length, f = WD / (1 + 1/m)

For maximum WD = 8 ” = 203.2 mm; f = 13.4 mm

For minimum WD = 6 ” = 154.2 mm; f = 10.069 mm

For our system we are using the HF12.5HA-1B lens from Fujinon. The specification of this lens are given in Table 3.4

Specification	Value
Focal Length	12.5 mm
Field of View	$38°47' \times 29°35'$
Iris range	F1.4 $\sim$ F16
Minimum focussing distance	10 cm
Back focal length	15.09 mm
Mount	C

Table 3.4: Specifications of HF12.5HA-1B

3.3.2 The Filter Set

As discussed in Section 2.1.2, the firefly luciferase is the most commonly used bioluminescence reporter. The spectra of the Firefly Luciferase is shown in Figure 3.11.

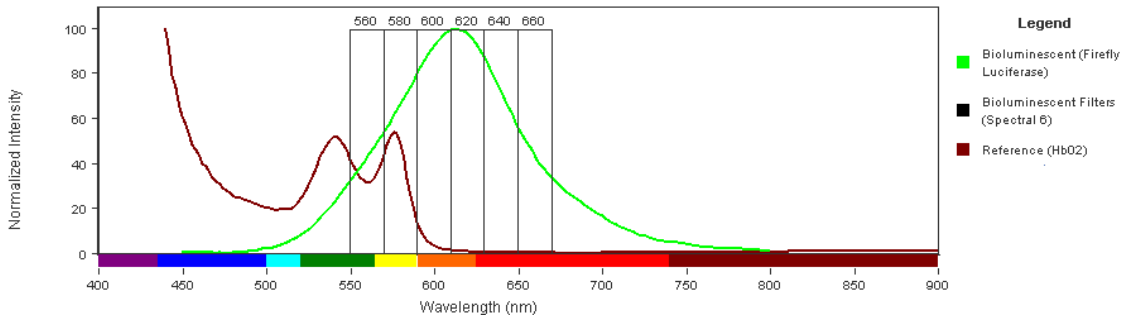

Figure 3.11: The spectrum of the Firefly Luciferase Expression. The six spectral bands that are used in our system have been demarcated.

Acquiring images at a high spectral resolution is one of the objectives guiding the design of this tomographic imager for bioluminescence signals. Two filter sets were considered to this end – VariSpec Liquid Crystal Tunable filters (LCTF) from

CRi Inc. USA and Interference filters from Omega Optical Inc. USA. The spectral bands being considered in this system are 560 ± 10, 580 ± 10, 600 ± 10, 620 ± 10, 640 ± 10 and 660 ± 10.

The optical density (OD) is defined as the degree of opacity of a translucent medium expressed by $log\frac{I_o}{I}$, where I_o is the intensity of the incident ray, and I is the intensity of the transmitted ray. OD is also related to the amount of energy transmitted through a filter. A higher OD indicates lower transmission. Transmission can be calculated using the following equation:

$$T = 10^{-OD} \times 100 = \%transmission \tag{3.2}$$

Interference filters are multilayer thin-film devices. They can be designed to function as an edge filter or bandpass filter. In either case, wavelength selection is based on the property of destructive light interference. Incident light is passed through two coated reflecting surfaces. The distance between the reflective coatings determines which wavelengths destructively interfere and which wavelengths are in phase and will ultimately pass through the coatings. If the reflected beams are in phase, the light is passed through two reflective surfaces. If, on the other hand, the multiple reflections are not in phase, destructive interference reduces the transmission of these wavelengths through the device to near zero. This principle strongly attenuates the transmitted intensity of light at wavelengths that are higher or lower than the wavelength of interest. These filters require a C-mount adapter available from Edmund Optics, USA. Moreover, while making spectral measurements, these filters need to to be manually mounted and unmounted from the CCD camera.

CRi's LCTF are tunable birefringent filters. the filters function like high quality interference filters, but the wavelengths they transmit are electronically tunable and allow for the rapid vibrationless selection of any wavelength in the visible (VIS) and NIR regions that the filters have been constructed to operate in. Figure 3.12 shows the transmission values over the VIS and NIR spectrum for a typical VariSpec filter.

As can be seen, the transmission in the spectral band being considered in this system is approximately 38 %. Owing to the weak nature of the bioluminescence

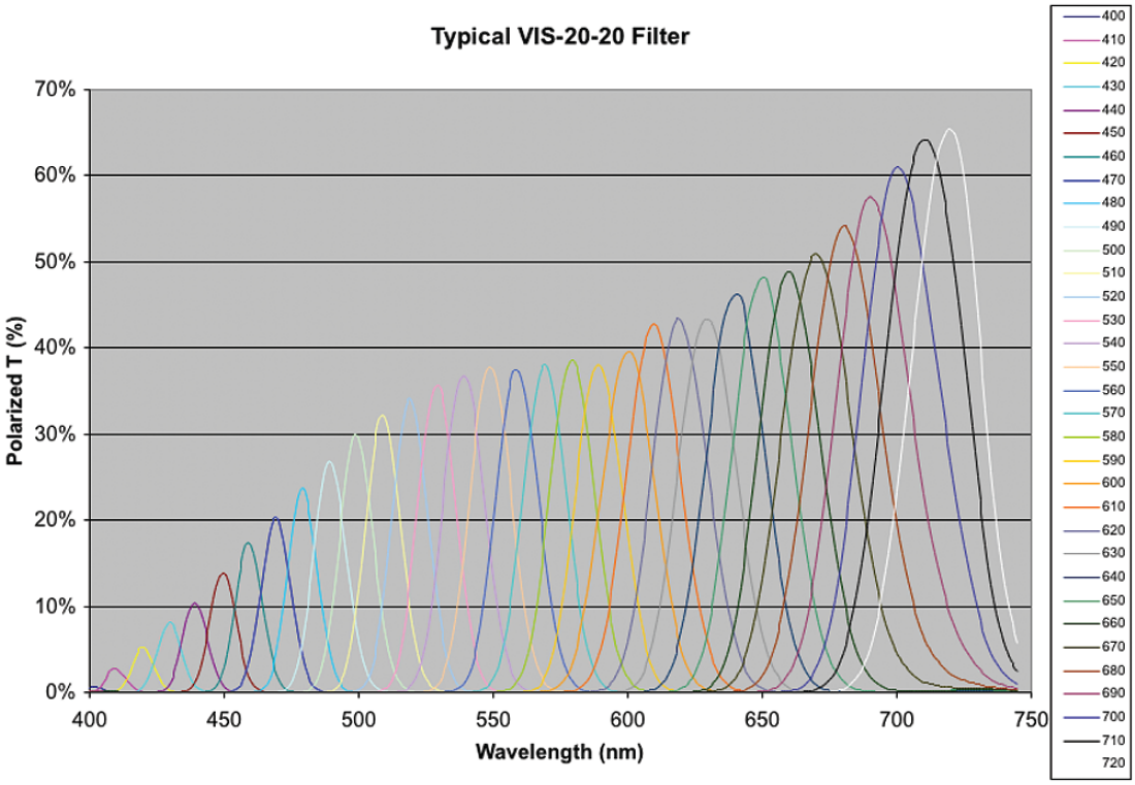

Figure 3.12: Transmission plot for the VariSpec LCTF

signals, the use of filters with low transmission would further deteriorate the quality of acquisition. For this reason the interference filters were selected. All the intereference filters used in the acquisition system have an average attenuation OD of 6 and peak transmission of 65 %.

3.4 The Stereo System

The stereo subsystem is the method employed in this tomographic imager to extract the surface information of the animal model. The application of extracting the surface map lies in improving the accuracy of the boundary measurements which are used in the inverse source problem. Further they can also be used in the co-registration of the optical domain measurements with 3D measurements made using other modalities like CT [22] and MRI [21].

This subsystem comprises of a stereoscopic camera system and an illuminator. The stereoscopic camera system is a two-camera system Bumblebee from Pointgrey

Research, Canada and the illuminator is a white ring light from Stockeryale, Ireland.

3.4.1 Stereo Vision

3D surface extraction can be understood as measuring the depth of the scene finding corresponding points in two different views of the same scene. Simple triangulation can then be used to determine the distance.

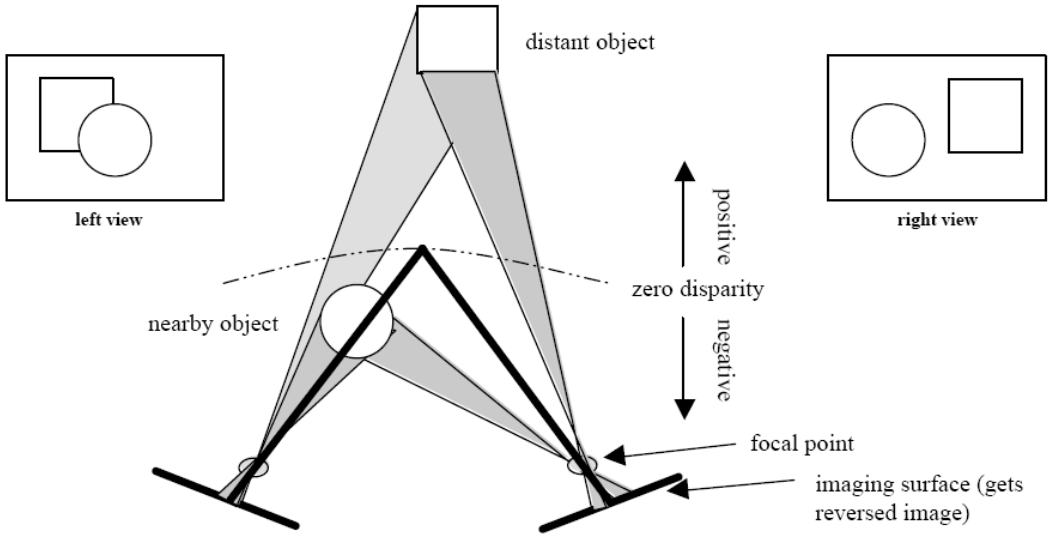

Figure 3.13: Geometry of stereo vision

Figure 3.13 depicts a typical camera configuration, with the cameras pointing somewhat inwards. Suppose the coordinates of two corresponding points are (x_{left}, y_{left}) and (x_{right}, y_{right}). For cameras that are properly aligned, $y_{left} = y_{right}$. The disparity is defined to be $x_{right} - x_{left}$. This value can be positive or negative, depending on the angle of the cameras as well as the distance to the object. Searching for corresponding points is a recurring problem in machine vision as well as in image and video compression. Computing stereo disparity is very similar to finding optimal motion vectors, and approaches for both problems are similar.

The most common approach in both stereo disparity calculations and motion compensation is to slide a block taken from one image over a second image. This approach is known as the Block Matching Algorithm. At each possible offset, a square-sense error is computed. Finding the position where the subimages are most similar (and the minimum error occurs) is equivalent to computing the disparity.

Disparities typically have a small dynamic range (often < 10 pixels) compared to the actual distances to objects. Therefore, measuring disparities to integral pixel values results in very low depth resolution. The solution is to measure disparities to subpixel resolution, with half-pixel accuracy being common and quarterpel used in some systems.

Finding corresponding points for every pixel in an image is an extremely computationally expensive task. Consider a straightforward implementation: for every pixel in the left image, a surrounding block of pixels (often 16×16 or 32×32) is slid across a row from the right image (which is the same height as the block from the left, but the width of the whole image.) At each position, the square-sense error (or other error metric) is computed, involving a large number of additions and multiplications. Rather than searching an entire row, a subset of it is usually selected based on an estimate of the maximum disparity likely to be seen in the data. The search range can also be dynamically adjusted by exploiting the fact that nearby points are likely to have similar disparities.

3.4.2 The Bumblebee System

The Bumblebee Stereo Vision System consists of a two-camera module and a software system that performs range measurements. The camera module generates two gray-scale, or color, images that are digitized and stored in the memory of the computer. The software system analyzes the images and establishes correspondence between pixels in each image. Based on the cameras geometry and the correspondences between pixels in the images, it is possible to determine the distance to points in the scene. The Triclops SDK is the development package provided along with the system which can be used to build a stand alone application using the camera module.

Figure 3.14 shows the interface of the stereo interface based provided alongwith the SDK.

The Triclops library establishes correspondence between images using the Sum of Absolute Differences correlation method. The intuition behind the approach is to do the following:

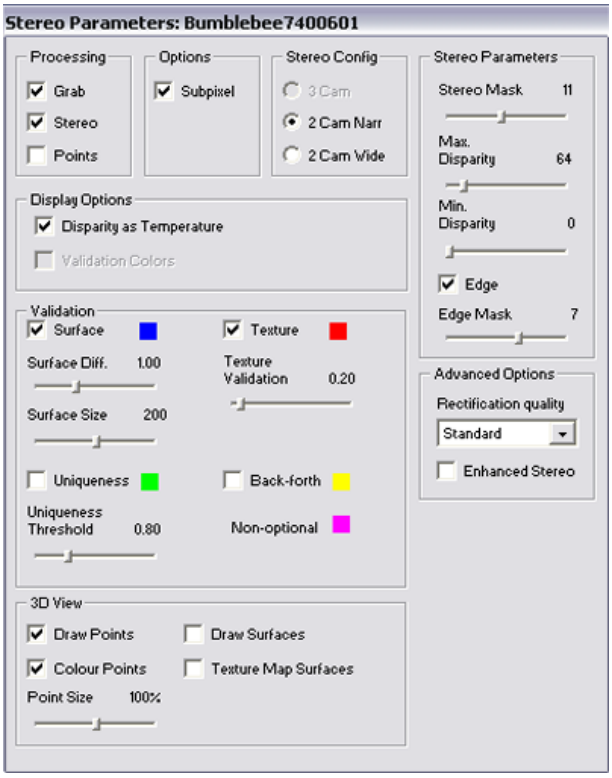

Figure 3.14: The Bumblebee stereo interface

1. For every pixel in the image.
2. Select a neighborhood of a given square size from the reference image.
3. Compare this neighborhood to a number of neighborhoods in the other image (along the same row)
4. Select the best match.

Comparison of neighborhoods or masks is done using the following formula:

$$\min_{d=d_{min}}^{d_{max}} = \Sigma_{i=-\frac{m}{2}}^{i=\frac{m}{2}} \Sigma_{j=-\frac{m}{2}}^{j=\frac{m}{2}} |I_{right}[x+i][y+j] - I_{left}[x+d+i][y+j]| \tag{3.3}$$

where, d_{max} and d_{min} are the maximum and minimum values of disparity
m is the mask size
All these values can be controlled through the interface in Figure 3.14.

Edge detection is an optional feature that allows matching on the changes in the brightness rather than the absolute values of the pixels in the images. This feature is useful because the cameras in the Triclops camera module have auto gain control. If the auto gains in the cameras do not change identically, the absolute brightness between images may not be the same. While absolute brightness are not the same, the change in the intensity stays constant. Therefore, using edge detection will help in environments where the lighting conditions change significantly.

There are a number of parameters that determine the kind of depth image produced:

- Disparity Range – Disparity range is the range of pixels that the stereo algorithm searches in order to find the best match.
- Correlation Mask – Correlation mask is a square neighborhood around the pixel that the system is trying to find the match for. The user is allowed to specify the size of the correlation mask.
- Two validation methods maybe used to avoid incorrect measurements – Texture validation and Uniqueness validation.
- Subpixel Interpolation – The Triclops library allows matching between images to subpixel accuracy.
- Surface Validation – This is a filtering process designed to remove noise from the disparity image.

The availability of all these variables for controlling the quality of range measurements / surface map, makes the Bumblebee system particularly robust and suitable for use in a controlled environment of the sBLTI.

CHAPTER 4
Platform Calibration

While the previous chapter discussed the likely causes of noise introduced in the system due to individual components, this chapter characterises and calibrates the system. The focus will be on two forms of error – error due to mechanical bias and the limitations introduced by the noise in the optical components.

4.1 Mechanical Error

The fabrication of the individual mechanical components of this system was done at the machine shop at RPI. All the components shown in Appendix A had to be built from raw material and even with the use of most accurate machines, a certain amount of mechanical bias appears in the assembly. The purpose of this section is to analyse two features of the rotatary component of the design. The only rotating component in this design is the mounting drum. This component has to be rolled from a flat piece of aluminium. This process in no way ensures a perfect circular drum and the first experiment is to measure the ellipticity of the system. The second experiment looks at the dynamics of the system as the accuracy of the control module is tested. As mentioned in the previous chapter, the units of operation in the control system are the encoder pulses. The first step is to calibrate the system and test the accuracy of position control for varying values of angular resolution.

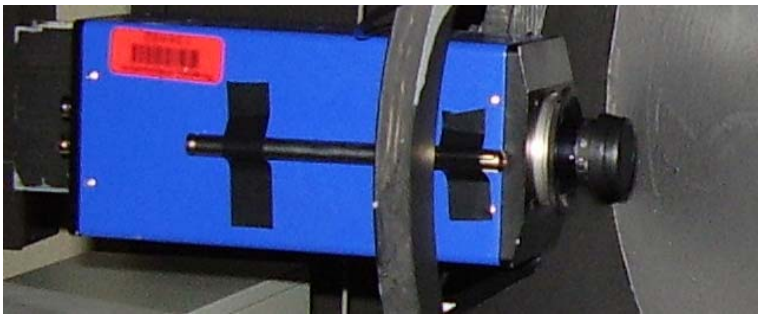

Figure 4.1: Approximation of the optical axis of the camera

4.1.1 Ellipticity

The experimental setup uses a laser pointer as a measure of the position of the optical axis of the camera. This is done as shown in Figure 4.1. The camera was then rotated between 15° and 135° in 15° steps and the position of the laser pointer was marked. In the next step the axis of rotation of the drum was marked and was taken as reference. The deviation of the pointer from the reference for each angle was calculated. The results are tabulated below.

Angle (°)	Deviation (mm)
15	17
30	7
45	2
60	-2
75	-6
90	-11
105	-16
120	-23
135	-35

Table 4.1: Deviation measurements for ellipticity measurements

One of the most significant observation is the deviation of the normal (90°) view from the reference axis. The readings were normalised by shifting the reference axis to the position marked by the normal view. The polar plots for both normalised and un-normalised readings are given in Figure 4.2.

4.1.2 Angular Position Accuracy

The experiment for measuring the angular accuracy of the system is done using a similar set up. A protractor is placed on the stage with its axis in line with the axis of rotation. The lateral position of the protractor is adjusted by inspection so as to align it with the view from the normal position. Once the position is set, the stage was not disturbed. Figure 4.3 shows the setup for this experiment.

The first step of the experiment was the calibration of the system. After performing multiple iterations of rotation with the different target angles, it was confirmed that 5 encoder pulses moves the system by 1.35°. Following this step, the experiment was carried out in the following steps. The system was rotated from 0°

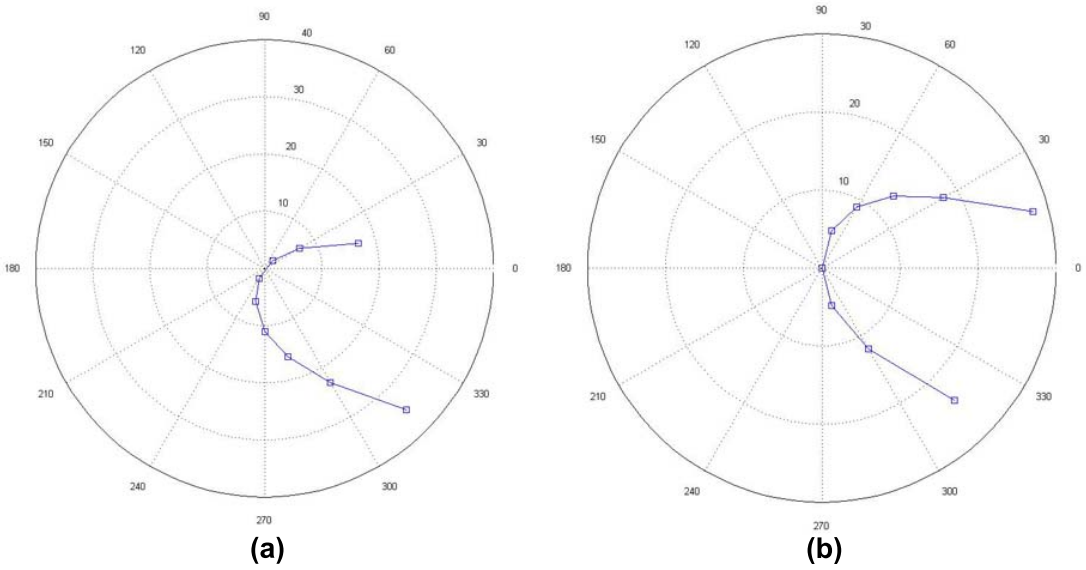

Figure 4.2: Polar plot quantising the ellipticity of the system: (a) Un-normalised (b) Normalised.

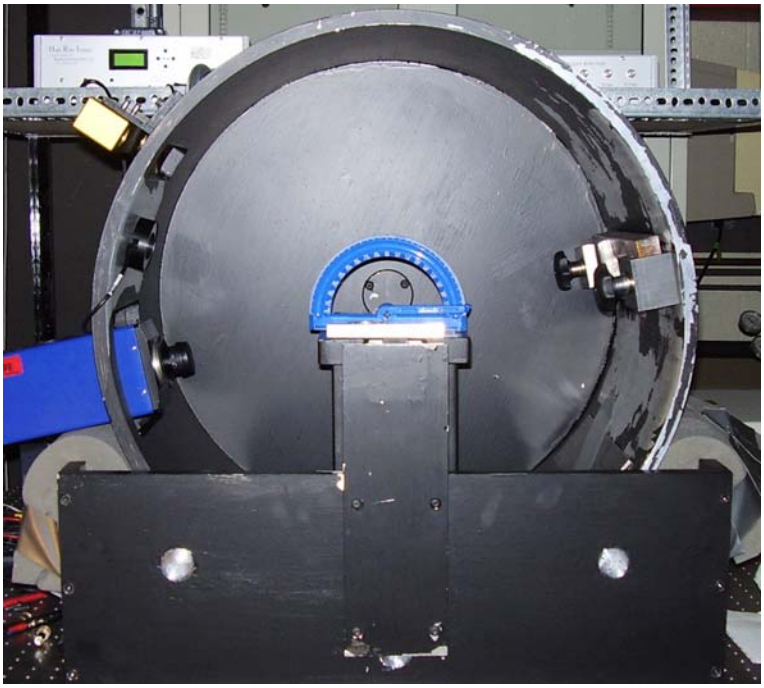

Figure 4.3: Experiment setup for measuring the angular accuracy of the control system

to 135° in steps of 5°, 10°, 15°, 20°, 30° and 45° and the angles at which the system stopped was recorded by reading the laser pointer position on the protractor. The difference in every adjacent angular position was matched against the angle that it was suppose to move. The error in the values for selected angles are plotted in Figure 4.4 and the values of maximum errors in position for each step size are tabulated below,

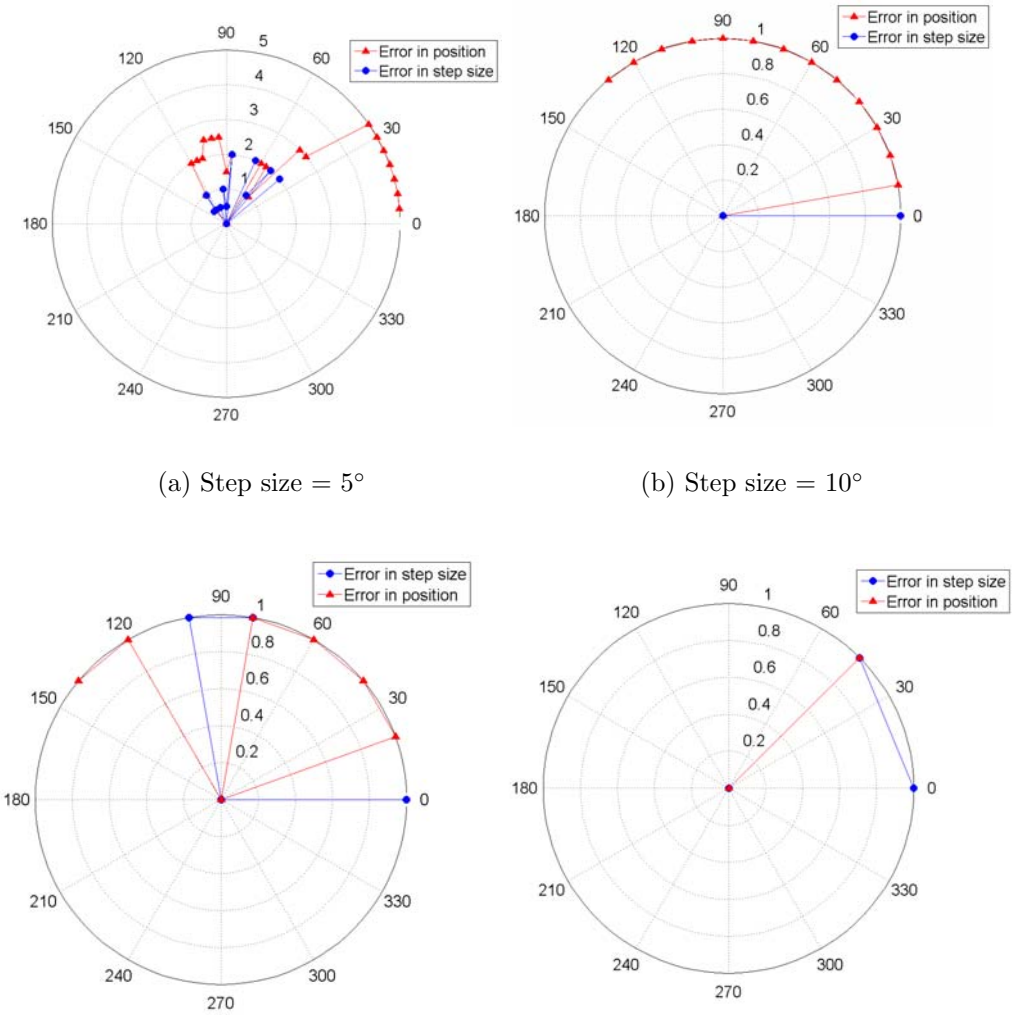

(a) Step size = 5°

(b) Step size = 10°

(c) Step size = 20°

(d) Step size = 45°

Figure 4.4: Polar plots showing the positioning errors varying with angles for selected step sizes.

The values of maximum errors in position for each step size are given in table

4.2. It can be seen from Figure 4.4 that the errors reduce with increaing step size and the lowest angular resolution that may be proposed after this experiment is 10°.

Step Size (°)	Encoder Pulses	Maximum Error (°)
5	18.5	2
10	37	-1
15	56	1.5
20	74	2
30	111	-3
45	166.67	1

Table 4.2: Maximum angular positioning errors

4.2 Noise Characteristics

As discussed in Section 3.3.1 the CCD camera has inherent error due to electronic noise. The noise was attributed to electrons generated due to heat developed in the electronic circuit during operation. Figure 3.9 shows the variation of the dark current with temperature. The other form of noise is the read out error which is largely dependent on the frequency at which the charge from the sensor is converted to voltage. This noise remains more or less constant over time. The other component of the acquisition sub-system, namely the filter set also affects the signal-to-noise ratio. In this section the effect of the noise characteristics of the acquisition system on the measurements is discussed.

4.2.1 Characterising drift

Baseline noise is the short time variation of the baseline from a straight line caused by electric signal fluctuations, temperature fluctuations and other factors. For the noise to be characterised as a short-time charateristic in time-dependent system, a requirement is that the baseline should deviate as little as possible from a horizontal line. The deviation of the baseline from the horizontal is referred to as drift. The concept of drift can be better explained by Figure 4.5.

In short drift is the variation of noise with time. It is usually attributed to warm up time of the camera system but is a critical factor for the imaging protocol to

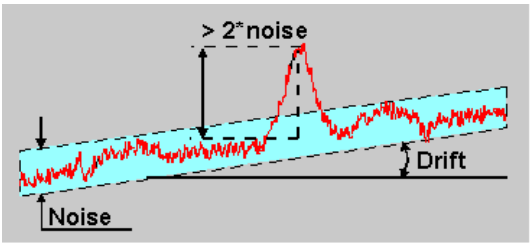

Figure 4.5: Defining Drift and Noise

ensure that the assumption of uniform noise level all acquired image levels holds true. The experiment involved taking dark images on the camera, at an interval of ninety seconds for one and a half hours. The average photon counts in those images gave a quantitative value of dark noise at the instant of acquisition. The average values thus calculated were plotted on a time scale to characterise the change in detector noise with time. Figure 4.6 shows the drift in detector noise. The stabilised values of the dark was calclated to be 41.69 counts with a standard deviation of 0.201.

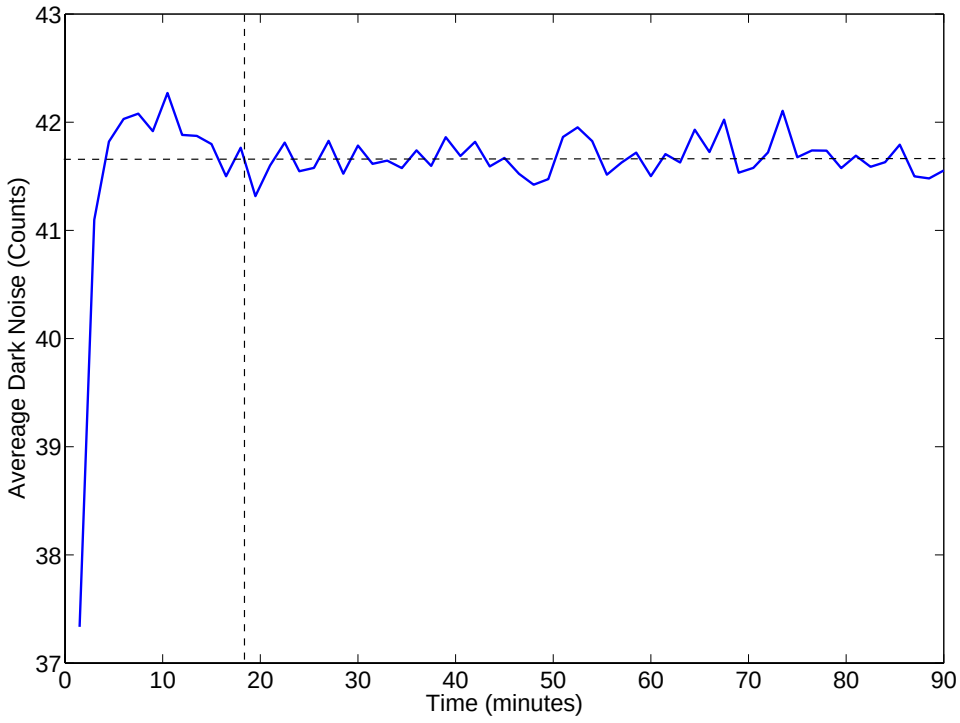

Figure 4.6: Variation of noise with time. The noise stabilises after 18 min to a value of 41.69 counts

4.2.2 Spectral Characterisation

As stated earlier, this system has been spectrally designed to image the luciferase expression. However for the initial phantom studies the tests will be done on a substitute for Luciferase. An orange LED (Catalog No. 276–272, Radioshack) has been demonstrated as a suitable replacement for Luciferase [28]. First we will compare the spectra of the LED with the known spectra of Luciferase using USB2000 spectrophotometer from ocean optics. Figure 4.7 shows a comparison between the two spectra.

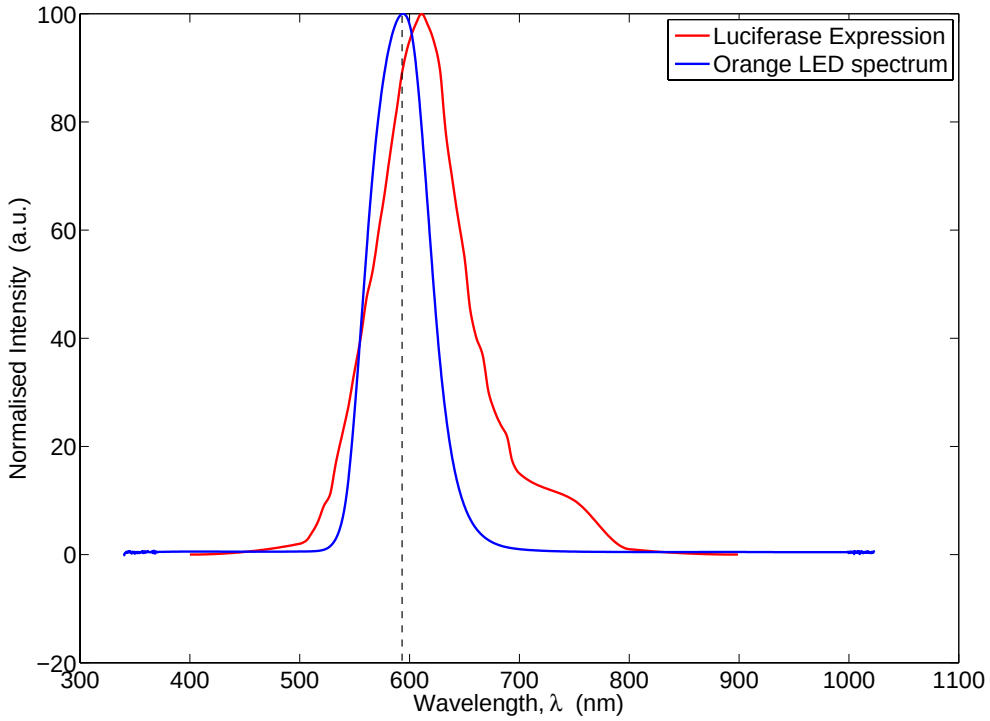

Figure 4.7: Spectral comparison of Luciferase expression and Artificial source.

Figure 4.7 shows that the spectra of the LED is very close to that of Luciferase with close spectral peaks. The FWHM of the two spectra may differ slightly, but it is not a large enough difference that would result that would cause the phantom studies to fail.

Second, the interference filters were characterised as having a transmission of 65 % at peak. This data was corroborated by acquiring the transmission spectra

through the six interference filters. The resulting spectra are shown in Figure 4.8.

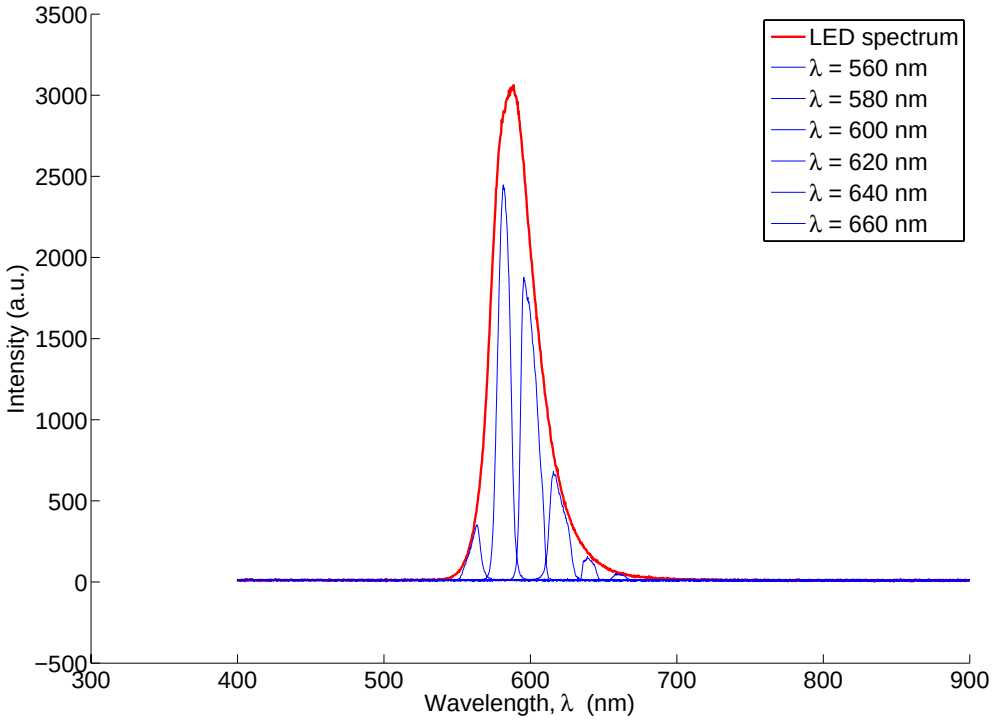

Figure 4.8: Filtered spectra of the LED through the six spectral bands of the acquisition system

It can be seen from this figure that the filters do not have a 100 % transmission. While the transmission values are not characterised for each individual filter at this point it is important to note the relevance of higher transmission values in a bioluminescence imaging system as the reduction in signal strength affects the SNR as much as an increase in the noise signal.

CHAPTER 5
System Evaluation

The previous chapter discussed the contribution of the mechanical and optical bias inherent in the design of this imaging platform, to the signal-to-noise raio (SNR) of the acquisition. In this section the sensitivity of the platform is studied by varying parameters such as tissue absorption coefficient, scattering coefficient and bioluminescence source location. Owing to the multiview capability of the platform, the source location is characterised by the depth of the source. In the following sections the construction of the phantom is discussed and subsequently the results are discussed.

5.1 Liquid Phantom Design

The propagation of light in tissues is accurately described by the Radiation Transport (RT) theory and further analysis is approximated by the diffusion equation. The fundamentals of the RT theory have been discussed in Appendix D. In this study a liquid phantom was used to study the sensitivity of the system to biolumimnescence signals as a function of depth of the source in the tissue.
As reported in [28] the optical properties of the major tissues in mice are as follows,

	Highly transmitting		Moderately transmitting	Poorly transmitting	
	Heart	Breast	Muscle	Lung	Liver
$\mu_a\,(mm^{-1})$	0.11	0.004	0.23	0.35	0.45
$\mu_s'\,(mm^{-1})$	1.10	0.8	1.00	2.30	2.00

Table 5.1: Optical properties of major organs in mouse.

Three liquid phantoms made of milk, ink and water were constructed to mimic the optical properties of breast, heart and muscle tissue (each representing one category of tissues in Table 5.1). The bioluminescence source was simulated using an orange

LED (Catalog No. 276–272, Radioshack). The spectral properties of the source were discussed in section 4.2.2. The peak of the emission spectra was found to be at 590 nm which made it a worthy substitute for firefly luciferase. The light from the LED was delivered to the phantom through an optical fiber (P400-025-SR, Ocean Optics, USA) having a core diameter of 400 μm and was measured to be 100 nW. The variation in depth for this source was achieved using the arrangement shown in figure 5.1. The depth of the source was changed using a manual motion stage (Part number – 423, Newport Co.,USA) with a micrometer actuator (SM–25, Newport Co., USA).

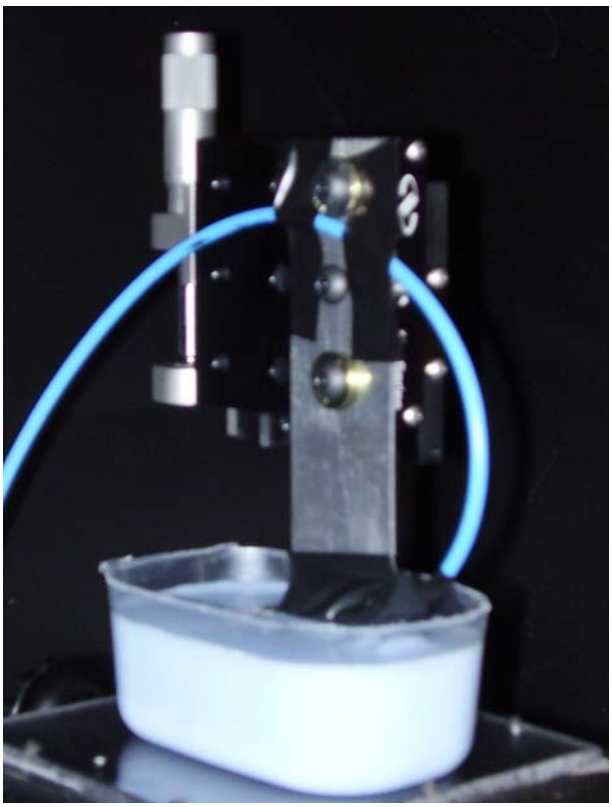

Figure 5.1: Experimental setup for measuring the sensitivity of the sBLTI

The source was placed 2 mm below the surface at the start of the experiment and was moved down till the maximum detected photon count is within the standard deviation of the dark noise of the CCD camera. This process was repeated for three spectral bands (580 ± 10 nm, 600 ± 10 nm and 620 ± 10 nm) and for the three types of phantoms.

5.1.1 Scattering Component of the Liquid Phantom

Several researchers in the field of tissue optics have used milk as a scattering component in liquid phantom [33]. In recent years however a more popular choice for scattering agent has been Intralipid^{TM}. The optical properties of Intralipid^{TM} which is close to the properties of homogenised milk in the NIR region have been studied extensively in [34], where electron microscopy was used to study the size of particles and Mie theory was used to calculate the optical properties. It was found that the dependence of the scattering coefficient (μ_s) on wavelength (λ) is given by equation 5.1.

$$\mu_s(\lambda) = 0.016\lambda^{-2.4} \pm 6\% \tag{5.1}$$

and the anisotropy factor g was given by equation 5.2,

$$g(\lambda) = 1.1 - 0.58\lambda \pm 5\% \tag{5.2}$$

for $0.4 < \lambda < 1.1$, where λ is in μm, and μ_s' is in mm^{-1}. Using the formula, $\mu_s' = \mu_s(1-g)$, the variation in the isotropic scattering coefficient was calculated for the above mentioned range.

Figure 5.2 shows the graph of μ_s' plotted over the range of 400 nm to 1100 nm, for 1ml of the Intralipid^{TM} 10 % diluted in 999 ml of water. For this experiment we make the assumption that the optical properties of homogenised milk is approximately equal to the scattering properties of Intralipid 10 % within permisible error. As can be seen from the above graph, the value of μ_s' at 590 nm was found to be 0.0137 mm^{-1} at a concentration of 1 part milk in 999 parts water. The value of μ_s is directly proportional to the concentration of milk required to impart the scattering component of the phantoms and thus for the three μ_s' values being considered - $0.8\,mm^{-1}$, $1.0\,mm^{-1}$ and $2.3\,mm^{-1}$, the required volume of milk was calculated to be 12.3 ml, 16.8 ml and 33 ml respectively, with the rest being water.

The background absorption of milk is close to that of water. It is known that the absorption coefficient of water at 590 nm is approximately 0.0018 mm^{-1} which is well below the μ_a of any tissue we are considering in table 5.1. Extra absorbing

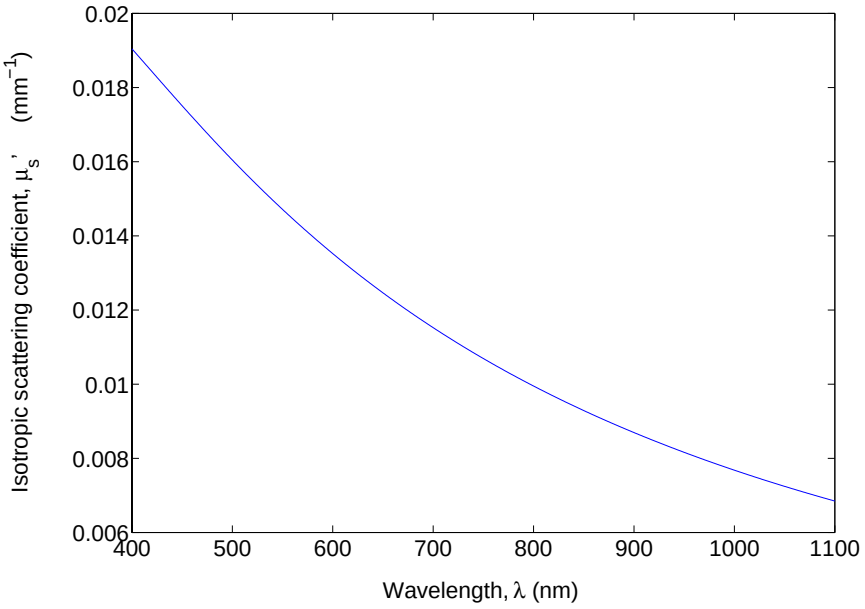

Figure 5.2: Graph of μ_s' for 10 % Intralipid diluted to 0.01 %

agent must therefore be added to the phantom to make its optical properties closer to that of the tissue.

5.1.2 Absorbing Component of the Liquid Phantom

Blue ink was used in this study to control absorption in the phantom. It was assumed that the scattering coefficient of the phantom mixture is independent of the amount of ink added. However this would only be true if the total volume of diluted dye added to the phantom was small compared to the total volume of the phantom which was calculated to be 210 ml. The optical properties of the ink were not provided by the manufacturer and thus absorption properties of the ink were measured in our lab. This process has been explained in detail in Appendix E. The absorption spectrum of the ink as found by this process is shown in Figure 5.3.

The absorption coefficient of the ink is related to its concentration by the equation,

$$\mu_a = \epsilon \times c \tag{5.3}$$

where, ϵ is called the extinction coefficient and c is the concentration of ink. If v is the volume of the ink to be used and the total volume of the phantom is V_p ml,

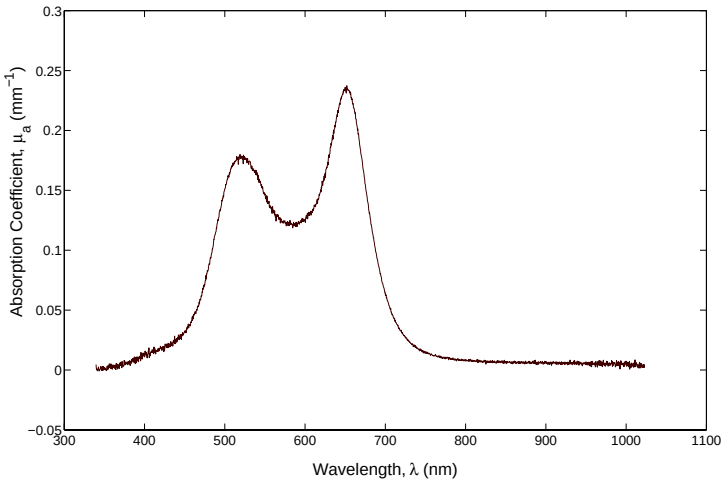

Figure 5.3: Graph of μ_a' for 100 μl of 5 % solution of ink in 4 ml water.

then c is given by,

$$c = \frac{v}{V_p + v} = \frac{\mu_a}{\epsilon} \tag{5.4}$$

Thus the value of absorption coefficient, μ_a can be related to the volume of ink to be used by the relation,

$$v = \frac{V_p \times \mu_a}{\epsilon - \mu_a} \tag{5.5}$$

The value of ϵ for the 5 % stock solution of the ink was found to be $12.2686\, mm^{-1}$ and V_p was 210 ml. Using these values, the volume of ink solution to be added to the phantom were calculated.

5.1.3 Refractive Index of the Liquid Phantom

The refractive index of a milk-based liquid phantom will be approximately that of water, which is 1.33 - slightly less than that of tissue (1.4). However the differences in the refractive index can be taken into account while solving the inverse source problem.

The composition of the liquid phantom for each of the tissues being considered is given in Table 5.2.

	Milk (ml)	5 % ink solution (ml)	Water (ml)
Breast	12.3	0.0685	197.7
Muscle	16.8	4.0	189.2
Lung	33	6.1	170.9

Table 5.2: Volume composition of the liquid phantoms.

5.2 SNR Characteristics

As mentioned previously, in this experiment the source was placed at a depth of 2 mm in the liquid phantom and displaced vertically downwards till the signal was undiscernible in the images obtained. Figure 5.4 shows the range of variation in signal strength captured. As can be seen in this figure, there is considerable poisson noise in the images and this noise can potentially skew the measurements obtained from this data. This noise was removed by the use of Anscombe filter. The Anscombe transform is a mathematical operation that transforms a Poissonian real random variable into a Gaussian random variable. It is usually used to pre-process the data in order to have the noise of constant standard deviation so as to apply denoising algorithms in the extensively studied framework of Gaussian additive noise.

Figure 5.4: Variation in signal strength from a depth of 2 mm to 20 mm in the breast tissue phantom.

As the source which is used to simulate luciferase expression in the animal model is an optical fiber, the emitted light is inherently anisotropic with directivity decided by the numerical aperture of the fiber. However, based upon the RT theory explained in Appendix D, we shall asume that this source can be assumed to be a point source at a distance of unit scattering length from the tip of the fiber where the diffusion of light will be isotropic in nature. This assumption is justified in Figure 5.4. Moreover the measurements made from this data obtained will take

the maximum value of photon count in the region shown to be the bioluminescence signal strength.

5.2.1 Calculating the detection limit

As was discussed in Section 4.2, the CCD camera has inherent dark noise which has a mean value of 41.69 counts and a standard deviation of 0.201. The average value of dark noise was taken as the noise floor when calculating the maximum depth at which the signal source is detectable, as beyond this distance the measured signal is almost entirely noise.

The signal strength was measured for the three spectral bands and in Figure 5.2.1, the variation in signal strength is plotted for each of the spectral bands in the three tissue phantoms.

As can be seen in this figure, the maximum depth at which a bioluminescence source of signal strength 100 nW can be detected is 1.5 cm in a highly transmitting tissue (breast) and 0.6 cm in a poorly transmitting tissue (lung). Beyond these depths the signal is visibly lost within the noise. It is also to be noted that, the signal strength shows the effect of the variation in optical properties over wavelength. The levels of the signals show a combined effect of absorption and scattering and hence the signal in the 620 nm spectral band is more attenuated than the other singals while the signal in the 600 nm band is the strongest of the three. With the use of filter with higher spectral resolution the variation in the source spectrum can be used to provide useful information about the optical properties of the tissues through which the light has travelled to the surface. In this study the maximum depth of detection was selected such that the weakest signal (in the 620 nm spectral band) may be detected.

5.2.2 Validation of results based on the diffusion equation

Owing to the continous wave nature of the source of bioluminescence signal, the behaviour of the signal in the tissue can be given by the steady-state solution of the diffusion equation as given in Equation D.19. Rewriting the equation as,

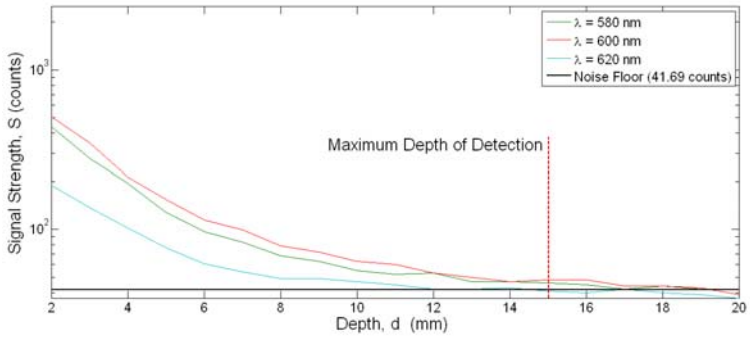

(a)

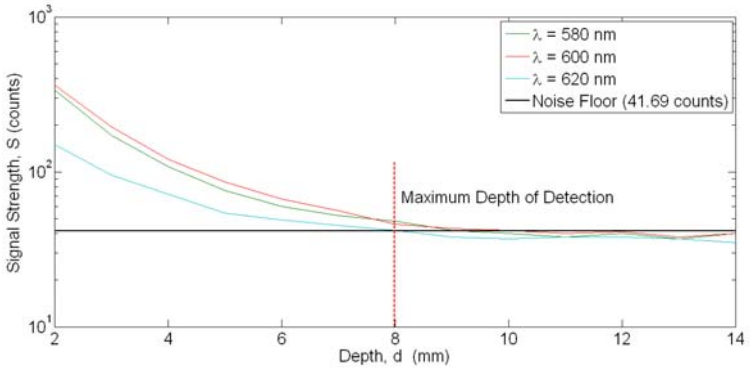

(b)

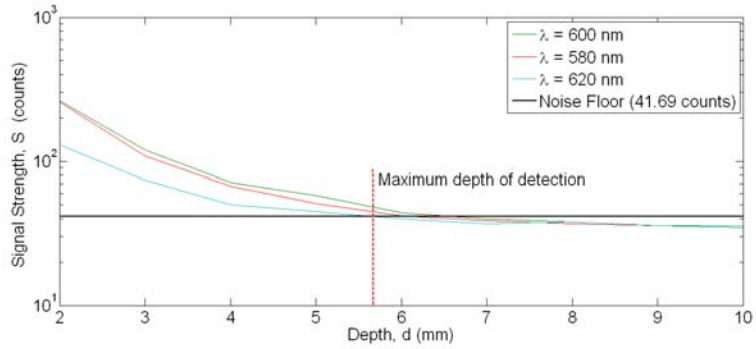

(c)

Figure 5.5: Variation in signal strength with depth : (a) breast tissue phantom, (b) muscle tissue phantom and (c) lung tissue phantom.

$$\frac{\Phi_d(d)}{h\nu c_m} = \frac{N\kappa_d^2}{4\pi}\frac{exp[-\kappa_d d]}{d}. \tag{5.6}$$

where, N is the number of photons injected by the point source into the medium to maintain a steady state, d is the depth of source, ϕ_d is the signal strength at detector and

$$\frac{1}{\kappa_d} = \sqrt{\frac{D}{\mu_a c_m}} \tag{5.7}$$

Here D is the diffusion coefficient given by

$$D = \frac{c_m}{3(\mu_a + \mu_s')}. \tag{5.8}$$

and in a scattering-dominant medium ($\mu_s' \gg \mu_a$), D can be written as,

$$D = \frac{c_m}{3\mu_s'}. \tag{5.9}$$

Substituting these values of D and κ into Equation 5.7 we get,

$$\frac{\Phi_d(d)}{h\nu c_m} = \frac{3N\,\mu_a\,\mu_s'}{4\pi}\frac{exp[-\sqrt{3\,\mu_a\,\mu_s'}\,d]}{d}. \tag{5.10}$$

Let

$$P = h\nu c_m\,\frac{3N\,\mu_a\,\mu_s'}{4\pi}$$

and

$$\mu_{eff} = \sqrt{3\,\mu_a\,\mu_s'} \tag{5.11}$$

and we can write Equation 5.10 as,

$$\Phi_d(d) = P\frac{exp[-\mu_{eff}\,d]}{d} \tag{5.12}$$

Taking natural log of both sides of Equation 5.12, we get

$$\log\left(d\,\Phi_d(d)\right) = -\mu_{eff}\,d + \log P \tag{5.13}$$

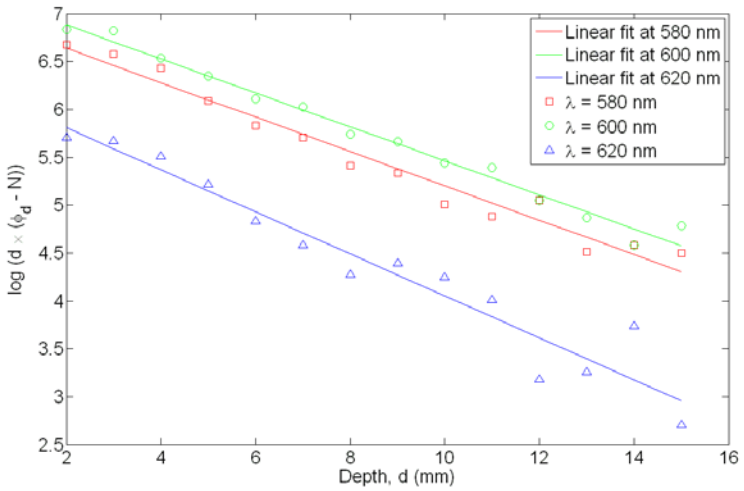

(a) Breast tissue phantom

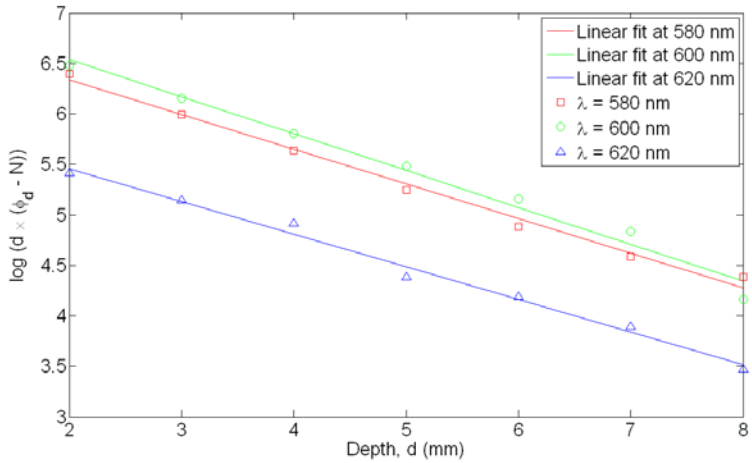

(b) Muscle tissue phantom

Figure 5.6: Variation in signal strength with depth

Two methods were adopted validate of the measurements made using the sBLTI. First, variation in signal strength with depth was checked for the linear behaviour according to Equation 5.13. Second, as can be seen from Equation 5.13, the slope of the line is given by the value of μ_{eff}. The theoretical value of μ_{eff} calculated using Equation 5.11 and the experimental value as calculated from the slope of the data was compared to judge the validity of the measurements.

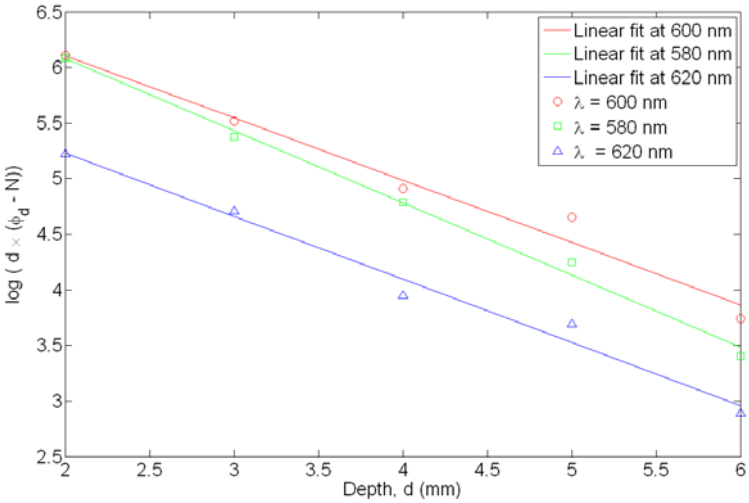

(c) Lung tissue phantom

Figure 5.6: Variation in signal strength with depth (Cont.)

As the dark noise is additive in nature, the measurements of signal strength shown in Figure 5.2.1 have an average noise added to it. This noise was removed before proceeding with the analysis of the measurements. The value of noise in each tissue phantom was taken as as the signal measurement at the position just below the calculated maximum depth of detection to avoid negative and zero values. The graphs showing the linear variation of the signal strength according to Equation 5.13 are shown in Figure 5.6. As can be seen from the graphs, the measurements were not perfectly linear and a line was fit to this data to measure the slope. Table 5.3 gives the norm of residual errors in fitting for each of the lines shown in Figure 5.6.

$\lambda(nm)$	Breast	Muscle	Lung
580	0.4915	0.1618	0.2732
600	0.3446	0.2508	0.1528
620	0.8858	0.1719	0.2316

Table 5.3: Norm of residual error in linear fit shown in Figure 5.6.

The slope of the line fit to the data above was used to compare the experimental

value of the slope with the theoretical value calculated using Equation 5.11. As the values of μ_s' and μ_a vary with wavelength, the value of the slope (μ_{eff}) will also be different for the different spectral bands. The theoretical value of μ_{eff} is calculated at 590 nm, using the value given in Table 5.1. Since the signal was not measured at 590 nm, the value of slope for the data measured at 600 nm was used for the comparison. Table 5.4 gives the comparison of these values.

$\lambda(nm)$	Breast	Muscle	Lung
Theoretical	0.1788	0.479	0.805
Experimental	0.1776	0.3656	0.6498

Table 5.4: Comparison of theoretical and experimental values of slope.

The disparity in the values shown in Table 5.4 may be attributed to the volumetric measurement of the absorbing and scattering agents added to the phantoms. This was followed by a comparison of the behaviour of light in each of the spectral band to see the attenuation of light in different types of tissues. The graphs given in Figure 5.7 show this comparison.

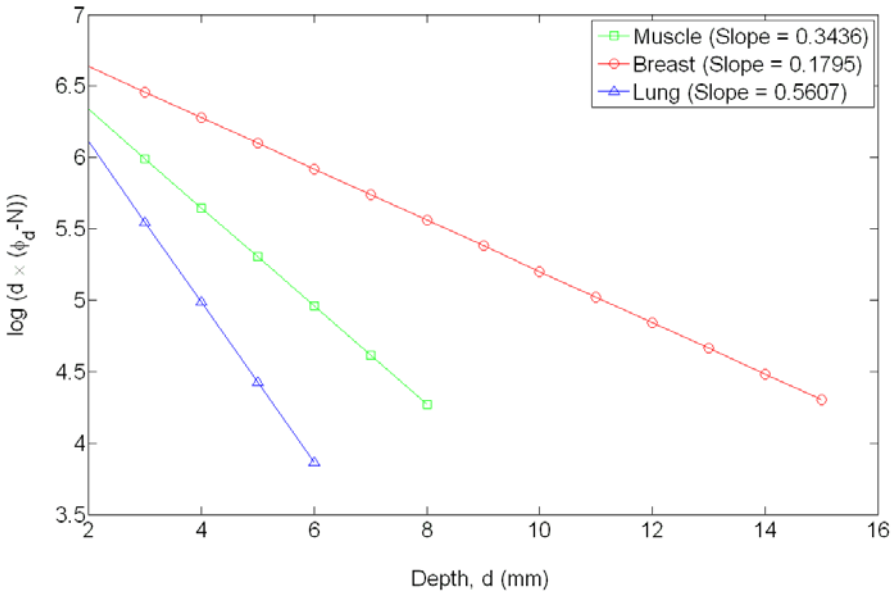

(a) $\lambda = 580$ nm

Figure 5.7: Comparison of attenuation in tissues

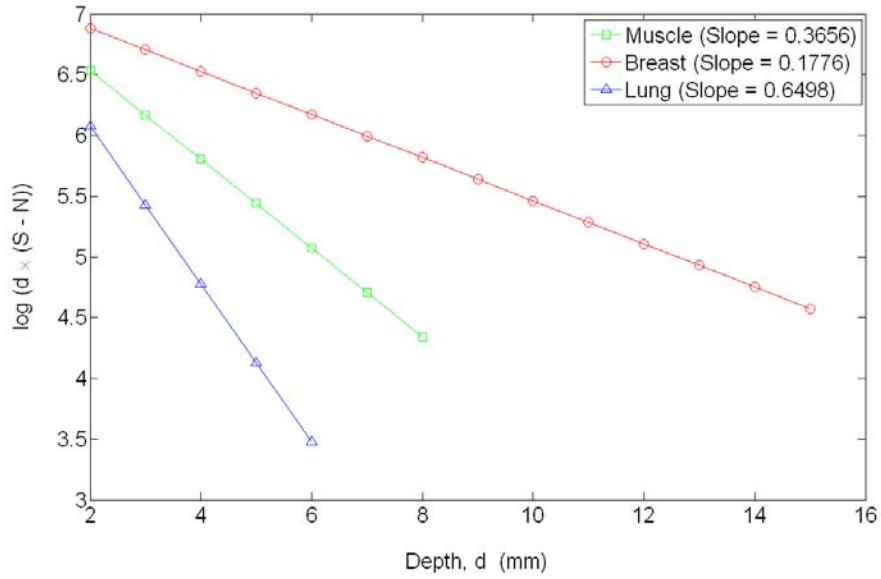

(b) $\lambda = 600$ nm

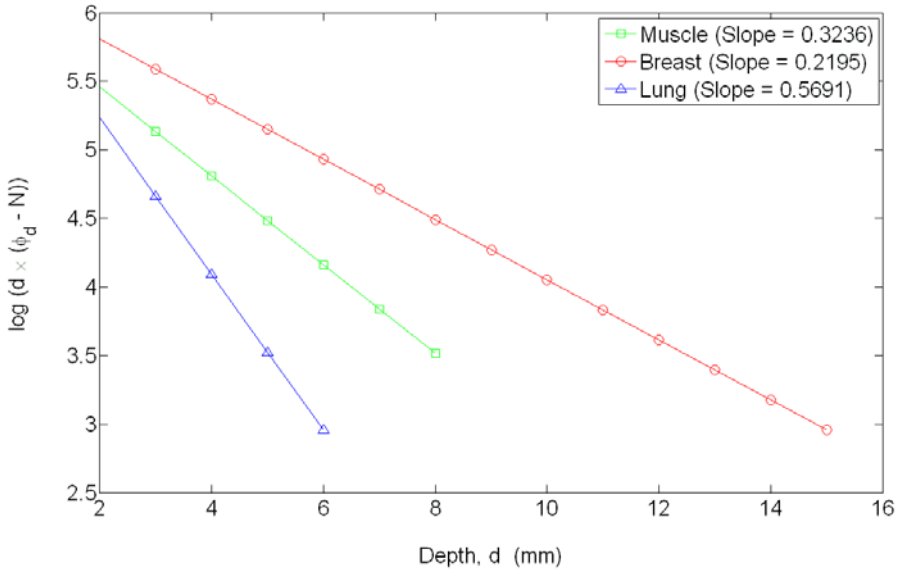

(e) $\lambda = 620$ nm

Figure 5.7: Comparison of attenuation in tissues (Cont.)

Figure 5.7 denotes that bioluminescence signal from small cancerlike volumes can be detected even after the photons propagate an average distance of 1 cm. The attenuation rate of the breast tissue is the lowest as expected however it can be seen that the signal strength at the maximum detectable depth is the highest for the 580 nm and 600 nm spectral band and approaches the signals levels in the other two phantoms only in the 620 nm band. In other words, bioluminescent signals from luciferase expression (550 nm – 600 nm) can propagate from deep within a highly transmitting tissue like the breast and heart. Similarly for the muscle tissue, the signal level detected at the maximum detectable depth is the highest for the 600 nm band. The lung tissue has the highest attenuation rate amond the three phantoms of 1 uint of magnitude every 2 mm.

5.3 Summary

In this chapter, the sensitivity of the sBLTI was scrutinized and it was found to be adequate for the detection of bioluminescence signals deep as 1.5 cm within the tissue. This estimate is conservative since technological advances to lead to significant detection improvement relative to the experimental setup used in this study. More efficient photon detection can be achieved by direct fiber coupling on the CCD chip or a 1:1 lens system. The primary cause of reduced sensitivity was the dark noise and this can be further reduced with the use of cooled CCD cameras allowing a deeper detection of the weak bioluminescent signals.

CHAPTER 6
Imaging Experiments

In the previous chapter the analysis of system noise and its effect on the sensitivity of the measurements was completed. In this chapter, the imaging protocol will be delineated and the results obtained at each step of the process will be discussed. The demonstration of the tomographic capability of the sBLTI required the use of a solid phantom. In the following sections, the preparation of the solid phantom will be explained, followed by the experimental protocol and subsequently the results obtained using the sBLTI.

6.1 Solid phantom preparation

As was discussed in the previou chapter, phantoms that simulate the optical properties of tissues are commonly used to mimic light distributions in living tissue. Solid tissue phantoms are often designed and utilized to simulate light distrinutions with a geometry of physical tissue. In this study the solid phantom was made by adding titanium dioxide (scattering agent) and ink (absorbing agent) to a solid matrix made of agar. The preparation of the agar matrix was done according to the method given in [35].

A highly purified agar powder (A-7049, Sigma-Aldrich, USA) is dissolved in distilled water in the concentration of 1 %, and heated upto the melting temperature of 95°C. A microwave oven was used for this purpose to avoid burning the agar. The agar matrix itself has negligible absorption and very low turbidity, thus the desired optical properties are reached by adding appropriate amounts of Titanium Dioxide (TI) , Ti-pure R-706 (DuPont, USA) and blue ink used previously in the liquid phantom; the details of which are given in the following sections. The optimal temperature for adding TI and ink to the agar is in the range of 80°C to 40°C. In this case, a suspension of TI was made in ethanol to avoid settling, and was added along with the ink at 60°C. At 40°C the solution was poured into a mould, which in this case was a 100 ml beaker and left for sometime. The solution was stirred

continously while cooling down to avoid the particles from settling down. The solution solidified in 30 minutes and was extracted from the mould and cut into two equal halves. In this study breast tissue phantom was prepared with $\mu_s' = 0.8mm^{-1}$ and $\mu_a = 0.004mm^{-1}$.

6.1.1 Optical properties of the phantom

TI is a commonly used scattering agent and its optical properties are critically dependent on the diameter of the particles. The optical properties of TI as given in [36] are defined by the following equations provided the mean diameter of particles is $340 \pm 90nm$,

$$\mu_{s,\lambda}' = 5.2(\frac{\lambda}{1000})^{-0.8} \tag{6.1}$$

$$\mu_{s,690}' = 8 \times c \tag{6.2}$$

where, c is the concentration in mg/mL. Combining the two equations, the relation between μ_s' and c can be written as

$$\mu_{s,\lambda}' = 11.59\, c\, (\frac{\lambda}{1000})^{-0.8} \tag{6.3}$$

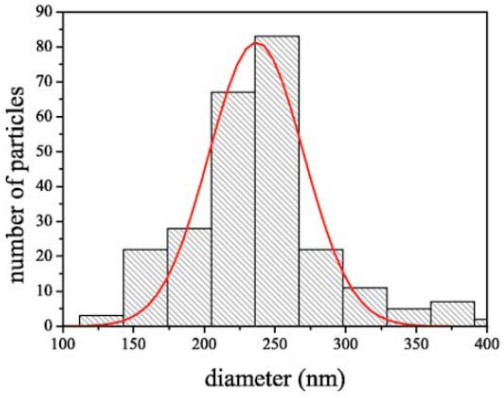

Figure 6.1: Distribution of TI particle diameter in Ti-Pure R-706.

The distribution of particle size of Ti-Pure R-706 is given in Figure 6.1. As can be seen, the mean diameter of the TI used in this study satisfies the condition for

Equation 6.3. Thus for a scattering coefficient of 0.8 mm^{-1} the mass of TI required was calculated to be 80.2271 mg. This TI was then mixed with 5 ml of ethanol to make a suspension mixed eventually with the agar solution.

As discussed in Section 5.1.2, the amount of ink to be added to the phantom can be derived using Equation 5.5. Thus using this relation, the volume of 5 % ink solution to be added to the agar phantom to impart μ_a equal to 0.004 mm^{-1} was found to be 20 μl.

6.1.2 Source simulation in phantom

In the solid phantom the multiple sources were simulated using the same method as was done in the case of the liquid phantom. The two sources were connected to the same LED source and had different core diameter. This ensured a different power at each source position. The position of the two sources is shown in Figure 6.2 along with a photograph of the setup. The phantom has black dye applied on the surface which be explained in the following sections.

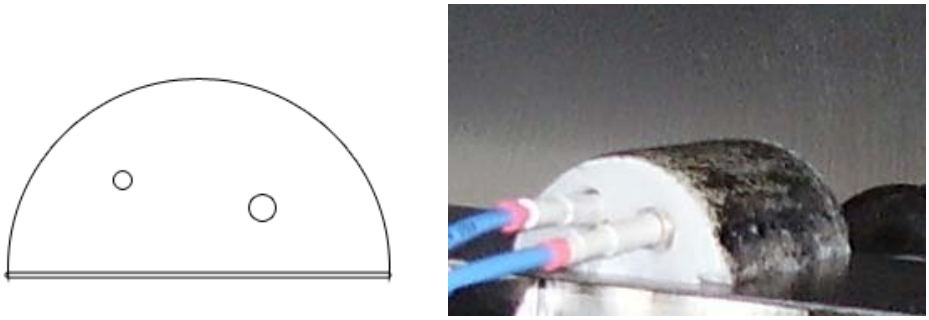

(a) Arrangement of the sources (b) Setup

Figure 6.2: Source simulation in solid phantom. The black dye is applied to the phantom after the acquisition of spectral data to impart a texture aiding the stereo reconstruction of the phantom.

6.2 Imaging Protocol

In this section the procedure of acquiring multiview multi-spectral images is explained. Figure 6.3, shows the intermediate positions of the camera as it is rotated

during the procedure while acquiring images. The reference angle is based on the CCD camera and measured in the clockwise direction.

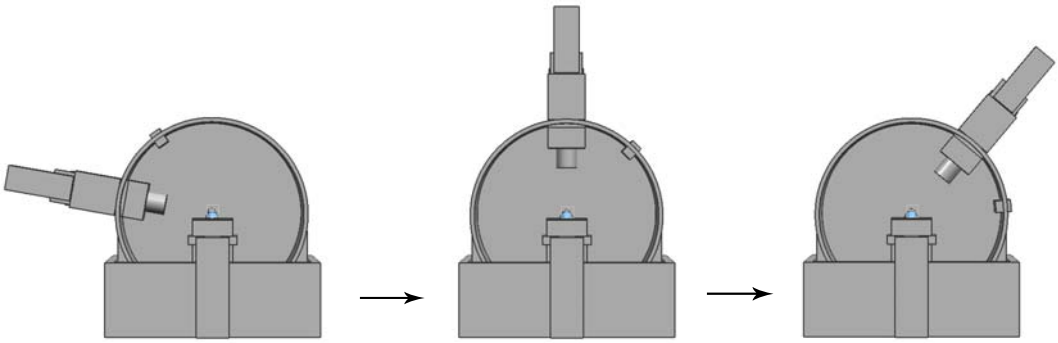

Figure 6.3: Schematic showing the camera positions during imaging as it is changed from 0° to 135°

1. The CCD camera and the stereo system are switched on. As per the characterisation of noise done in Section 4.2, the level of dark noise increases to a stable value in 18 minutes. The camera is setup for an exposure time of 700000μs and the software binning is turned off.

2. At the end of 18 minutes the first image is acquired on the CCD camera at 0° angle.

3. The 580 nm filter is attached to the lens of the camera and the image is acquired. The filter is then changed to 600 nm and then 620 nm and the images are acquired at the same angle. This completes the multispectral acquisition for one angle.

4. The system is then rotated by the prespecified angle.

5. This process continues till the CCD camera reaches and angle of 135° as shown in Figure 6.3.

6. Now the camera is rotated in the counter-clockwise direction and stops at 3 angles - 135°, 750° and 30°. at each of these locations the stereo camera acquires images and the point cloud (3D points representing the phantom/animal surface) are stored.

This concludes the acquisition of surface and bioluminescence data. All the post-procesing done on these images and point clouds is done offline.

6.3 Phantom Imaging Results

Figure 6.4 shows the preliminary imaging results for without the use of filters. In this experiment, images were acquired for three spectral bands and for 4 angular positions. It may however be mentioned that this system is capable of a much higher angular resolution. The simplicity of the phantom surface made images acquired that smaller angular gaps redundant. As can be seen from this figure, the shape of the phantom is clearly visible and this is useful in registration of the spectral images with the 3D surface. These images also give a fair idea of the relative strength of the two sources. A comparison of the images in Figure 6.4 and the following Figure 6.5 will also show the use of filters in removing artefacts from the signals acquired.

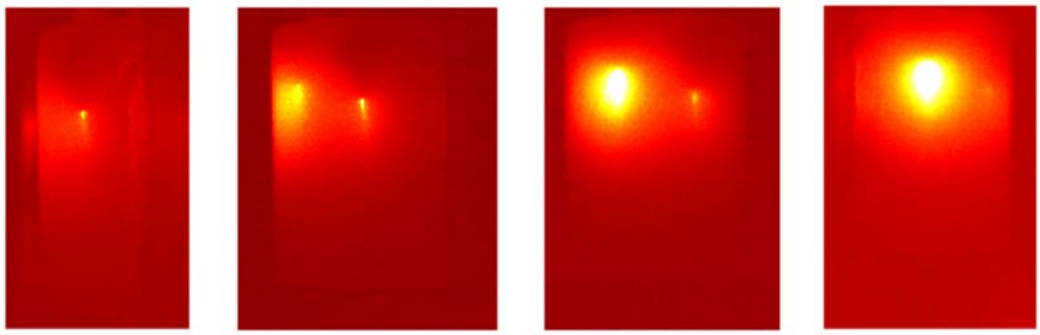

Figure 6.4: Multiview acquisition made without using filters. The images are at an angle of 0°, 45°, 90° and 135° from left to right.

The images acquired using the CCD camera are noisy and just as was done in case of the liquid phantom, anscombe filter was used to remove the poisson noise from these images. Figure 6.5 shows the results of acquisition by the protocol described above. The variation in signal strength that was observed in the liquid phantom can be seen in this case as well with the images in the 600 nm spectral band having the highest intensity and the images in the 620 nm band having the weakest strength.

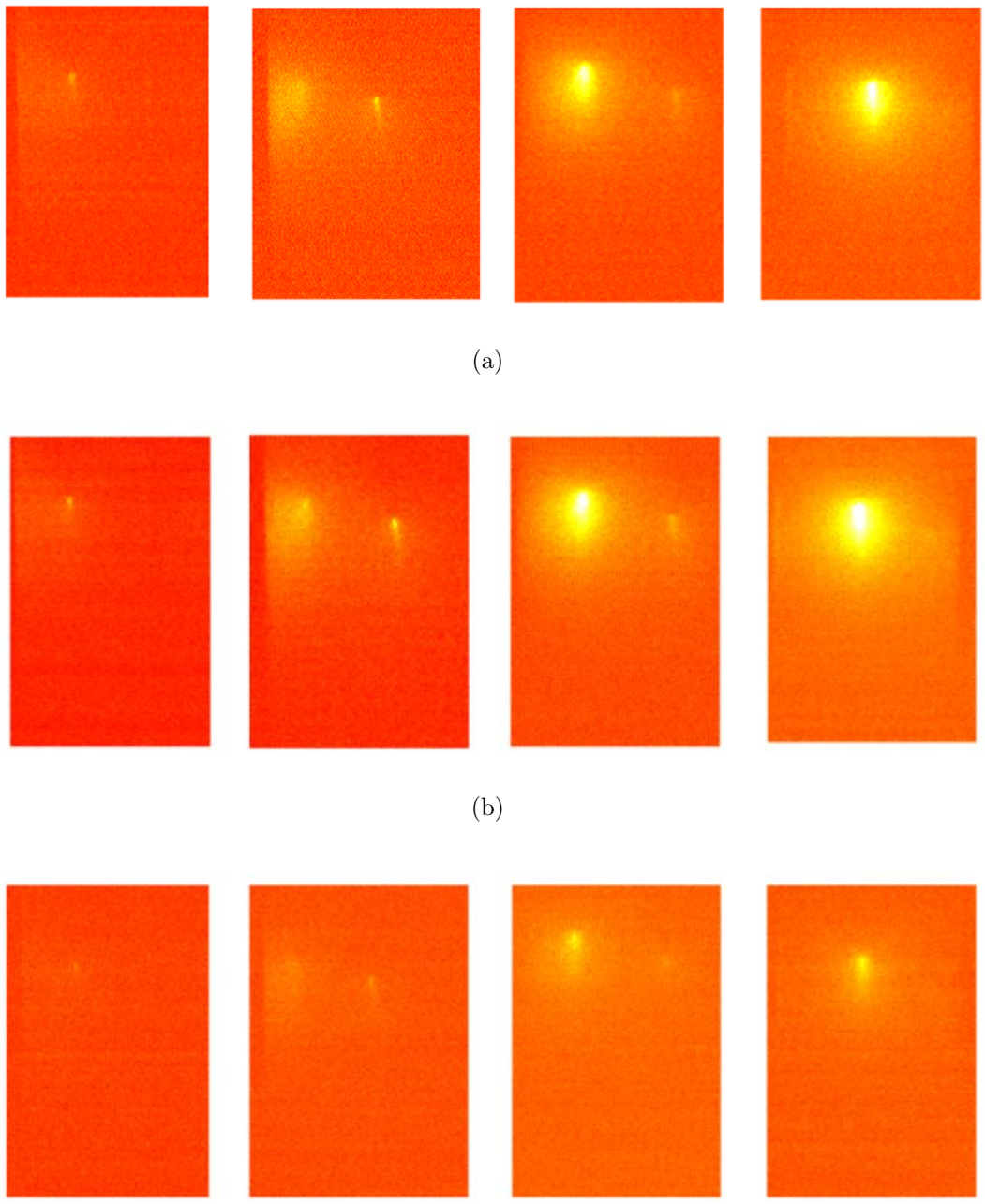

(a)

(b)

(c)

Figure 6.5: Multi-view acquisition of two bioluminescence signals in 3 spectral bands. (a) $\lambda = 580$ nm, (b) $\lambda = 600$ nm and (c) $\lambda = 620$ nm. The four images in each spectral band are at an angle of 0°, 45°, 90° and 135° from left to right.

6.4 Surface Extraction Results

This step in the 3D measurement generation process requires the maximum amount of post processing and a large part of this step is done manually. The stereo reconstruction process is based on the matching of features in two views of the same object. Features are most commonly present on the surface of a mouse inclusive of the skin and hair is sufficient to impart texture for a good reconstruction. The surface of the solid phantom however is smooth and glossy. This presented significant problems in the accurate reconstruction of the phantom surface. The issue was dealt with by applying a black dye on the surface to generate an irregular pattern which will assist the feature matching process. The dye was applied after the bioluminescence signals were acquired and before the counter-clockwise rotation was started.

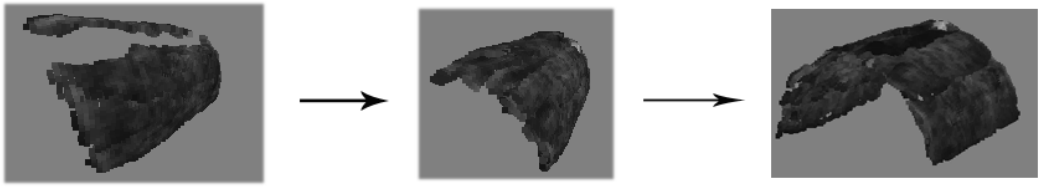

Figure 6.6: Combining point clouds from 3 different views of the phantom.

Figure 6.6 shows the steps of the surface reconstitution after the point cloud is obtained from the three views. This process involves rotation and transformation of each individual point cloud such that they are perfectly registered. The software used for this process was developed at the Advanced Computational Research Laboratory in the Mechanical Engineering department. This step directly affects the accuracy of the reconstructed surface and is therefore very critical.

The reconstituted phantom point cloud is shown in Figure 6.7. This completes the first step of surface extraction. In order to test the performance of the stereo camera system in reconstructing a more complicated surface such as in the case of a mouse, the surface of a toy mouse was extracted. The results of the surface reconstitution of the mouse are shown in Figure 6.8.

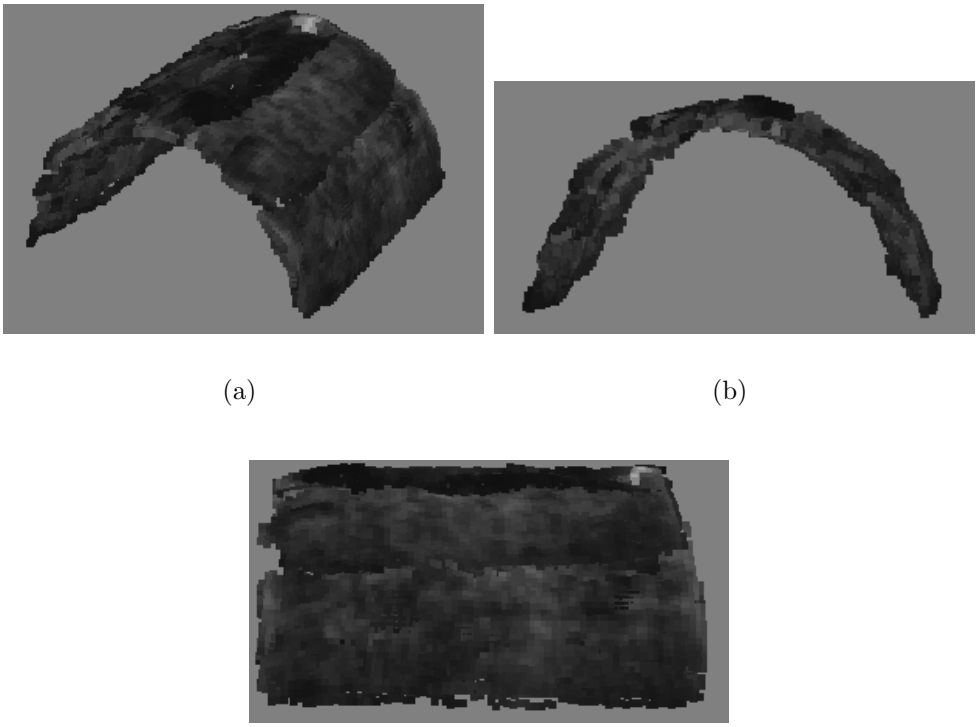

(a) (b)

(c)

Figure 6.7: (a) The reconstituted phantom surface (b) Front view of the phantom surface (c) Side view of the phantom surface

It was seen that the reconstruction failed at the extremities of the mouse body however, the application of bioluminescence in mouse studies concentrates mainly on the torso which has been reconstructed accurately.

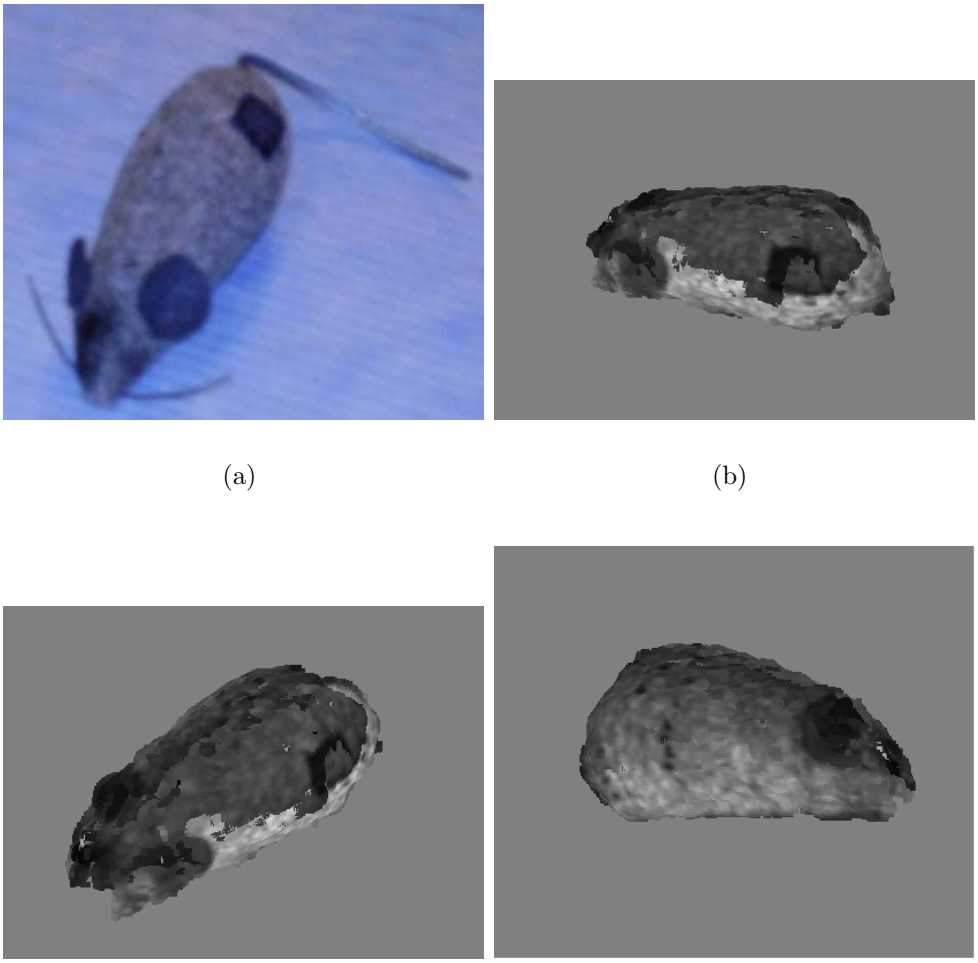

(a) (b)

(c) (d)

Figure 6.8: (a) Toy mouse used for reconstruction (b) Left view of the mouse surface (c) Top view of the mouse surface (d) Right view of the mouse surface

The next step in surface extraction is rescaling of the point cloud. The software used for reconstitution scales the 3D coordinates with reference to the camera axis. While this does not introduce significant errors in the surface extraction process, it becomes important to rescale the coordinates before registering the bioluminescence signal and the 3D surface. The size of the phantom used for this study was measured to be a semi-cylinder of radius 2.3 cm and length 5.3 cm. In this case the process of rescaling the reconstructed suface becomes trivial. In actual mouse studies the images obtained from the CCD camera as shown in Figure 6.4 are useful to measure

the dimensions of the subject and scale the points accordingly. Another method that may be employed for this purpose is the use of a reference object on the imaging stage whose dimensions are known beforehand and that can be used for rescaling the point coordinates.

After the reconstituted points are scaled to the correct value, a surface was fit through the points. This is a time consuming process and will be difficult to incorporate this process online. The *gridfit* function in Matlab was used to fit the surface and the results of the surface fitting are shown in Figure 6.9.

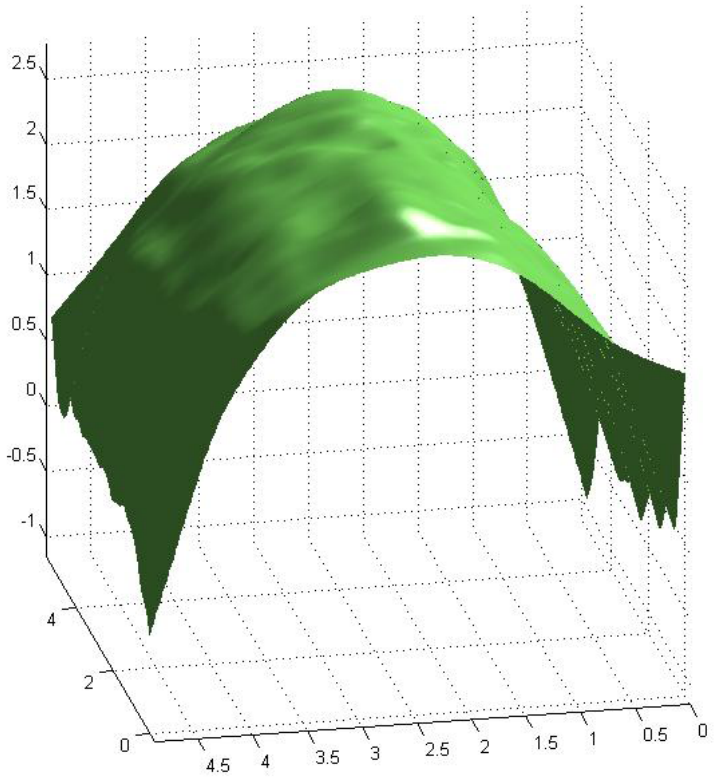

Figure 6.9: Surface of the phantom as obtained by fitting a surface to the reconstituted point cloud.

This completes the surface extraction process and before proceeding further, the accuracy of the stereo system was determined by comparing the reconstructed surface with a model cylinder of the dimensions of the phantom. Figure 6.10 shows the reconstructed surface overlayed on the model surface being use for comparison. It can be clearly seen that the reconstruction is not completely accurate. The error

in the reconstruction was quantified by measuring the maximum deviation from the model surface in the y-z plane and in the x-z plane. Figure 6.11 shows the error in the reconstruction in these two planes.

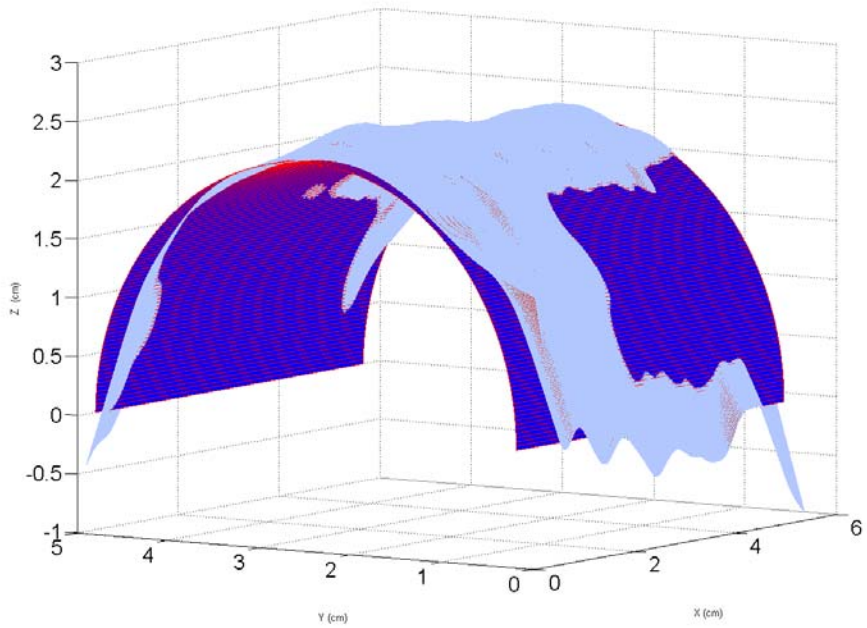

Figure 6.10: Reconstructed surface compared with a model surface of the phantom.

It can be seen from Figure 6.11 that the maximum error in the reconstructed surface is in the negative z-axis. This is extension in the reconstructed surface is automatically generated by the *gridfit* function to maintain the smoothness constraint of the surface. This error can be ignored. The other error in the reconstruction is in the form of bumps on the surface which as mentioned before is due to misalignment in the different sections of point clouds. This error is not visible while manually registering the clouds but is very evident in the surface generated. As noted in the figure, the maximum value of this deviation was found to be $\sim$ 2 mm.

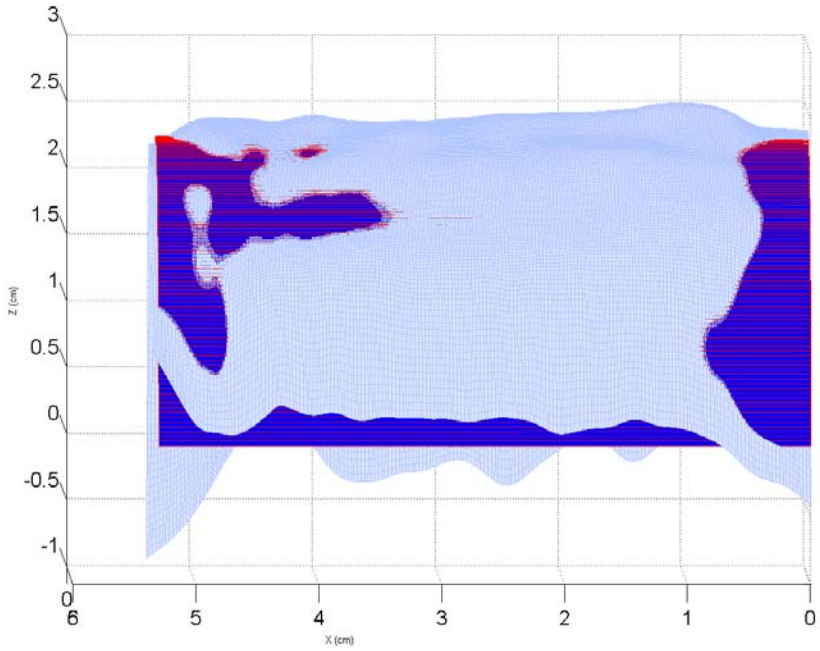

(a)

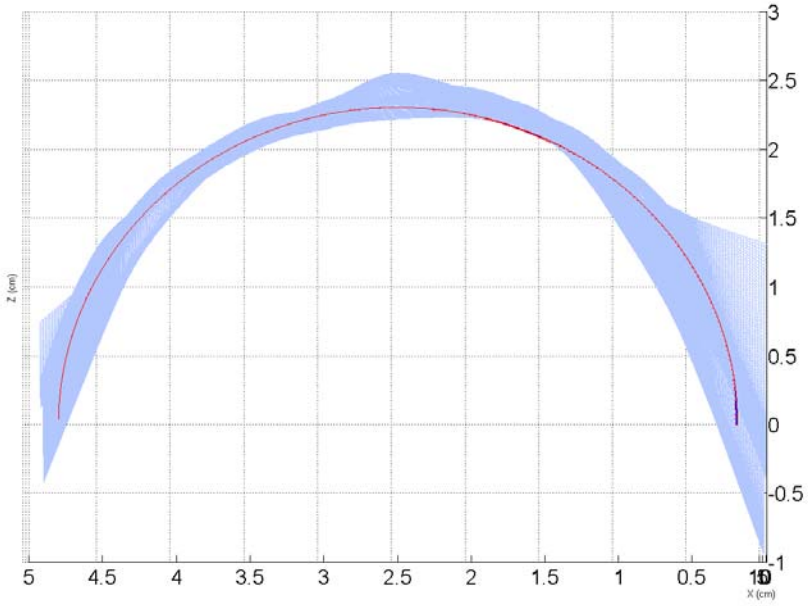

(b)

Figure 6.11: (a) Error in the x-z plane with a maximum value of $\sim$ 1 mm. (b) Error in the y-z plane with an average value of $\sim$ 1 mm and maximum value of $\sim$ 2 mm.

6.5 3D Data Representation

In this step the multispectral images acquired from different angles are superimposed on the surface reconstructed in the previous section. The reconstructed surface is defined in terms of a meshgrid which spans the x and y coordinates. If there are m points in the x direction and n points in the y direction, then the height which defines the surface is given as a matrix of values of size $m \times n$. The value of photon count as obtained from the CCD camera can be represented on the surface based on a $m \times n$ matrix with each value of the matrix giving the photon count for one 3D point on the surface.

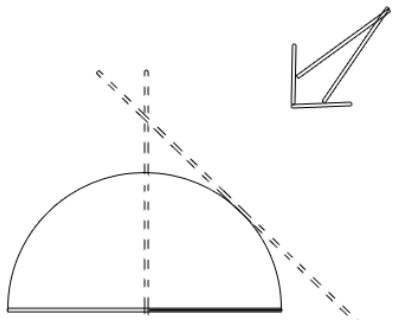

Figure 6.12: The concept behind overlaying 2D images on a 3D surface.

The concept behind overlaying the 2D image on the 3D surface can be better explained using Figure 6.12. Henceforth, the matrix containing the values of the photon counts shall be referred to as c. In the Figure 6.12, the bottom line represents c. At this point, a particular view of the phantom is available along with the 3D matrices. Assuming that every pixel is representative of a single point on the surface, the field of view captured in the image is shown by the dotted line. The values of the subset of c as marked in Figure 6.12 are given in the image as intensity values. These values are assigned by resizing the image to the size of this subset of c. This process is repeated for all the angles at which data is obtained. In case of overlapping values, the average value was assigned to the cell in c.

The results of the registration of 2D image from the 600 nm dataset and the 3D surface extracted in the previous step is shown in Figure 6.13.

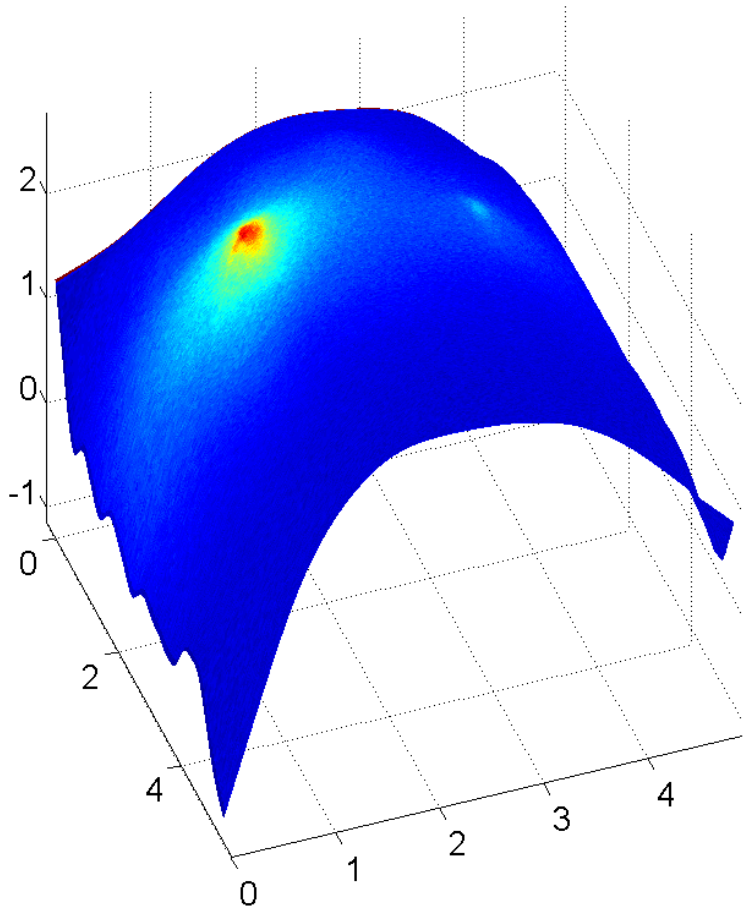

Figure 6.13: The final representation of the tomographic data acquired using sBLTI.

6.6 Summary

In this chapter, the data generation procedure using the sBLTI was explained in detail starting from the preparation of the phantom to the 3D data of light emission measured on its surface. The acquisition system was able to acquire quality multispectral multi-view images. It was seen that the stereo system does not provide a completely accurate reconstruction, however the errors introduced are not severe and can be avoided by employing some basic image processing principles.

CHAPTER 7
Discussion

The current state of this research project and the likely future work are reviewed in this final chapter. In addition, possible design features of any next generation device are discussed.

7.1 The Platform

During this research project a computer-controlled platform capable of imaging weak bioluminescence signal over multiple spectral bands exiting a small animal body from different angles was constructed. A novel feature of this system is the 3D surface extraction and projecting the 2D exittance measurements onto this surface to generate tomographic bioluminescence data. Following the fabrication of the system it was characterized and its capabilities were studied. The preliminary phantom studies performed during the course of this project demonstrated a good accuracy of the tomographic measurements. The following are some of the key features of this design.

- The platform was designed as a modular device allowing suitable changes and addition of devices to the basic imager.

- The imager works on the principle of rotating the imaging devices about the subject. The automation of the system is accomplished by controlling the rotation of the acquistion system using a servo motor and this allows precise and accurate control. It was shown that the system can acquire images at an angular seperation as low as 5°.

- The CCD camera used for imaging the signals has a very high quantum efficienvy of $\sim$ 70 % over the spectral range of interest (550 nm - 700 nm). The maximum exposure time of 100 ms ensures a high sensitivity. Moreover software control of the acquisition allows noise control and accurate measurements online.

- The filter set currently being used comprises of interference filters having a high transmission ($\sim$ 65 %) and a very bandwidth which ensures a spectral resolution of 10 nm.

- The other important component of this platform is the Bumblebee Stereo camera system which allows a reconstruction of the subject surface which is used in 3D quantifiation of the tomographic measurements.

7.1.1 Mechanical modifications

During the process of characterisation, a few features of the platform's mechanical design were shown to contribute a mechanical bias to the measurements. While these errors were not significant in affecting the accuracy of the results, the following changes will allow improvement in performance of the system for future studies.

- One of the most time consuming stages during the development of this platform was the automation based on servo control. The capability of the system in adding imaging devices is restricted by the capability of the motor in providing the requisite torque. One of the first modification to be made in this system is the addition of a 2:1 gear system to improve the torque supplied by the motor. While this reduces the angular velocity and thereby the imaging time, the continous-wave nature of the bioluminescence signals provides enough margin to increse the imaging time.

- The second modification which has already been planned for is the increasing the angular range of system rotation from the present 135° to 180°. This will be accomplished by making design changes to the supporting base.

- The experiments conducted for measuring the mechnical bias of the system showed that there is an inherent ellipticity in the system's mechanical design. The effect of this error was offset by moving the specimen to the new axis of rotation. The cause of this ellipticity was found to be in the camera mounting frame and this error can be fixed with a few minor changes.

- The stereo system requires a working distance of 12 " to acquire a more artefact free reconstruction. At present it is placed at a distance of 13 " from the subject however, changes will be made in the platform to increase the working distance of the stereo camera, while considering the ellipticity of the system. The change in the system's position will affect the torque required to rotate the imager and therefore, this change will be compromise arrived at through further investigations.

7.1.2 Performance

The sensitivity of the system in imaging weak signals travelling through the tissue was analysed in Chapter 5. The results were satisfactory and comparable to the results from instruments available in the industry and the academia. The multi-view capability of this system based on rotation of the imaging devices ensures an accurate and complete measurement as opposed to the simultaneous acquisition from multiple angles done in many of the systems. The errors in positioning the system were seen to be not more than 3° which makes for a strong arguement in favor of this concept. However two changes may be suggested which will further improve the sensitivity of this system to noise.

- The initial results obtained from the CCD images show a high sensitivity of this system to ambient noise despite taking the images in a dark room due to the light from the computer screens. It is therefore proposed that a light-tight enclosure be built around the platform to block out any ambient light and further increase the SNR in the acquire images.

- One of the objectives stated at the beginning of this project was multi-spectral acquisition at a very high spectral resolution. Due to the unavailability of high-transmission filters which can be controlled through the computer, a part of the acquisition process had to be carried out manually. Several options involving Liquid Crystal Tunable filters are being explored which will give this system more range in spectral imaging.

7.2 3D reconstruction and quality

Generation of the 3D results by projecting the 2D bioluminescence images onto the 3D surface extracted using the stereo system is the crux of the image reconstruction process. The more critical aspect of this step is the surface extraction and it has proven to be prone to change in illumination. Increasing the working distance of the stereo system will help reduce the artefacts in the reconstructed surface visible as bumps and deformations. The Triclops library provided with the stereo system has provisions for assigning translation and rotation transformations to the derived point cloud. This will negate the need for manual reconstitution of the point clouds. Moreover, further post processing of the pointcloud by delineating a clear boundary on the surface will provide a smoother reconstruction. Another component of the imaging platform that is presently being developed is a software wrapper encapsulating the different control software under a single user-friendly interface.

7.3 Future imaging studies

As of now, a platform capable of generating accurate 3D exitance map of bioluminescence signals from a small animal has been developed. However, one of the major obstacles in completing the remaining steps of bioluminescence tomography is the inverse source problem. This inverse problem assumes the knowledge the optical properties of the small animal being imaged and the inherent heterogeneity of the optical properties presents a difficult problem in this regard. The use of time-resolved optical imaging is being explored as means of determining the values of optical properties in the subject body.

Time-resolved optical imaging works on the principle of measuring the spread in laser pulses as they travel through the subject body and measuring the optical properties from this spread. As mentioned earlier, this platform was designed as a modular system. The major device addition required for this technique includes, a pulsed diode laser, a gated intensifier to be used in conjunction with the CCD camera and an X-Y scanner which will be used to direct the laser across the subject body, meauring the pulse spread and thereby the optical properties. The CCD

camera being used, Imager 3 QE from LaVision systems is part of the Picostar which also includes an intensifier which has a temporal resolution of 200 ps. Our lab already has a Mai-Tai laser from Spectraphysics capable of wavelengths ranging from 700 nm – 1100 nm. Also with the present system design the galvo scanner can be placed within the specimen stage. The combination of these two methods is a novel solution to the conventional problems in bioluminescence tomography.

Another direction being investigated in the current state of this research is the combination of multiple imaging modalities. This refers to the use of other systems like MicroCT or MRI systems for small animals in conjunction with this system to improve the accuracy of the tomographic bioluminescence measurements.

7.4 Conclusion

In conclusion, I have developed a prototype multiview multispectral bioluminescence tomography system, evaluated its performance and successfully obtained initial tomographic phantom images. The accuracy of the source location calculated from these measurements however can only be judged after the inverse source problem is solved. The sensitivity and prospects presented by this system is however particularly encouraging. Future work will focus on further assisting the problem of inverting the tomographic measurements to determine the source location by determining the optical properties for each individual test subject using time-resolved imaging technique. Moreover the modular nature of this system makes it suitable for application in multiple optical imaging techniques by making minor changes to the platform itself. This will provide us with a robust optical measurement system finding applications in current research in optical imaging techniques.

BIBLIOGRAPHY

[1] T. F. Massoud and S. S. Gambhir. Molecular imaging in living subjects: seeing fundamental biological processes in a new light. *Genes and Dev.*, 17:545–580, 2003.

[2] M. Cutler. Transillumination as an aid in the diagnosis of. breast lesions. *Surg. Gynecol. Obstet.*, 48:721–730, 1929.

[3] T. Vo-Dinh, editor. *Biomedical Photonics Handbook*. CRC Press, 2003.

[4] A. Yodh and B. Chance. Spectroscopy and imaging with diffusing light. *Phys. Today*, 48:34–40, 1995.

[5] A. Vogel and V. Venugopalan. Mechanisms of pulsed laser ablation of biological tissues. *Chem. Rev.*, 103:577–644, 2003.

[6] I. J. Bigio and J. R. Mourant. Ultraviolet and visible spectroscopies for tissue diagnostics: fluorescence spectroscopy and elastic-scattering spectroscopy. *Eur. J. Cancer*, 38, 2002.

[7] X. Intes, J. Ripoll, Y. Chen, S. Nioka, A. G. Yodh, and B. Chance. In vivo continuous-wave optical breast imaging enhanced with indocyanine green. *Med. Phys.*, 30(6):1039–1047, June 2003.

[8] D. J. Hawrysz and E. M. Sevick-Muraca. Developments toward diagnostic breast cancer imaging using near-infrared optical measurements and fluorescent contrast agents. *Neoplasia*, 2:388–417, 2000.

[9] B. Ballou, G. W. Fisher, T. R. Hakala, and D. L. Farkas. Tumor detection and visualization using cyanine fluorochrome-labeled antibodies. *Biotechnol. Prog.*, 13(5):649–658, 1997.

[10] V. Ntziachristos, C. Tung, C. Bremer, and R. Weissleder. Fluorescence molecular tomography resolves protease activity in vivo. *Nature Medicine*, 8:757–761, June 2002.

[11] C. H. Contag and B. D. Ross. It's not just about anatomy: In vivo bioluminescence imaging as an eyepiece into biology. *J. Magn. Reson. Imaging*, 16:378–387, 2002.

[12] T. Wilson and J.W. Hastings. Bioluminescence. *Annu. Rev. Cell Dev. Biol.*, 14:197–230, 1998.

[13] B. W. Rice, M. D. Cable, and M. B. Nelson. In vivo imaging of light-emitting probes. *J. Biomed. Optics*, 6:432–440, 2001.

[14] H. L. Rocchetta, C. J. Boylan, J. W. Foley, P. W. Iversen, D. L. LeTourneau, C. L. McMillian, P. R. Contag, D. E. Jenkins, and T. R. Parr Jr. Validation of a noninvasive, real-time imaging technology using bioluminescent escherichia coli in the neutropenic mouse thigh model of infection. *Antimicrob. Agents and Chemotherap.*, 45(1):129–137, 2001.

[15] M. Edinger, T. J. Sweeney, A. A. Tucker, A. B. Olomu, R. S. Negrin, and C. H. Contag. Noninvasive assessment of tumor cell proliferation in animal models. *Neoplasia*, 1:303–310, 1999.

[16] A. Wetterwald, G. van der Pluijm, and I. Que. Optical imaging of cancer metastasis to bone marrow: a mouse model of minimal residual disease. *Am. J. Pathol.*, 160:1143–1153, 2002.

[17] M. Edinger, Y. A. Cao, Y. S. Hornig, D. E. Jenkins, M. R. Verneris, M. H. Bachmann, R. S. Negrin, and C. H. Contag. Advancing animal models of neoplasia through in vivo bioluminescence imaging. *Eur. J. Cancer*, 38:2128–2136, 2002.

[18] A. Nakajima E. V. Nguyen C. Taylor-Edwards A. J. Slavin C. H. Contag C. G. Fathman G. L. Costa, M. R. Sandora and J. M. Benson. Adoptive immunotherapy of experimental autoimmune encephalomyelitis via t cell delivery of the il-12 p40 subunit. *J. Immunol.*, 167:2379, 2001.

[19] L. D. Stegman U. Prasad G. Chen M. S. Bhojani T. L. Chenevert B. D. Ross A. Rehemtulla, D. E. Hall. Molecular imaging of gene expression and efficacy following adenoviral-mediated brain tumor gene therapy. *Mol. Imaging*, 1:43, 2002.

[20] G. S. Lipshutz, C. A. Gruber, Y. Cao, J. Hardy, C. H. Contag, and K. M. L. Gaensler. In utero delivery of adeno-associated viral vectors: Intraperitoneal gene transfer produces long-term expression. *Mol. Therapy*, 3:284–292, 2001.

[21] M. Allard, D. Côté, L. Davidson, J. Dazai, and R. M. Henkelman. Combined magnetic resonance and bioluminescence imaging of live mice. *J. Biomed. Optics*, 12(3), May/June 2007.

[22] G. Alexandrakis, F. R. Rannou, and A. F. Chatziioannou. Tomographic bioluminescence imaging by use of a combined optical-pet (opet) system: a computer simulation feasibility study. *Phys. Med. Biol.*, 50(17):4225–4241, September 2005.

[23] High sensitivity cameras : Principle and technology. Technical report, Hamamatsu Photonics K. K., 2006.

[24] M. Oshiro. Cooled ccd versus intensified cameras for low-light video–applications and relative advantages. *Methods Cell Biol.*, 56:45–62, 1998.

[25] C. Kuo, O. Coquoz, T. L. Troy, H. Xu, and B. W. Rice. Three-dimensional reconstruction of in vivo bioluminescent sources based on multispectral imaging. *J. Biomed. Optics*, 12(2), March/April 2007.

[26] http://www.xenogen.com/wt/page/imaging. Xenogen Imaging Systems website.

[27] G. Wang, W. Cong, Y. Li, W. Han, K. Durairaj, X. Qian, and H. Shen. Recent development in bioluminescence tomography. In *3rd IEEE International Symposium on Biomedical Imaging: Macro to Nano*, pages 678–681, 6-9 April 2006.

[28] G. Wang, H. Shen, K. Durairaj, X. Qian, and W. Cong. The first bioluminescence tomography system for simultaneous acquisition of multiview and multispectral data. *Intl. J. Biomed. Imaging*, 2006.

[29] A. J. Chaudhari, F. Darvas, J. R. Bading, R. A. Moats, P. S. Conti, D. J. Smith, S. R. Cherry, and R. M. Leahy. Hyperspectral and multispectral bioluminescence optical tomography for small animal imaging. *Phys. Med. Biol.*, 50, 2005.

[30] H. Dehghani, S. C. Davis, S. Jiang, B. W. Pogue, K. D. Paulsen, and M. S. Patterson. Spectrally resolved bioluminescence optical tomography. *Opt. Lett.*, 2006.

[31] A. Corlu, T. Durduran, R. Choe, M. Schweiger, E. M. C. Hillman, S. R. Arridge, and A. G. Yodh. Uniqueness and wavelength optimization in continuous-wave multispectral diffuse optical tomography. *Opt. Lett.*, 28(23), December 2003.

[32] R. J. Valentine. *Motor Control Electronics Handbook*, chapter 2. McGraw-Hill, 1998.

[33] K. M. Yoo, B. B. Das, and R. R. Alfano. Imaging of a translucent object hidden in a highly scattering medium from the early portion of the diffuse component of the transmitted ultrafast laser pulse. *Opt. Lett.*, pages 958–962, 1992.

[34] H. J. van Staveren, C. J. M. Moes, J. van Marle, S. A. Prahl, and M. J. C. van Gemert. Light scattering in intralipid-10 % in the wavelength range of 400-1100 nm. *Appl. Opt.*, 30(31):4507–4514, 1991.

[35] R. Cubeddu, A. Pifferi, P. Taroni, A. Torricelli, and G. Valentini. A solid tissue phantom for photon migration studies. *Phys. Med, Biol.*, 42:1971–1979, 1997.

[36] T. Moffitt, Y. Chen, and S. A. Prahl. Preparation and characterization of polyurethane optical phantoms. *J. Biomed. Optics*, 11(4), 2006.

APPENDIX A
Technical Drawings

This chapter catalogs the technical drawings of the Multispectral Bioluminscence Tomographic Imager. The following are the parts that have been shown:

- Figure A.1 – The Final Assembly.
- Figure A.2 – The Mounting Drum.
- Figure A.3 – The Supporting Base .
- Figure A.4 – The Specimen Stand.
- Figure A.5 – The Camera Frame.

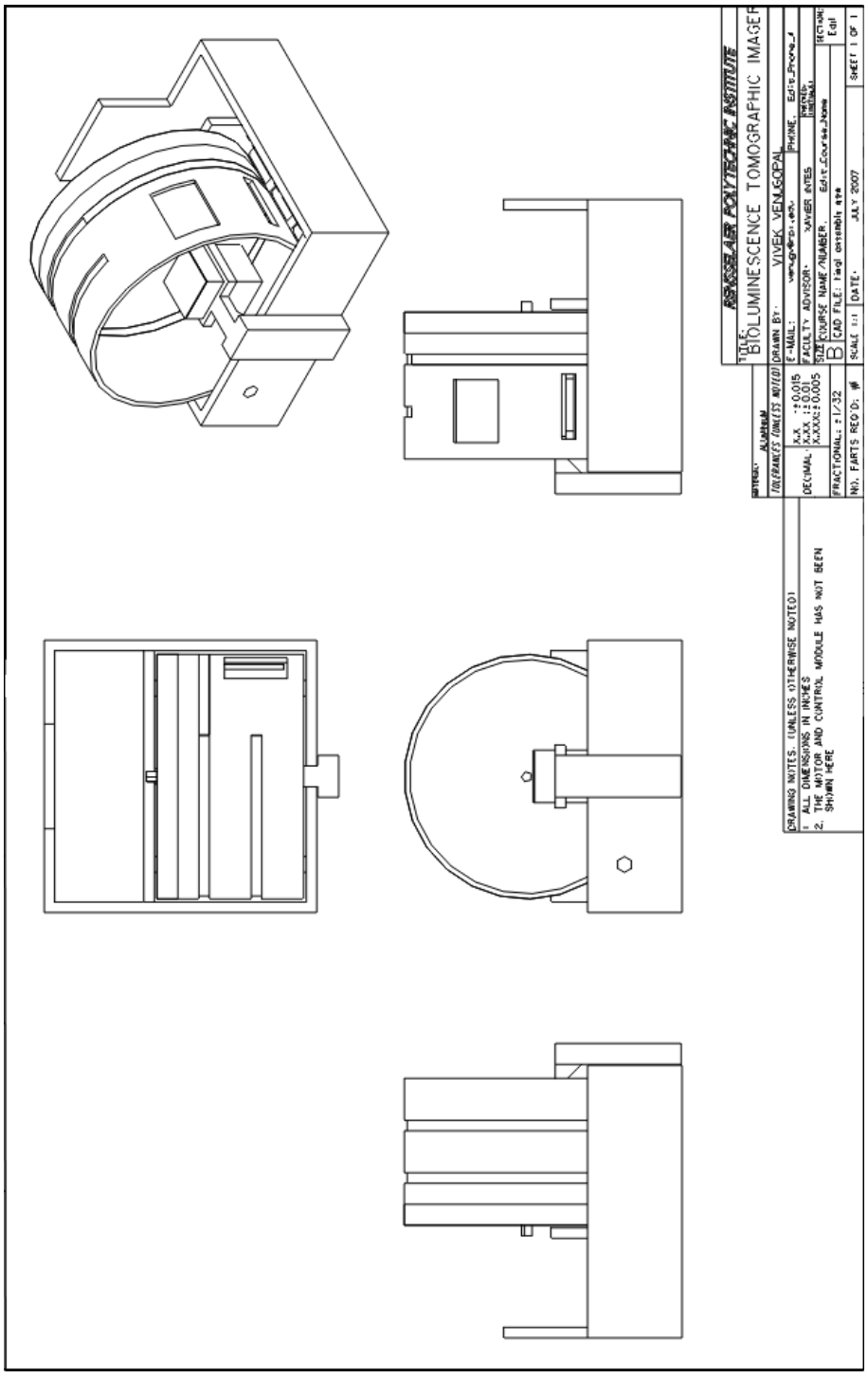

Figure A.1: The Final Assembly

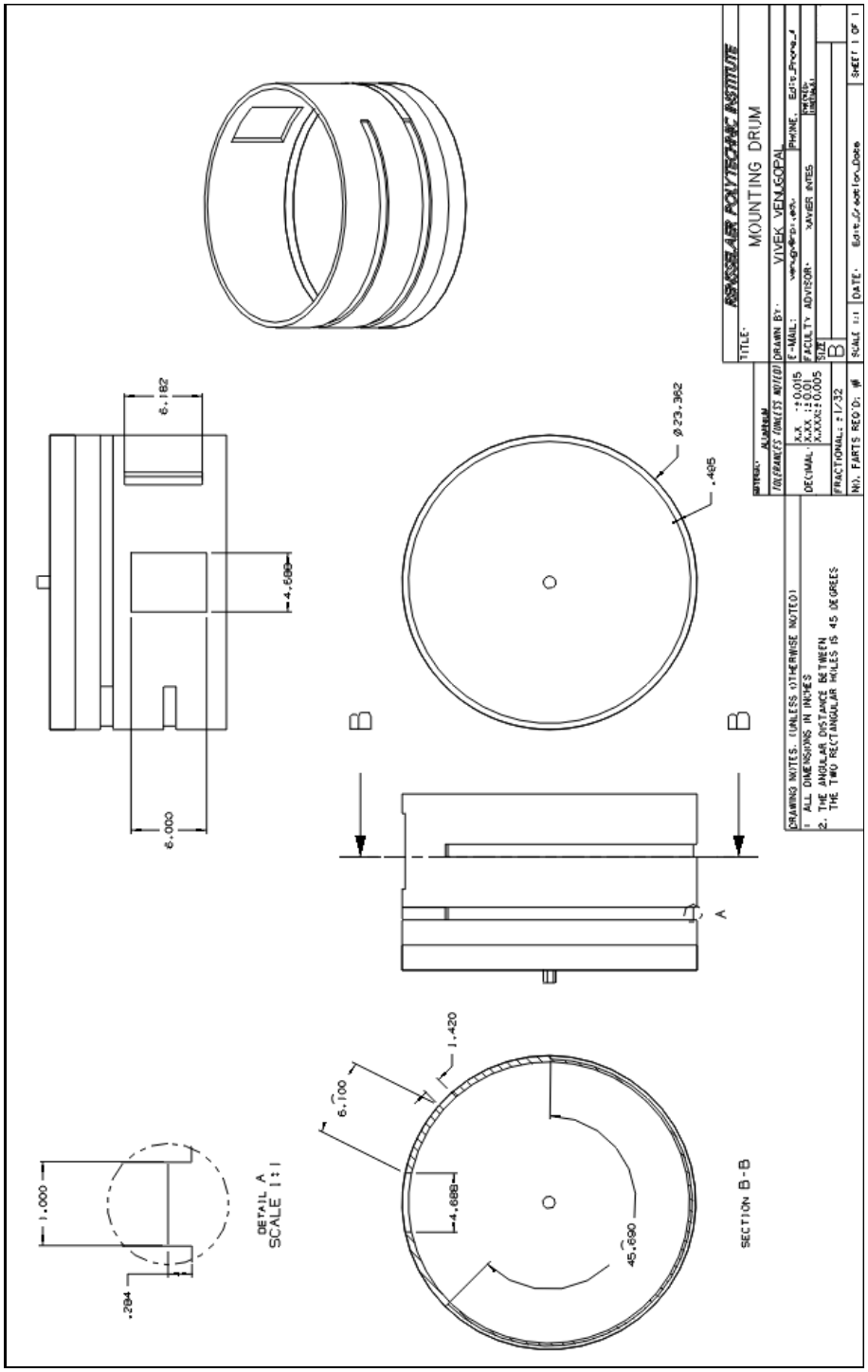

Figure A.2: The Mounting Drum

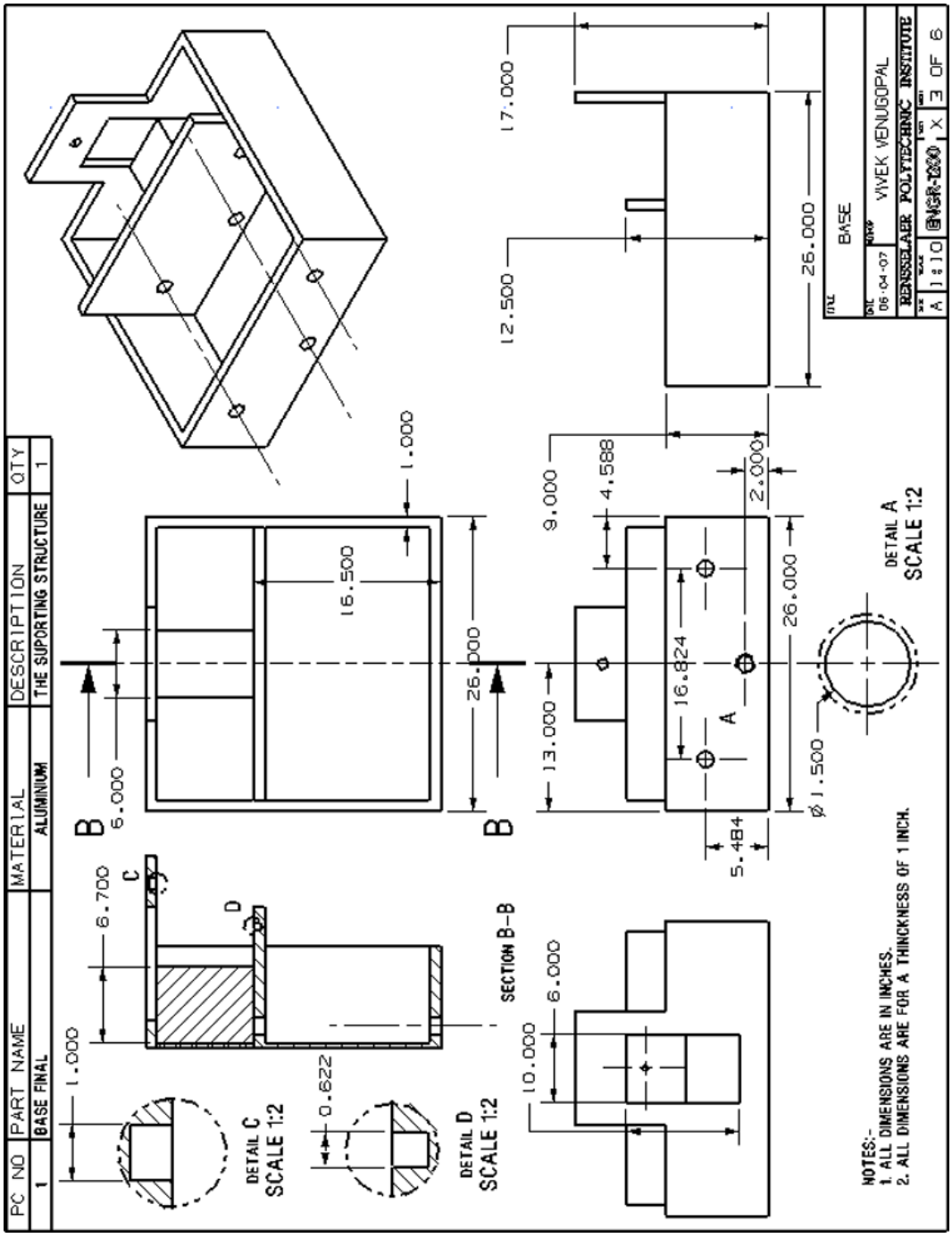

Figure A.3: The Supporting Base

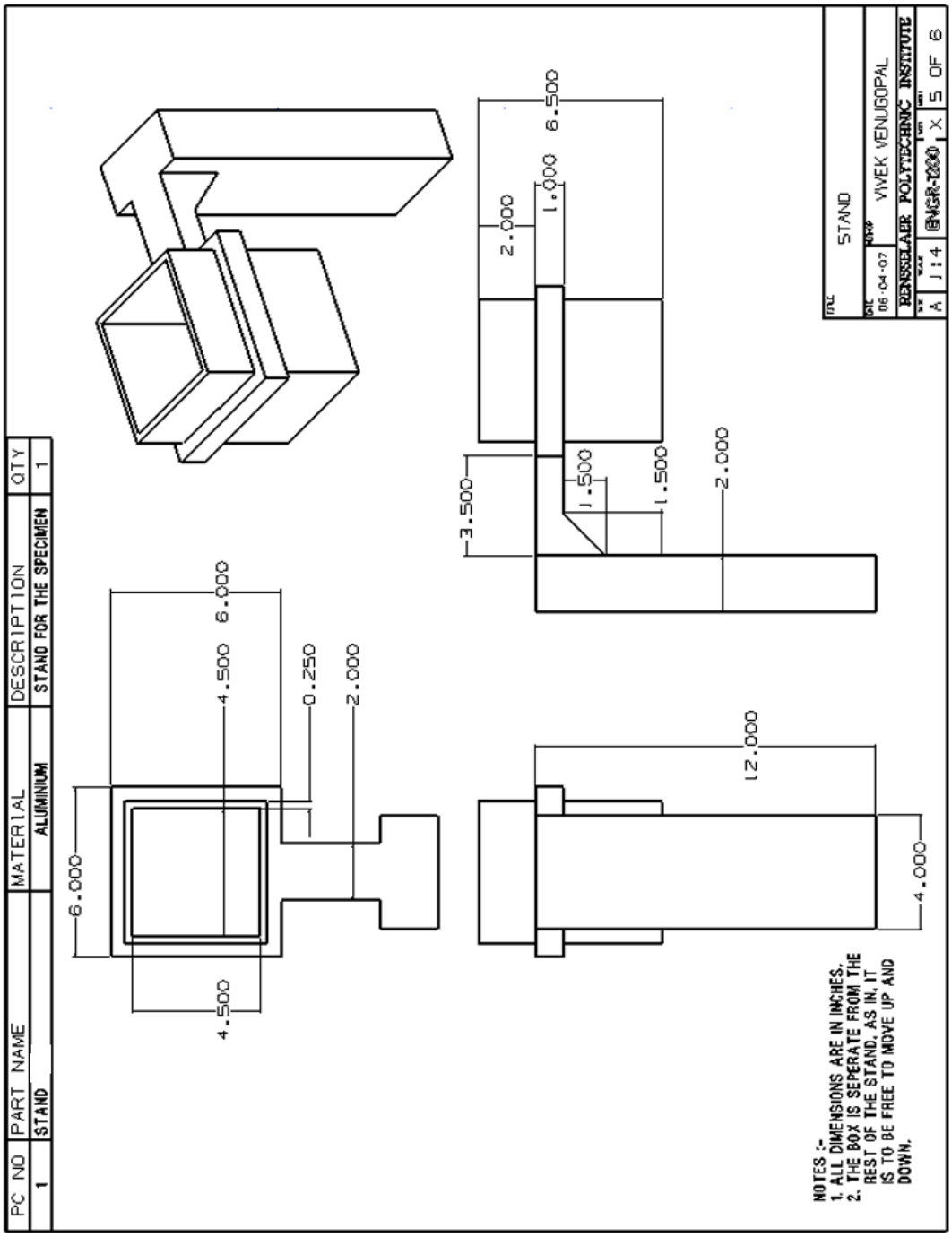

Figure A.4: The Specimen Stand

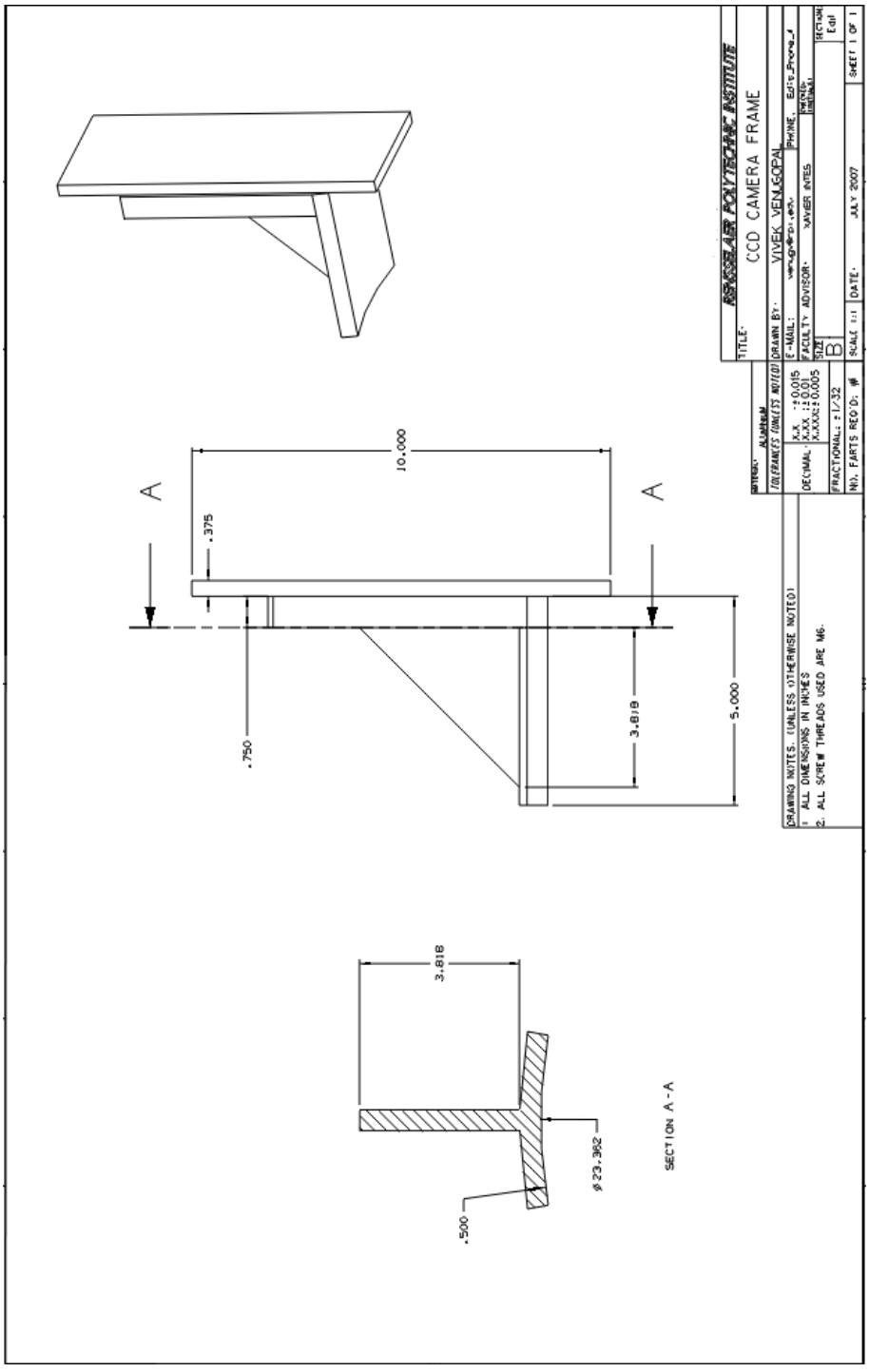

Figure A.5: The Camera Frame

APPENDIX B
Control Module Connections

The following pages show the wiring diagram of the control module in Figure B.1 and the connectors of the USB 6211 DAQ device have been defined in Figure B.2.

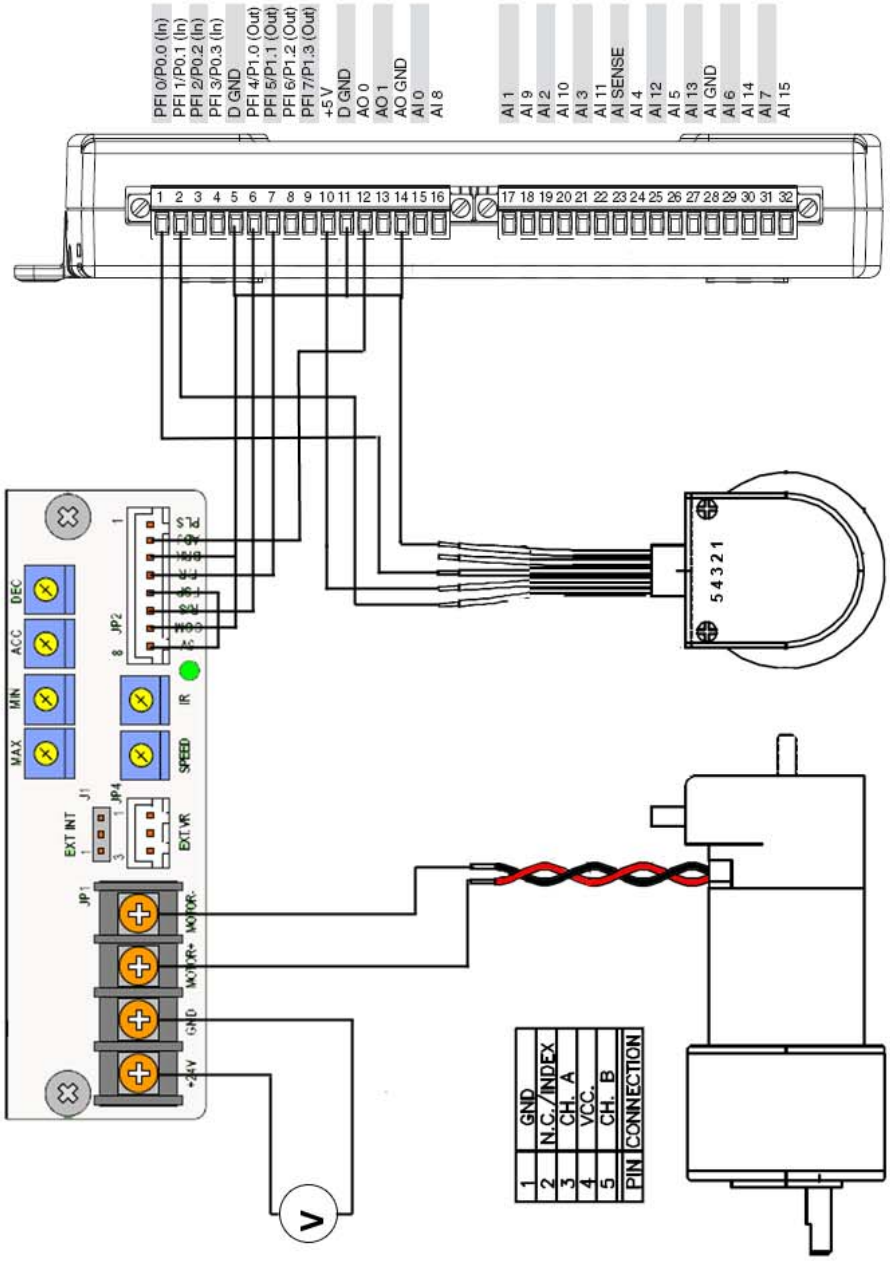

Figure B.1: Wiring Diagram

Signal Name	Reference	Direction	Description
AI GND	—	—	**Analog Input Ground**—These terminals are the reference point for single-ended AI measurements in RSE mode and the bias current return point for DIFF measurements. All three ground references—AI GND, AO GND, and D GND—are connected on the device.
AI <0..31>	Varies	Input	**Analog Input Channels 0 to 31**—For single-ended measurements, each signal is an analog input voltage channel. In RSE mode, AI GND is the reference for these signals. In NRSE mode, the reference for each AI <0..31> signal is AI SENSE. For differential measurements, AI 0 and AI 8 are the positive and negative inputs of differential analog input channel 0. Similarly, the following signal pairs also form differential input channels: <AI 1, AI 9>, <AI 2, AI 10>, <AI 3, AI 11>, <AI 4, AI 12>, <AI 5, AI 13>, <AI 6, AI 14>, <AI 7, AI 15>, <AI 16, AI 24>, <AI 17, AI 25>, <AI 18, AI 26>, <AI 19, AI 27>, <AI 20, AI 28>, <AI 21, AI 29>, <AI 22, AI 30>, <AI 23, AI 31>
AI SENSE	—	Input	**Analog Input Sense**—In NRSE mode, the reference for each AI <0..31> signal is AI SENSE.
AO <0..1>	AO GND	Output	**Analog Output Channels 0 to 1**—These terminals supply the voltage output of AO channels 0 to 1.
AO GND	—	—	**Analog Output Ground**—AO GND is the reference for AO <0..1>. All three ground references—AI GND, AO GND, and D GND—are connected on the device.
D GND	—	—	**Digital Ground**—D GND supplies the reference for PFI <0..15>/P0/P1 and +5 V. All three ground references—AI GND, AO GND, and D GND—are connected on the device.
+5 V	D GND	Input or Output	**+5 V Power**—These terminals provide a +5 V power source or can be used to externally power the PFI outputs.
PFI <0..3>, PFI <8..11>/P0.<0..7>	D GND	Input	**Programmable Function Interface or Static Digital Input Channels 0 to 7**—Each PFI terminal can be used to supply an external source for AI, AO, or counter/timer inputs. You also can use these terminals as static digital input lines.
PFI <4..7>, PFI <12..15>/P1.<0..7>	D GND	Output	**Programmable Function Interface or Static Digital Output Channels 0 to 7**—You can route many different internal AI, AO, or counter/timer outputs to each PFI terminal. You also can use these terminals as static digital output lines.
NC	—	—	**No connect**—Do not connect signals to these terminals.

Figure B.2: Connector Signals

APPENDIX C
Labview Virtual Instrument (VI)

The VI implementing the control algorithm for the imaging system is presented in the following pages. Figure C.1 shows the user interface for the motion control. Figure C.2 shows the main VI which uses three seperate VI, Encoder Input, Controller and Motor Output. These three subsystems are shown in Figures C.4, C.3 and C.5 respectively.

Figure C.1: Front Panel of the Labview VI

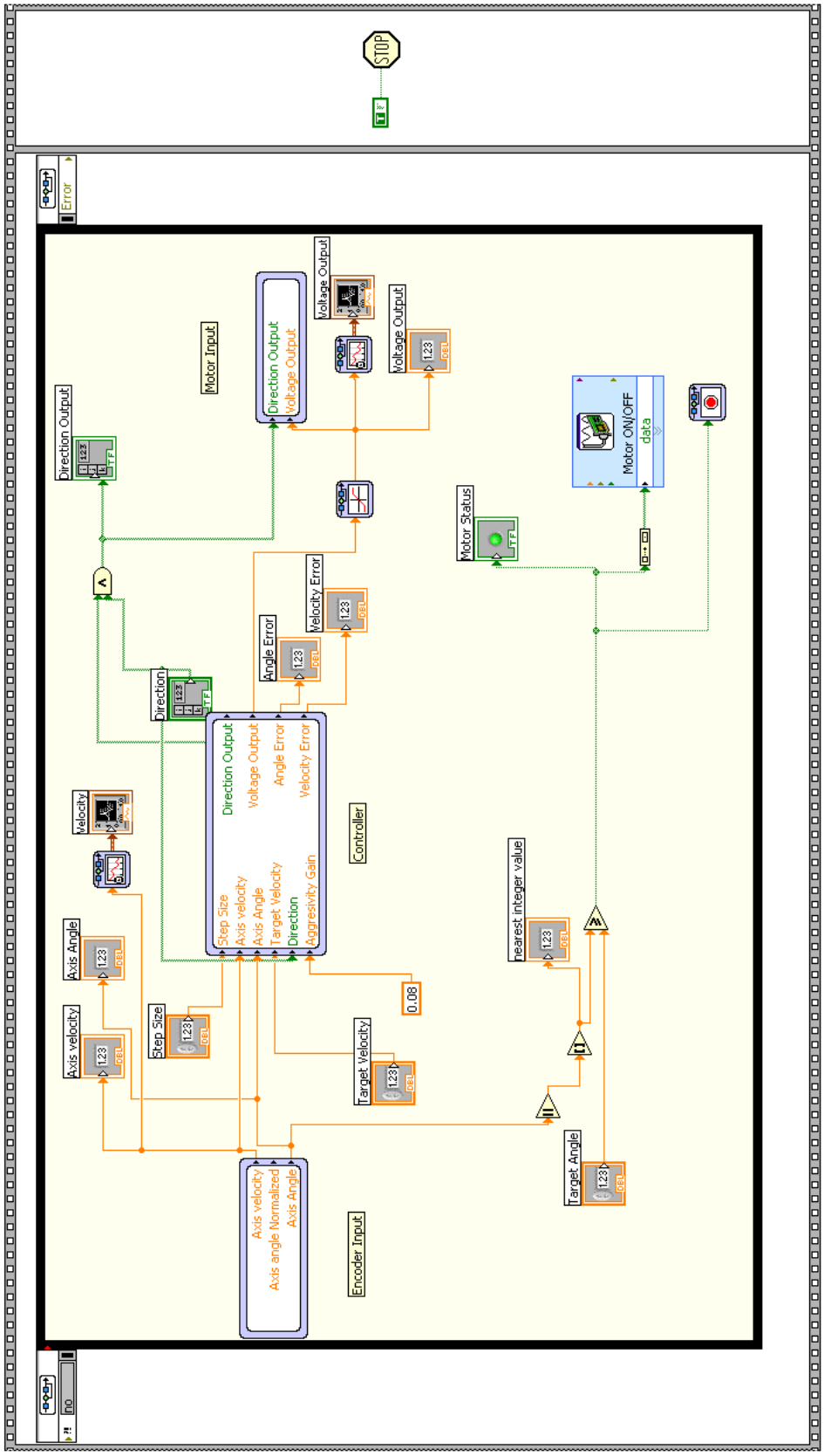

Figure C.2: The VI wrapper for the controller and the data I/O

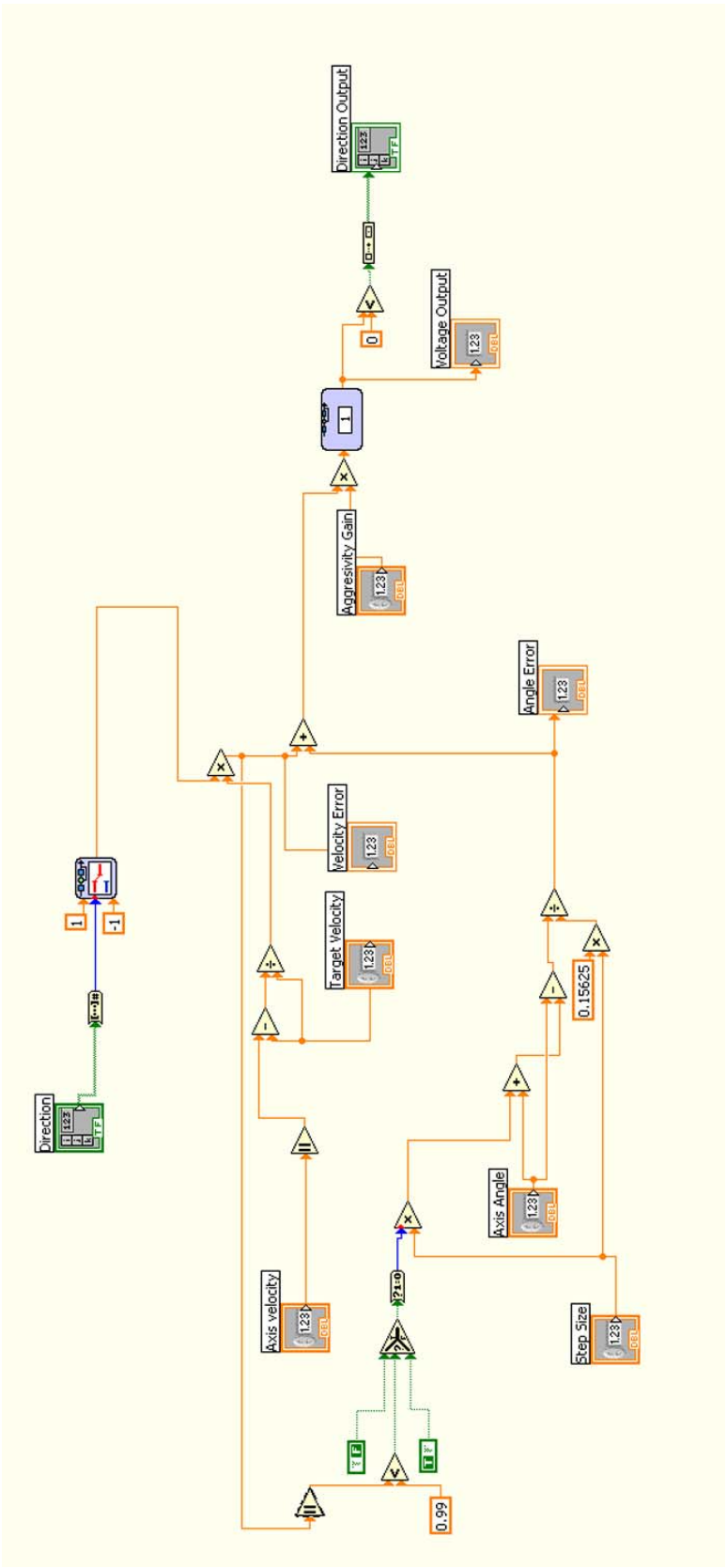

Figure C.3: Controller Subsystem – VI subsystem implementing the control algorithm

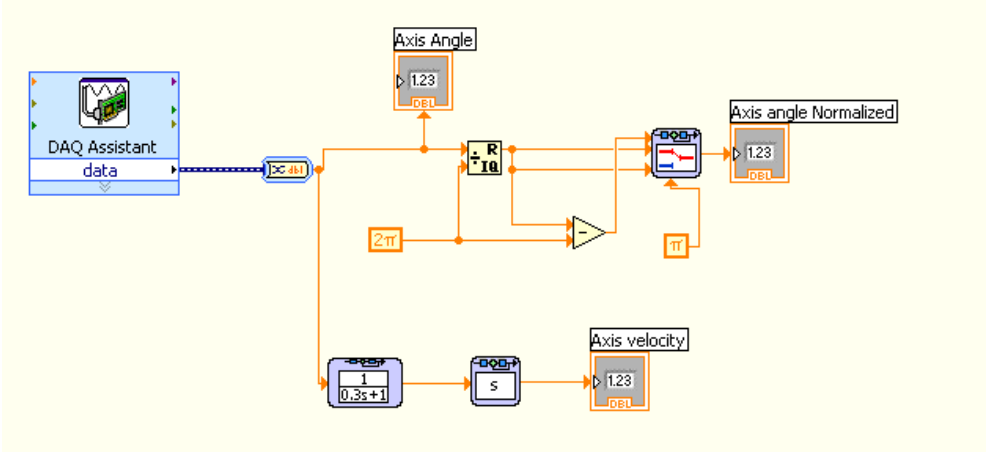

Figure C.4: Encoder Input Subsystem – VI subsystem receiving encoder pulses from the motor

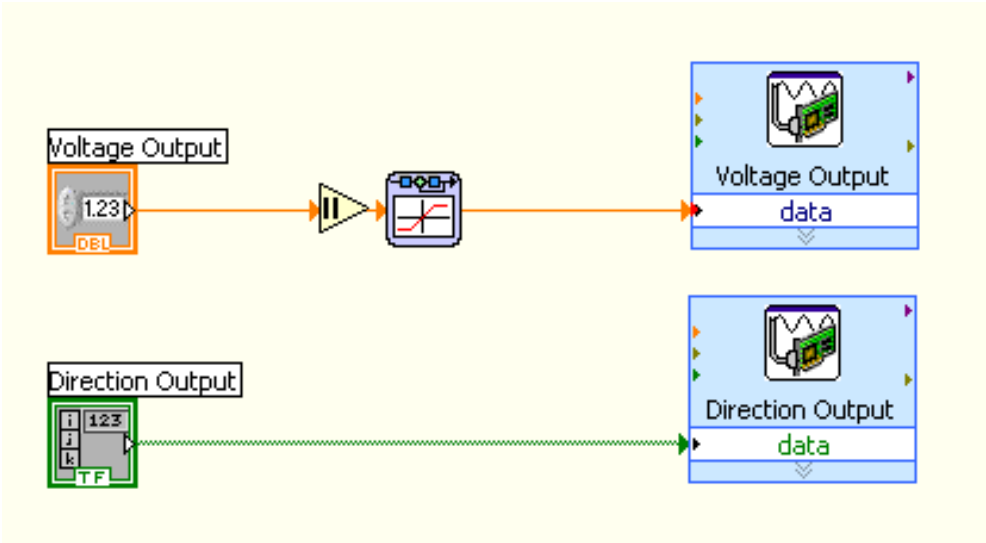

Figure C.5: Motor Output Subsystem – VI subsystem sending command siganls to the motor through the drive

APPENDIX D
Light Propagation in Tissues

In this section, the mathematical model defining the interaction of light with tissues is discussed. Owing to the complicated nature of the electromagnetic theory a model known as the Radiation Transport (RT) theory is adopted for studying the propagation of light in tissues. The RT theory ignores the electromagnetic properties of light like phase and polarization and follows the transport of light energy. However the wave theory is used to determine the material parameters used in the fundamental equations. The fundamental quantity in the RT theory is the *specific intensity*, $I(r, \hat{s}, t)$ which is described as the light power per unit area per solid angle. This is given by the relation,

$$dP = I(r, \hat{s}, t) d\omega da \tag{D.1}$$

where, dP is the light power at time t and at point r directed in a cone of solid angle $d\omega$ oriented in the direction of unit vector $\hat{s}$, from a surface area da normal to $\hat{s}$.

The *attenuation coefficient* is defined in terms of the scattering and absorption coefficients as,

$$\mu_t = \mu s + \mu_a \tag{D.2}$$

and the total mean free path is given as,

$$l_t = \frac{1}{\mu s + \mu_a} \tag{D.3}$$

The *Average Cosine of Scatter*, g is a measure of the scatter retained in the forward direction after a scatter event. A scatterer with a positive value of g is more likely to scatter the photon in the forward direction while a negative value represents backward scattering. Also the value of g for isotropic scattering is 0. Human tissue has a value of g between 0.4 and 0.99.

D.0.1 Radiation Transfer Equation

This equation (also known as Boltzmann equation) is the fundamental equation which describes the dynamics of specific intensity in the RT model. In other words it describes the propagation of a packet of light at *r(t)* having direction of propagation $\hat{s}$ through space over time *dt*. This packet loses intensity due to absorption and scattering but also gains energy from other scattered photons scattered from other directions and also from other sources of light at *r(t)*.

Combining all these processes, the Radiation Transport equation is written as,

$$\begin{aligned} \frac{1}{c_m}\frac{d}{dt}I(r(t),\hat{s},t) &= -(\mu_s+\mu_a)I(r(t),\hat{s},t) \\ &+ \frac{\mu_s+\mu_a}{4\pi}\int p(\hat{s},\hat{s}')I(r(t'),\hat{s}',t)d\Omega' \\ &+ Q(r(t),\hat{s},t), \end{aligned} \tag{D.4}$$

where, $Q(r(t),\hat{s},t)$ is the source term and c_m is the average speed of light in the medium. If the coordinate system is fixed to the medium then the derivative can be reduced to partial derivatives and the equation becomes,

$$\begin{aligned} \frac{1}{c_m}\frac{\partial}{\partial t}I(r,\hat{s},t) = &- \hat{s}\cdot\vec{\bigtriangledown}I(r,\hat{s},t) - (\mu_s+\mu_a)I(r,\hat{s},t) \\ &+ \frac{\mu_s+\mu_a}{4\pi}\int p(\hat{s},\hat{s}')I(r,\hat{s}',t)d\Omega' \\ &+ Q(r,\hat{s},t), \end{aligned} \tag{D.5}$$

The dynamics can be interpreted through the change of $I(r,\hat{s},t)$ with time. The specific intensity will increase with time if its spatial derivative in the $\hat{s}$ direction is decreasing, that is, it will flow from regions of high intensity to low intensity. The $-(\mu_s+\mu_a)I(r,\hat{s},t)$ term will always decrease the value of specific intensity as it accounts for the effects of scattering and absorption losses. The integral term will increase $I(r,\hat{s},t)$ as it accounts for the scattering from all other directions into the $\hat{s}$ cone and so will $Q(r,\hat{s},t)$ which represents the source at r.

An important case of the RT equation is the steady-state form which means that

the $\frac{\partial}{\partial t} I(r, \hat{s}, t) = 0$. This implies that the losses and gains are balanced such that the specific intensity does not change with time at any point in the medium. This occurs when the light wave has had time to reverberate through the tissue layers. The steady-state RT equation in a source free region is given by,

$$\hat{s} \cdot \vec{\bigtriangledown} I(r, \hat{s}) = -(\mu_s + \mu_a) I(r, \hat{s}) + \frac{\mu_s + \mu_a}{4\pi} \int p(\hat{s}, \hat{s}') I(r, \hat{s}') d\Omega' \tag{D.6}$$

When the absorption is significantly low to permit significant penetration into the tissue, scattering is the dominant process. It is also known as the *diffusion limit*. The diffusion limit is important because the photons are able to move through the tissue although the strong scattering disperses the light in a random fashion. The particles move through the medium in a series of steps or random direction and random length. With the step being equally likely in every direction, the isotropic scattering coefficient μ_s', which is related to the previously defined anisotropic scattering parameters as,

$$\mu_s' = (1 - g)\mu_s \tag{D.7}$$

In other words, this relation means that the scattering becomes isotropic after $\frac{1}{1-g}$ anisotropic steps. The values of g in tissues lies between 0.4 and 0.99, isotropic diffusion can take place after 2 steps to over 100 steps.The photons can also be absorbed as they propagate and the absorption properties are encompassed by the usual absorption coefficients μ_a.

When the number of photons undergoing the random walk is large, the density of photons can be described as a continous function whose dynamics are decided by the diffision equation. In diffusion the properties of the medium are contained in the **diffusion coefficient**,

$$D = \frac{c_m}{3(\mu_a + (1 - g)\mu_s)}. \tag{D.8}$$

The quantity,

$$\mu_t' = \mu_a + (1 - g)\mu_s \tag{D.9}$$

is called the transfer attenuation of the medium, The diffusion coefficient can also be written as,

$$D = \frac{1}{3} c_m l_t' \tag{D.10}$$

where l_t' is the effective mean free path.

Diffusion Equation

In the scattering dominant limit, the angular dependence of the specific intensity is well approximated by the first-order expansion in the unit vector $\hat{s}$,

$$I_d(r, \hat{s}, t) \cong \frac{1}{4\pi} \Phi_d(r, t) + \frac{3}{4\pi} F_d(r, t) \hat{s}_f \cdot \hat{s}, \tag{D.11}$$

where,

$$\Phi_d(r, t) = \int_{4\pi} I_d(r, \hat{s}, t)\, d\Omega \tag{D.12}$$

is the total intensity at point r, and,

$$F_d(r, t) = F_d(r, t)\hat{s}_f = \int_{4\pi} I_d(r, \hat{s}, t)\hat{s}\, d\Omega \tag{D.13}$$

is the net intensity vector. Integrating all the terms in Equation (D.4) over the entire 4π solid angle results in a new expression in terms of $\Phi_d(r, t)$ and $F_d(r, t)$,

$$\frac{1}{c_m} \frac{\partial}{\partial t} \Phi_d(r, t) = -\vec{\bigtriangledown} F_d(r, t) - \mu_a \Phi_d(r, t) + Q_c + Q_s \tag{D.14}$$

This equation gives a relation of the divergence of F_d in terms of the total intensity Φ_d.

The next step is to define a second relation between F_d and Φ_d and eliminate F_d. The lowest order approximation is obtained by using **Fick's law**,

$$c_m F_d(r, t) = -D \vec{\bigtriangledown} \cdot \Phi_d(r, t). \tag{D.15}$$

Fick's law asserts that the net photon current is proportional to the gradient of the

photon density. In other words, when the photon density varies in space, there is a net flow of photons from high density to low density along the path of the steepest descent. Substituting Equation (D.15) into Equation (D.14) results in the diffusion equation given by,

$$\frac{1}{c_m}\frac{\partial}{\partial t}\Phi_d(r,t) = D\vec{\bigtriangledown}\Phi_d(r,t) - \mu_a c_m \Phi_d(r,t) + Q_c + Q_s \tag{D.16}$$

In a steady state regime in a source free region, the diffusion equation becomes,

$$\bigtriangledown_d^2.\Phi_d(r) - \kappa_d c_m \Phi_d(r) = 0 \tag{D.17}$$

where,

$$\frac{1}{\kappa_d} = \sqrt{\frac{D}{\mu_a c_m}} \tag{D.18}$$

is the diffusion length. A point source of light at r = 0, injecting photons at a rate to maintain a steady state, has a photon density away from the source of,

$$\frac{\Phi_d(r)}{h\nu c_m} = \frac{N\kappa_d^2}{4\pi}\frac{exp[-\kappa_d r]}{r}. \tag{D.19}$$

APPENDIX E
Characterising the absorption coefficient of ink

This section details the experiments carried out in order to determine the absorption coefficient (μ_a) of the blue ink that was used as an absorbing agent in the phantom studies. This charaterization was done on the basis of the Beer-Lambert law. The Beer-Lambert law states,

$$I = I_o \, exp\,[-\mu_a l] \tag{E.1}$$

μ_a is also expressed as,

$$\mu_a = \epsilon_\lambda \, c \tag{E.2}$$

where, ϵ_λ is the extinction coefficient at wavelength λ and c is the concentration of the absorption agent. Taking the logarithm of both sides of equation E.1 we get,

$$\log \frac{I}{I_o} = -\epsilon_\lambda \, c \tag{E.3}$$

The term $\frac{I}{I_o}$ is called transmittance (T) and $\log_{10} \frac{I}{I_o}$ is defined as the Absorbance (A) of the optical medium.

In this experiment a 5 % stock solution of the ink was prepared by mixing 500 μl of ink in 9.5 ml of distilled water. The procedure involved adding 100 μl of the ink solution to a 4 ml water. The 4 ml water solution hencforth referred to as the buffer was placed in a plastic cuvette. The cuvette was placed in front of a white light source and the spectrum of the transmitted light was measured using a USB2000 spectrophotometer (Ocean Optics, USA). Following each measurement the buffer was changed to avoid error due to change in buffer volume during mixing. The volume of ink solution was added in steps of 100 μl. Figure E.1 shows the transmission spectra of the light obtained after passing through varying concentrations. The spectrum of light passing through the buffer at 0 ink concentration is taken as the I_o spectrum to account for absorption of water and the cuvette. The ratio of I and I_o gives the value of transmission for each wavelength and the logarithm of the transmission gives the absorbance. Figures E.2 and E.3shows the graphs of

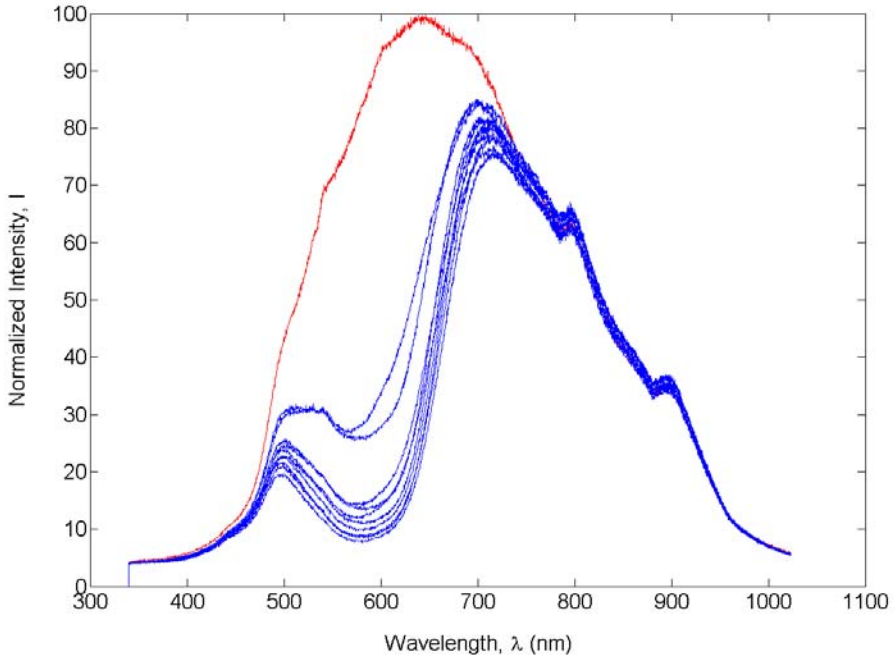

Figure E.1: Spectra of light transmitted through ink solutions of varying concentration. The spectra shown in red shows the spectrum of light through the buffer. This will be taken as the I_o value.

transmission and absorbance with wavelength.

Following this, the slope of the graph between absorbance and concentration was determined for each wavelength. The length of the path of light was assumed to be the diameter of the cuvette and it was found to be 11 mm. The slope was divide by this length to get the value of extinction coefficient, ϵ. Figure E.4 shows the linear fit made on the data is shown for one particular wavelength and Figure E.5 shows the extinction coefficient calculated by this process. The vallue of extinction coefficient at our wavelength of interest was found to be **12.86** $mm^{-1}.\mu l/ml$.

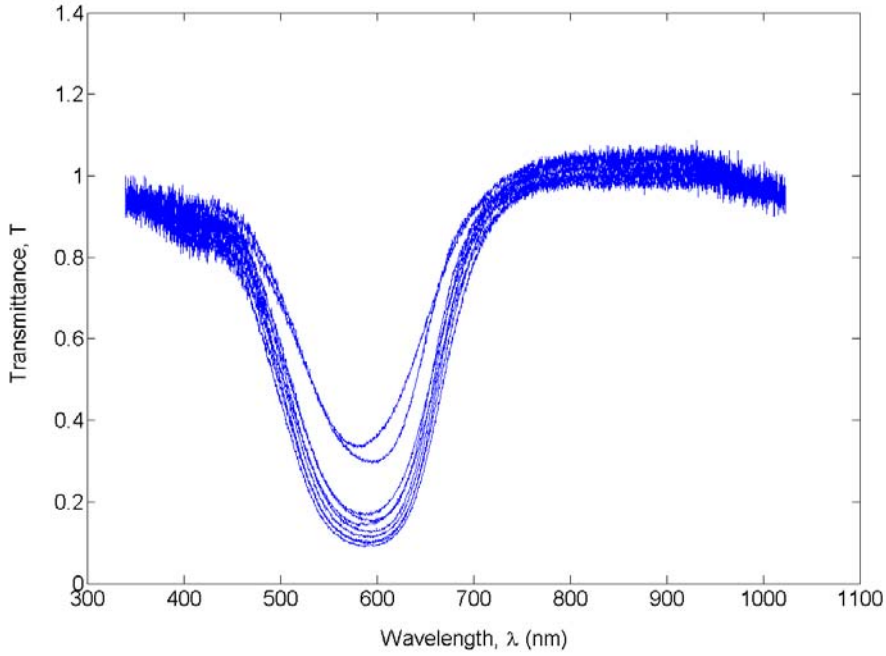

Figure E.2: Transmission of the medium.

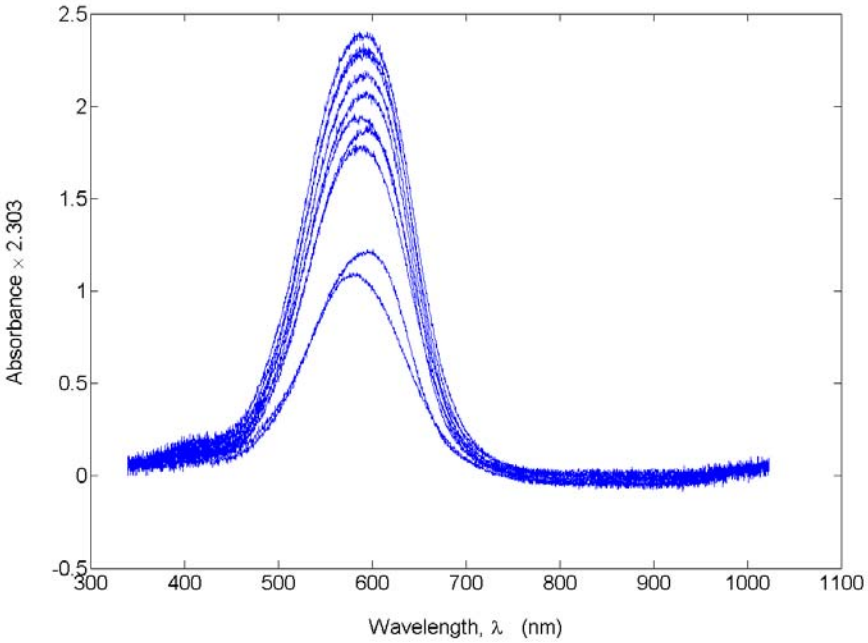

Figure E.3: Absorbance of the medium.

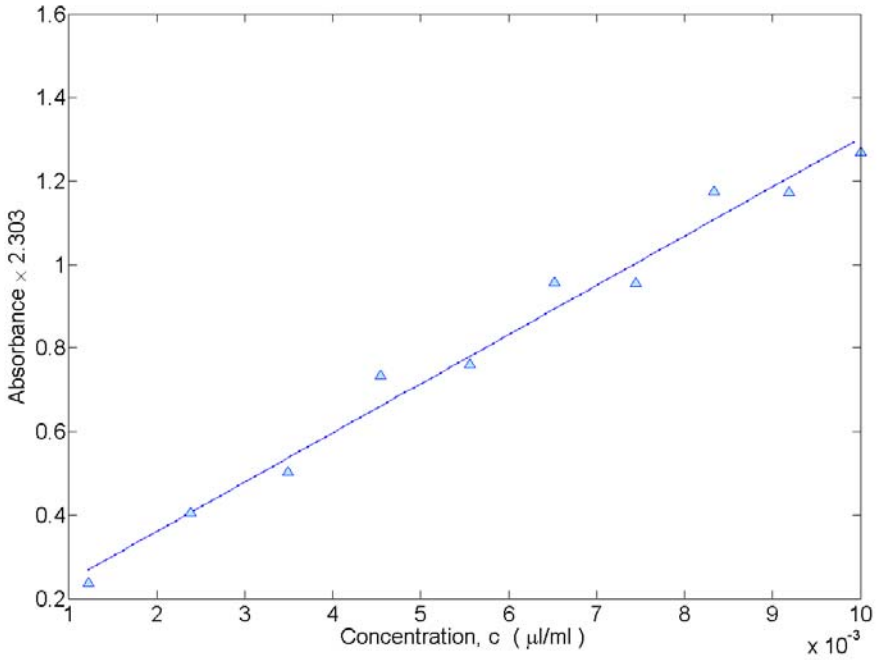

Figure E.4: Linear fit made at 595 nm.

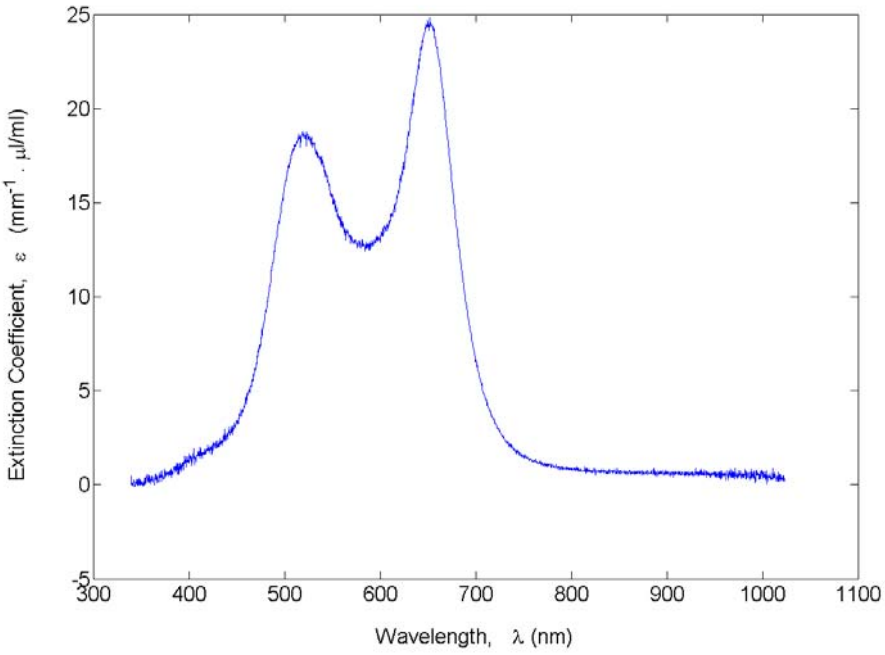

Figure E.5: Graph showing the variation of extinction coefficient of the ink with wavelength.